PhD THESIS

EXPERIMENTAL ANALYSIS AND VALIDATION OF ULTRASONIC TORSIONAL WAVES

UNIVERSITY OF GRANADA - SPAIN

DOCTORAL PROGRAMME IN CIVIL ENGINEERING
DEPARTMENT OF STRUCTURAL MECHANICS

INAS H. FARIS

SUPERVISOR: GUILLERMO RUS CARLBORG

Editor: Universidad de Granada. Tesis Doctorales
Autor: Inas H. Faris
ISBN: 978-84-1306-972-2
URI: http://hdl.handle.net/10481/69872

EXPERIMENTAL ANALYSIS AND VALIDATION OF ULTRASONIC TORSIONAL WAVES

ULTRASONICS LAB
TISSUE MECHANICS

EXPERIMENTAL ANALYSIS AND VALIDATION OF ULTRASONIC TORSIONAL WAVES

author:
INAS H. FARIS

supervisor:
GUILLERMO RUS CARLBORG

May 2021

A DISSERTATION SUBMITTED IN PARTIAL FULFILLMENT OF THE REQUIREMENTS FOR THE DEGREE OF DOCTOR OF PHILOSOPHY

Doctoral Programme in Civil Engineering
Department of Structural Mechanics and Hydraulic Engineering
University of Granada
Granada (Spain)

UNIVERSIDAD DE GRANADA

La doctoranda INAS H FARIS y el director de la tesis GUILLERMO RUS CARLBORG, garantizamos, al firmar esta tesis doctoral, que el trabajo ha sido realizado por el doctorando bajo la dirección del director de la tesis y hasta donde nuestro conocimiento alcanza, en la realización del trabajo, se han respetado los derechos de otros autores a ser citados, cuando se han utilizado sus resultados o publicaciones.

Granada, mayo de 2021.

Director de la Tesis | Doctorando

Fdo.: GUILLERMO RUS CARLBORG | INAS H FARIS

"Nothing in life is to be feared; it is only to be understood."

Marie Curie

Acknowledgements

My deep gratitude goes first to my supervisor, Prof. Guillermo Rus. Who expertly guided me through this part of my postgraduate stage and shared the excitement of nearly four years of discovery. His unwavering enthusiasm for physics and engineering kept me constantly engaged with my research. His generosity made my time at the Ultrasonic Lab enjoyable.
I spent countless days observing Guillermo, with lots of fascination and magic, when he programs, configures and measures all kinds of things he encounters. This picture of his made me, after a lifetime, discover what I really want to do. He makes me have big dreams.

My appreciation also extends to my laboratory colleagues. Antonio and Jorge's mentoring and encouragement have been precious; their early insights launched the greater part of this dissertation. Many thanks also to Jose, Bea, Juanma and Manu, who enlivened the -3 subbasement with good humour, engineering, music, some remarkable disastrous experiments that we have carried out well due to the episodes of laughter they caused. They all succeed in creating a positive atmosphere in which to do science.

Notable credits go to *the millionaires*, the *coffee tigers*, the *evil one and his enemy*, Lucia and Esther for their love and patience. Because they always understood.

I am indebted to my family, whose value for me only grows with time.

Inas

Sometimes my courage fails me and I think I ought to stop working, live in the country and devote myself to gardening[1]. But I am held by a thousand bonds, and I don't know when I shall be able to arrange things otherwise. ***Nor do I know whether, even by writing scientific books, I could live without the laboratory.***[2]

[1] A bakery in Órgiva, in my case
[2] Letter to her sister Bronya, September 1927. In Eve Curie, Madame Curie (1938).

Publications & Conference presentations

Publications

- **Faris IH**, Melchor J, Callejas A, Torres J, Rus G. Viscoelastic Biomarkers of Ex Vivo Liver Samples via Torsional Wave Elastography. Diagnostics (Basel). 2020;10(2):111. Published 2020 Feb 19. doi: 10.3390/diagnostics10020111
- Callejas A, Melchor J, **Faris IH**, Rus G. Hyperelastic Ex Vivo Cervical Tissue Mechanical Characterization. Sensors. 2020; 20(16):4362. https://doi.org/10.3390/s20164362
- Rus G, **Faris IH**, Torres J, Callejas A, Melchor J. Why Are Viscosity and Nonlinearity Bound to Make an Impact in Clinical Elastographic Diagnosis? Sensors. 2020; 20(8):2379. https://doi.org/10.3390/s20082379
- Callejas A, Melchor J, Faris IH, Rus G. Hyperelastic Ex Vivo Cervical Tissue Mechanical Characterization. Sensors. 2020; 20(16):4362. https://doi.org/10.3390/s20164362
- Jorge Torres, **Inas Faris**, Antonio Callejas, "Histobiomechanical Remodeling of the Cervix during Pregnancy: Proposed Framework", Mathematical Problems in Engineering, vol. 2019, Article ID 5957432, 11 pages, 2019. https://doi.org/10.1155/2019/5957432
- Callejas A, Gomez A, **Faris IH**, Melchor J, Rus G. Kelvin–Voigt Parameters Reconstruction of Cervical Tissue-Mimicking Phantoms Using Torsional Wave Elastography. Sensors. 2019; 19(15):3281. https://doi.org/10.3390/s19153281
- Yazdi, A. A., Melchor, J., Torres, J., **Faris, I.**, Callejas, A., Gonzalez-Andrades, M., & Rus, G. (2020). Characterization of non-linear mechanical behavior of the cornea. Scientific RepoRtS, 10(1), 1-10.

Conference presentations

- Ex vivo human cervix acoustical shear ultrasonic properties, International Congress on Ultrasonics, Brugge (Belgium),2019, INAS H FARIS; Antonio Manuel Callejas Zafra; Jorge Torres Perez; Juan Manuel Melchor Rodríguez; Guillermo Rus Carlborg.
- Assessment of mechanical biomarkers of ex-vivo liver samples, 27th International Conference on Composites or Nano Engineering, University of Granada, Granada (Spain), 2019, INAS H FARIS; Antonio Manuel Callejas Zafra, Guillermo Rus.
- Acoustical biomechanical properties of ex-vivo human cervix, Euroson, Granada (Spain), 2019, INAS H FARIS; Antonio Manuel Callejas Zafra; Jorge Torres Perez; Juan Manuel Melchor Rodríguez; Guillermo Rus Carlborg.
- Mechanical biomarkers by torsional wave elastography for gestational diagnosis, First Colloquium of The Spanish Theoretical and Applied Mechanics Society, Madrid (Spain)2019, INAS H FARIS; Antonio Manuel Callejas Zafra; Juan Manuel Melchor Rodríguez; Jorge Torres Perez; Guillermo Rus Carlborg.
- Propiedades ultrasónicas del cizallamiento acústico de muestras ex vivo de hígado animal, VIII Reunión del Capítulo Nacional de la Sociedad Europea de Biomecánica, Castellón (Spain), 2018, INAS H FARIS; A Callejas, Juan Manuel Melchor Rodríguez; Guillermo Rus Carlborg.
- Experimental analysis and validation of cervical tissue biomechanical properties using SWE. The World Congress of Biomechanics, Dublin (Ireland) 2018, INAS H FARIS; Juan Manuel Melchor Rodríguez; Guillermo Rus Carlborg; Antonio Manuel Callejas Zafra.

Abstract

The structural microarchitecture of soft tissue is getting attention among the biomechanical engineering community and rising interest in clinical diagnosis in a broad spectrum of specialities. The new scientific concept of torsional waves (TW) ultrasound will enable the in vivo and noninvasive quantification of a new class of biomarkers. These biomarkers, direct measures of tissue mechanical properties, are intimately related to the structural microarchitecture of soft tissue and ideal for diagnostic applications. This concept will be validated by the novel technology proposed herein by generating and sensing torsional waves in soft tissue. The breakthrough that this new generation of physical-mechanical biomarkers implies will have a long-term impact. The elastic functionality of tissues is intimately linked to a variety of pathologies.

Its quantitative measurement in vivo constitutes a disruptively new diagnostic principle proposed only recently. Well beyond birth and labour disorders (prematurity, induction failures, placenta, etc.), it has enormous potential of being extended to diagnose a growing range of highly prevalent pathologies, including solid tumours (e.g. prostate, cervix, breast, melanoma), connective tissue disorders (ligament injuries, ageing disorders), and liver fibrosis, to name a few. Quantifying the elastic functionality of the cervix is currently not a standard diagnostic tool since no elasticity quantifying technologies exist now or are still under early research. One of the most important potential torsional wave device applications will reduce infant mortality and childhood morbidity. By quantifying biomechanical properties of the cervix in at-risk women, sufficiently early detection of preterm birth may be identified so that suitable interventions can be implemented to delay delivery. The noninvasive in vivo quantification of the biomechanical properties of the cervix will be the clinical focus of this project. This will be accomplished by combining the underlying theory, the technological advances necessary for a proof-of-concept torsional wave diagnostic probe and model-based inverse algorithms to reconstruct the cervical stroma microarchitecture to predict its elastic evolution predict its structural ability to dilate. Finally, and most importantly, this project broadens the scope of applications, paving the way to any situation related to modifications of the collagen mechanics, like mechanobiological cell signalling, controlling tumour growth, inflammatory and healing processes, etc., and opening a new

and broad field of research with impacting applications.
The research group to which I belong has developed the torsion wave elastography technique and has patented an isotropic sensor validated in vivo by measuring under different conditions (pressure and angle of incidence) in pregnant women non-pregnant volunteers. At the same time, the validation was done against a rheometer with ex vivo tissue samples. My contribution to the work focuses on exploring new designs and validating the sensor against the gold standard: shear wave elastography using a Verasonics US research system(Vantage 256, Verasonics Inc., Redmond, WA, USA) and using mechanical testing. The validation was concentrated at the beginning employing tissue-mimicking phantoms, animal tissue, liver, and breast. Only when I entirely programmed the scripts for shear wave elasticity imaging and integrated the post process algorithms, I focused on scans of ex vivo samples of the human uterine cervix. This is due to the difficulty of obtaining these samples. This dissertation includes four main objectives (1) Quantification of tissue viscoelasticity using isotropic TWE probe; First validation against SWEI was done for ex vivo animal liver and tissue-mimicking hydrogel phantoms and only after, for ex vivo human uterine cervical tissue. Four rheological fitting models were used. As far as we know, these results are the first that are presented using this technique. (2) An additional step is to explore how the TW sensor behaves when measuring tissues with different layers, epithelial and connective. Being the first layer much thinner than the second. Therefore, and to check the type of waves propagating in shell-like elements, a new sensor was designed to measure corneas and have a concave shape. So, I explored tissue viscoelasticity in bounded media; Cornea designing and fabricating a modified isotropic TWE probe. (3) Assessment of shear stiffness of anisotropic soft tissue employing a new design of the TWE probe sectorized with three channels, capable of measuring in a single batch in three different directions. (4) Attempts to the nonlinear viscoelastic characterization of the cervical tissue. We proposed a nonlinear model and compared it with the models present in the literature.

Resumen

La microarquitectura estructural de los tejidos blandos está recibiendo atención entre la comunidad de ingenieros biomecánicos y está aumentando el interés en el diagnóstico clínico en un amplio espectro de especialidades. El nuevo concepto científico de ultrasonido de ondas torsionales (TW) permitirá la cuantificación in vivo y no invasiva de una nueva clase de biomarcadores. Estos biomarcadores; medidas directas de las propiedades mecánicas de los tejidos, están íntimamente relacionados con la microarquitectura estructural de los tejidos blandos y son ideales para aplicaciones de diagnóstico. Este concepto será validado por la nueva tecnología propuesta en esta tesis; generar y detectar ondas de torsión en tejidos blandos. El gran avance que supone esta nueva generación de biomarcadores físico-mecánicos tendrá un impacto a largo plazo. La funcionalidad elástica de los tejidos está íntimamente ligada a una variedad de patologías.
Su medición cuantitativa in vivo constituye un principio de diagnóstico disruptivamente nuevo propuesto recientemente. Mucho más allá de los trastornos del embarazo y el parto (prematuridad, fallos en la inducción, placenta, etc.), tiene un enorme potencial de extenderse para diagnosticar una gama cada vez mayor de patologías altamente prevalentes, incluidos los tumores sólidos (p. Ej., Próstata, cuello uterino, mama, melanoma), trastornos en los tejidos conectivo (lesiones de ligamentos, trastornos debido al envejecimiento) y fibrosis hepática, por nombrar algunos. La cuantificación de la funcionalidad elástica del cuello uterino no es actualmente una herramienta de diagnóstico estándar, ya que actualmente no existen tecnologías de cuantificación de la elasticidad o aún se encuentran en fase de investigación inicial. Una de la potencial aplicacione del dispositivo de ondas torsionales más importantes se resume en reducir la mortalidad y la morbilidad infantil. Al cuantificar las propiedades biomecánicas del cuello uterino en mujeres en riesgo, se puede identificar una detección lo suficientemente temprana del parto prematuro para que se puedan implementar las intervenciones adecuadas para retrasar el parto. La cuantificación no invasiva in vivo de las propiedades biomecánicas del cuello uterino será el enfoque clínico de este proyecto. Esto se logrará combinando la teoría subyacente, los avances tecnológicos necesarios para una sonda de diagnóstico de ondas torsionales de prueba de concepto y algoritmos inversos basados en modelos para reconstruir la microarquitectura del estroma cervical para predecir su evolución

elástica y predecir su capacidad estructural para dilatarse. Finalmente, y lo más importante, este proyecto amplía el campo de aplicaciones, allanando el camino a cualquier situación relacionada con modificaciones de la mecánica del colágeno, como la señalización celular mecanobiológica, control del crecimiento tumoral, procesos inflamatorios y de cicatrización, etc., y abriendo una nueva y amplio campo de investigación con aplicaciones impactantes.
El grupo de investigación al que pertenezco ha desarrollado la técnica de elastografía por ondas de torsión y ha patentado un sensor isotrópico validado in vivo midiendo bajo diferentes condiciones (presión y ángulo de incidencia) en mujeres embarazadas y voluntarias no embarazadas. Al mismo tiempo, se realizó la validación frente a un reómetro con muestras de tejido ex vivo. Mi contribución al trabajo se centra en explorar nuevos diseños y validar el sensor contra la tecnología de elastografía estándar: la elastografía de ondas de corte utilizando un sistema Verasonics US research system(Vantage 256, Verasonics Inc., Redmond, WA, USA) y adicionalmente se validará utilizando pruebas mecánicas. La validación se empezó empleando phantoms de gelatina hechos en el laboratorio para la imitación del tejido blando, tejido animal: hígado y pechuga de aves. Solo cuando programé por completo los scripts para la obtención de imágenes de elasticidad por ondas de corte e integré los algoritmos de posproceso, me dediqué en escaneos de muestras ex vivo del cuello uterino humano. Esto se debe a la dificultad de obtener estas muestras. Esta tesis incluye cuatro objetivos principales (1) Cuantificación de la viscoelasticidad tisular utilizando una sonda de ondas de torsión isotrópica; La primera validación contra SWEI se realizó para el hígado animal ex vivo y los phantoms de hidrogel que imitan el tejido y después, para muestras de tejido cervical humano ex vivo. Se utilizaron cuatro modelos de ajuste reológico. Hasta donde sabemos, estos resultados son los primeros que se presentan utilizando esta técnica. (2) Un paso adicional es explorar cómo se comporta el sensor TW al medir tejidos con diferentes capas, epiteliales y conectivos. Siendo la primera capa mucho más fina que la segunda. Por tanto, y para comprobar tipo de ondas que se propagan en elementos con forma de placa, se diseñó un nuevo sensor para medir las córneas con una forma cóncava. Entonces, quantifiqué la viscoelasticidad tisular en medios acotados; como la Cornea diseñando y fabricando una modificación de la sonda de ondas de torsión isotrópica. (3) Evaluación de la rigidez del tejido blando anisotrópico empleando un nuevo diseño de la sonda de ondas de torsión, pues ha sido sectorizada con tres canales, capaz de medir en una sola tanda en tres direcciones diferentes. (4) La caracterización viscoelástica no lineal del tejido cervical. Propusimos un modelo no lineal y lo comparamos con los modelos presentes en la literatura.

Abbreviations

ARF	Acoustic radiation force
ARFI	Acoustic radiation force impulse
CCI	Cervical consistency index
DE	Dynamic elastography
ECM	Extracellular matrix
FDA	Food and Drug Administration
FEM	Finite element model
FFT	Fast Fourier transform
FOEC	Fourth order elastic constants
GAGs	Glycosaminoglycans
GUI	Graphical user interface
HA	Hyaluronic acid
IQ	In-phase and quadrature
IQR	Interquartile range
ISPPA	Spatial peak pulse average intensity
ISPTA	Spatial peak temporal average intensity
KV	Kelvin-Voigt
KVFD	Kelvin-Voigt fractional derivative
M	Maxwell
MI	Mechanical index
MTL	Multiple track location
PBS	Phosphate buffered saline
PGs	Proteoglycans
PIP	Probabilistic inverse problem
PLA	Polylactic acid
PTV	Particle tracking velocimetry
ROI	Region of interest
SE	Strain elastography
SMC	Smooth muscle cells
SPTB	Spontaneous preterm birth
sPTD	Spontaneous preterm delivery
SSI	Supersonic Imagine
SWE	Shear wave elastography
SWEI	Shear wave elasticity imaging
SWS	Shear wave speed

TE	Transient elastography
TH	Thickness
TOEC	Third order elastic constants
TOF	Time of flight
TU-SWE	Transurethral shear wave elastography
TWE	Torsional wave elastography
USTB	Ultrasound toolbox
WHO	World health organization
Z	Zener
3DMMRE	3D multifrequency magnetic resonance elastography

Contents

List of Figures

List of Tables

Part I

INTRODUCTION

"I am one of those who think like Nobel, that humanity will draw more good than evil from new discoveries."

Marie Curie

Chapter1

Introduction

1.1.Project rationales and goals

The research group to which I belong has developed the torsion wave elastography technique (TWE) and has patented an isotropic sensor that has been validated in vivo by measuring under different conditions (pressure and angle of incidence) in pregnant women and non-pregnant volunteers. At the same time, the validation was done against classical rheometry with ex vivo tissue samples. My contribution to the work focuses on validating the sensor against the gold standard: shear wave elastography using Verasonics US research system(Vantage 256, Verasonics Inc., Redmond, WA, USA). The validation was concentrated at the beginning employing tissue-mimicking phantoms, animal tissue, liver, and breast. Only when I entirely programmed the scripts for shear wave elasticity imaging and integrated the post process algorithms, I focused on scans of ex vivo samples of the human uterine cervix. This is due to the difficulty of obtaining these samples. This dissertation includes four main objectives that are separated into the different chapters as follows:

1. Quantification of tissue viscoelasticity using isotropic TWE probe; First validation against SWEI was done for ex vivo animal liver and tissue-mimicking hydrogel phantoms and only after, for ex vivo human uterine cervical tissue. Four rheological fitting models were used. As far as we know, these results are the first that are presented using this technique.

2. An additional step is to explore how the TW sensor behaves when measuring tissues with different layers, epithelial and connective. Being the first layer much thinner than the second. Therefore, and to check the type of waves propagating in shell-like elements, a new sensor was designed to measure corneas and have a concave shape. So, I explored tissue viscoelasticity in bounded media; Cornea designing and fabricating a modified isotropic TWE probe.

3. Assessment of shear stiffness of anisotropic soft tissue employing a new

design of the TWE probe sectorized with three channels, capable of measuring in a single batch in three different directions.

4. Attempts to the nonlinear viscoelastic characterization of the cervical tissue. We proposed a nonlinear model and compared it with the models present in the literature.

1.2.Impact

The adoption of multiscale approaches by the biomechanical community has achieved a significant improvement in quality in the mechanical characterization of soft tissues. The recent developments in elastography techniques are enabling an in vivo and non-invasive quantification of tissue mechanical properties. Elastic alterations in tissue are associated with a broad spectrum of pathologies, which arises from the tissue microstructure, histology and biochemistry. This knowledge is combined with research evidence, suggesting a powerful diagnostic potential ranging from highly prevalent pathologies, from birth and labour disorders (prematurity, induction failures, etc.) to solid tumours (e.g. prostate, cervix, breast, melanoma) liver fibrosis, to name a few. This work aims to illustrate the TWE technique's potential in quantifying soft tissue viscous, anisotropic and nonlinear elastic parameters as conceivable diagnostic mechanical biomarkers.

This will be accomplished by combining the underlying theory, the technological advances necessary for a proof-of-concept torsional wave diagnostic probe. Finally, and most importantly, this project broadens the scope of applications, paving the way to any situation related to modifications of the collagen mechanics, like mechanobiological cell signalling, controlling tumour growth, inflammatory and healing processes, etc., and opening a new and broad field of research with impacting applications.

1.3.Thesis outline

This thesis is divided into the following parts: An introduction, summarizing the global idea of this work and the objectives that are searched. And some preliminary and basic concepts on the theories of mechanical properties of the soft tissue. A second part where the TWE technique description is detailed. It also details the design and fabrication procedure of the different TW sensor models. How the mechanical biomarkers are reconstructed, and the validation techniques that were used. The experimental results part is divided into four chapters in concordance with the objectives of this thesis. Each chapter includes the experimental set-up, results and conclusions. Finally, the last part includes a summary of the conclusions, limitations of the

TWE and future works.

"I am among those who think that science has great beauty."

Marie Curie

Chapter2

Preliminary concepts: Biomechanics of soft tissue

The soft tissue is responsible for supporting and connecting the different structures of the body. It can be said that almost the whole human body is soft tissue if we exclude bones, teeth and nails, considering that they differ substantially in their flexibility and mechanical properties. Soft tissue modelling can be done on several scales, including microscopic and macroscopic. This work deals with the second. The tissue is fundamentally composed up of three parts, the epithelium, stroma and mesenchymal cells [4]. The role of the different parts of the soft tissue will be addressed in the tissues that are mainly dealt with in this thesis; the cervix and the cornea.

Soft tissue structure is considerably complex; modelling it is challenging and requires close collaboration between the clinical and engineering communities. In 2003 [5], Humphrey has summed it up, saying that it has a *nonlinear, inelastic, heterogeneous, anisotropic character that varies from point to point, from time to time and from individual to individual.*

Soft tissue shows a dynamic behaviour under the effects of an applied load, varying from linear to nonlinear. This is why different mechanical models have been developed to try to capture this behaviour. These models include elastic (linear), hyperelastic (nonlinear elasticity), viscoelastic (time-dependent), and poroelastic (biphasic) types. Additionally, soft tissue can be characterized depending on its homogeneity and isotropy.

In this chapter, some brush strokes are given to introduce the theoretical concepts treated experimentally in this thesis. Additionally, biomechanical explanations concerning the structure of the organs that have been explored to validate the proposed torsional wave technique experimentally are included.

2.1.Human uterine cervix as a biomechanical structure

The possibility of getting specimens of cervical tissue is limited to scientific cases and at-risk only. Therefore there is no availability of considerable numbers of samples, which limits an adequate breakthrough in the characterization of the aetiology of the cervix. The mechanical response in tissues such as the cervix is governed by its collagen structure. Several biological and mechanical changes cause disorientation in this structure during the gestation period, going from cross-linked fibres to just connected fibrils. Linking the variations on a microscopic biological scale to a macroscopic mechanical scale to achieve a multiscale approach to the problem becomes a valuable tool. Currently, there is no available clinical tool to evaluate the cervical biomechanical state quantitatively. For this reason, the WHO (World Health Organization) calls for innovation and research.

2.1.1.The cervix during pregnancy

- **Anatomy and physiology of the cervix:** From the moment a woman gets pregnant, biological changes occur; it is well known that these changes came from the combination of the growing pressures exerted by the fetus and endocrine processes that involves remodelling of the cervical tissue. It begins with biochemical reactions that affect the morphology of the tissue to the point of changing mechanical properties. The cervix serves two different functions: First, to protect from invading organisms from the vagina and maintain the fetus inside the uterus until the time of labour, behaving like a sphincter-like structure[6]. Second, move from a stiff mechanical barrier to a compliant structure that can dilate [7], serving as a guide to leaving the mother.

  The cervix is the cylindrical-shaped fibrous organ located in the lower part of the uterus, around 3 cm in length and 2cm in diameter[8] see Figure2.1. It is covered with epithelium, which is a tissue with an eminently protective function against infections and mechanical aggression. The elliptical convex part protrudes into the vagina is the ectocervix covered by a pinkish stratified squamous epithelium known as the

  exocervix visible zone speculum inspection. It is a non-keratinizing epithelium, which means that it cannot self-hydrate and possess a porous texture. It is composed of 15-20 cell layers. The division between the stroma and the epithelium is a single basal layer of cells with dark nuclei. It is usually a straight section, and however, sometimes there are inclusions of the stroma (stromal papillae). These projections become

vascularized, providing nutrients to the epithelium[9]

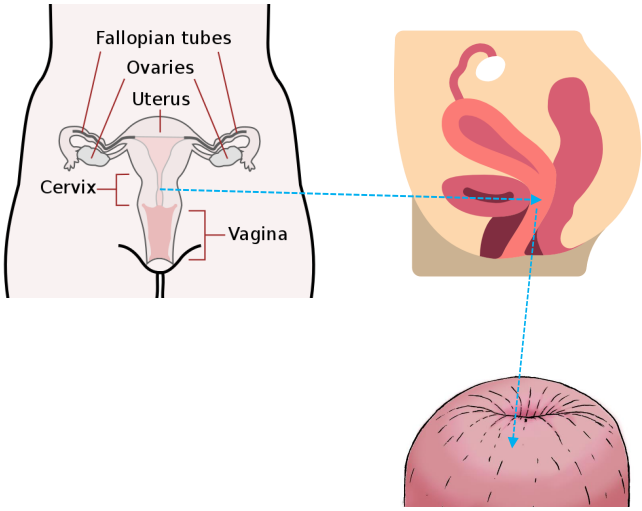

Figure 2.1: Human uterine cervix location

- **Phases of remodelling:** Pregnancy is a process of remodelling where the biochemical relationships within the stroma set-up the new aspect of tissue. The duration of the procedure varies depending on the patient, taking into account her parity[10] and her BMI[11, 12, 13]. It is usually divided into four phases[14] which are superimposed as they occur until birth: softening, ripening, dilation and postpartum.

  1. **Softening:** Cervical softening is the first and most extended phase that commonly starts in the first month. It begins a slowly increasing turnover of ECM components, whose more visible result is the disorganization of the collagen network, which shows a decline in resistance, defined as compliance see Figure2.2. Nevertheless, the tensile strength(the integrity) is maintained. The compliance reflects the decrease in the elastic slope associated with unordered collagen fibres, elastic tension, increased water content and proteoglycans[15]. In the nonpregnant cervix, the epithelial cells are scant. However, during pregnancy, the hormone relaxin is implicated in their proliferation[16] when some prostaglandis(PGs) synthesis begins to be noticed. The cytokine interleukin-8(IL-8) appear[17].
  2. **Ripening:** Cervical ripening begins a few weeks before deliv-

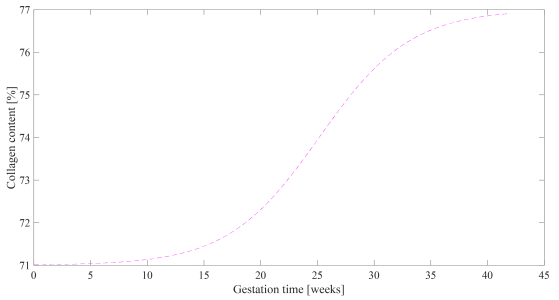

(a)

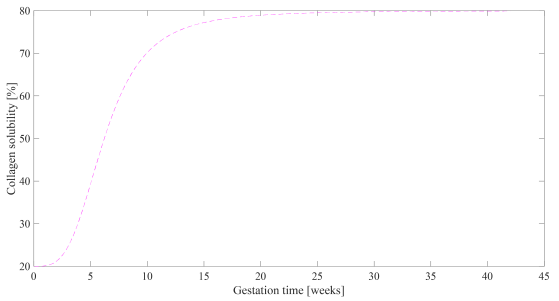

(b)

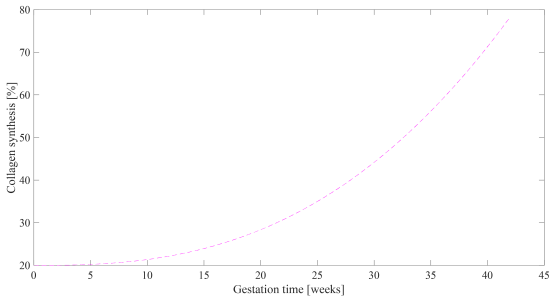

(c)

Figure 2.2: Collagen changes during pregnancy. a) Collagen content (b) Collagen solubility c) Collagen synthesis evolution . Adapted from [1] (CC BY 4.0.)

ery, and rapid changes in the cervix characterize it. It loses its integrity to prepare for the delivery. There is a marked increase in the synthesis of proteoglycans, collagen and hyaluronic acid (HA). Moreover, a hydrophilic glycosaminoglycan that interacts with epithelium cells and proteoglycans as versican. HA is in a considerable molecular weight to favour tissue hydration, resulting in a viscoelastic material, which unbalances the collagen network structure, dispersing and reducing its mechanical resistance[18, 19] due to increasing collagen solubility. Introducing progesterone inhibitors during softening has been proven to cause to reach maturation before[20], demonstrating that progesterone is a factor that maintains pregnancy. The loss of this hormone helps the estrogen to reach its receptors, facilitating the activation of ripening.

3. **Dilation:** The dilation of the cervix, preceded by biochemical changes caused by new hormonal regulation, contractions of the myometrium and the tension of the fetal protrusion, triggering the maximal loss of tensile strength. This process involves the infiltration of leukocytes, PGs, proteases and collagenases into the EMC[21, 22]. The protective mucus plug is expelled; in addition, it comes to a phase of effacement where the cervix narrows its walls and shortens to reach 10 cm in diameter. To complete the pregnancy, the female reproductive system must be transformed from a static formation to an active one with the coordination of its components. This coordination will lead to the final contractions that are transmitted through gap junctions. The continuous transition of the uterus to the cervix implies a reduction in the SMC content[23]. The circular and longitudinal architecture of SMC and collagen is maintained towards the cervix, ensuring a supporting force during pregnancy[24]. Myers et al.[25] identified a collagen remodelling with a four order magnitude reduction in stiffness. The contractions of the uterus are transmitted to the cervix, resulting in a progressive stretching towards dilation. At this point, the cervix resembles an elastic band, which begins to reach the elastic limit in dilation. Hence, the importance of the restorative phase in the postpartum.
4. **Postpartum:** The postpartum phase, the uterine involution, is meant to recover the tensile strength of the tissue, avoid environmental contamination, and prepare for ensuing pregnancies.

□ **Cervix histology** The histological composition of the cervix began

to be investigated in the 1960s on non-pregnant women, where two clearly differentiated zones were distinguished[26]:

- Smooth musculature 5-10%.
- Stroma 90%.

The musculature holds the functional part of the tissue, which is to prepare the cervix to dilate. Generally, studies have focused on the external os, which has more straightforward and direct access. However, Vink et al.[6]study measured that the content of smooth muscle cells (SMC) can reach 50-60% in the internal os, which a priori should not allow to extrapolate results to the whole set of the cervix. It should be remarked that this cell content is similar to that of the uterus, which along with gap junctions, a cell pathway for direct communication, can relate the remodelling of the uterus to the cervix. Stroma is the part of the tissue that ensures that musculature fulfils its mission by providing structural support. The cervix is considered a fibrous connective tissue since bundles of macromolecular fibres form its structure. These macromolecules are found within the stroma and are embedded in an extracellular matrix (ECM), where the most important biochemical reactions occur. The ECM composition can be differentiated into extracellular fluid with a content of approximate 75-80% and dry tissue of about 20% in content. In the latter, the main constituent is fibrillar collagen which forms a cross-linked network entwined with the protein elastin and enclosed by a ground substance of viscous proteoglycans and glycosaminoglycans that offers hydration and other matricellular proteins[27, 28]. A viscoelastic and heterogeneous point of view is required to understand the cervix[29, 30]. The study of Westervelt et al.[31]on the distension in the cervix employing finite elements, where geometric properties and materials were considered, deduced that the geometric parameters affected the most in the simulation softening. On the other hand, Fernandez et al.[32]proved that material properties must be carefully handled. The ECM provides strength and rigidity and has a crucial function during gestation, ensuring the integrity of the tissue.

2.1.2.Evaluation of cervical biomechanical properties

Although in the field of cervical tissue mechanical characterization, most of the works focus on dynamic methods, various techniques have been developed using different modalities, employing different tissue excitations and

extracting different parameters of tissue motion. Some of these methodologies and their application in the care of cervical tissue can be found below.

Since the '70s, elastography has gradually become a widely applied medical imaging technique[33]. The principle of elastography is to induce a motion in the tissue so that a mechanical characterization is possible if the resulting displacements are followed. The difference in the mechanical excitations generated externally or internally led to the development of several elastography techniques. Therefore, different imaging modalities are used to estimate tissue displacement.

- **Quasi-static elastography/ strain imaging:** Quasi-static elastography or strain elastography (SE) was introduced in 1991 by Ophir et al.[34]. In the SE, static compression is used to deform the tissue. This stress can be induced by external palpation with the probe or endogenous stress such as cardiovascular movements to move the tissue. The displacements and the local strains are usually derived from the ultrasonic backscatter signals before and after compression by the 2D correlation of the ultrasound pre and post-compression data. The result is a qualitative deformation gradient map, called elastogram. SE is easy to implement but has limitations, such as the difficulty to compress deep organs. In addition, it is highly dependent on the pressure that the operator transmits to the tissue. Strain-induced by either cardiovascular pulsation or respiration can be used[35] to solve the limitation of SE of transmitting stress to deep organs. This has been used in deep organs like the liver[36]. The first elastography measurement in pregnant cervical tissue was performed by Thomas et al.[37]. In this study, they used static elastography to calculate the ratio of soft tissue to stiffer one during the pregnancy duration and tried to correlate it with the gestational age. After that, Thomas et al. [38]demonstrated no correlation of the tissue quotient with gestational age. Several authors used quasi-static methods to try to determine cervical stiffness during pregnancy. Molina et al.[39] used the hand to provoke tissue displacement to obtain cervical strain. For reproducibility, they also used quasi-static methods in 112 pregnant women in the four different zones of the cervix. Measurements were reliable except in the zone where the transducer exerts the pressure directly. Hernandez-Andrade et al.[40], in a posterior study, also suggested that there is a significant correlation between cervical strain and cervical length but much less correlation with gestational age. In their work, measuring was done in two different cervical regions. Several studies

affirm that it is too soon to adopt quasi-static elastography to truly capture the changes that cervical tissue suffers during the gestational age considering that measurements are highly dependent on the pressure applied by the physician. Several works proposed the standardization of measurements[41, 42, 43]. The primary approach is to be able to control the loading applied on the cervix. Limiting the induced probe displacement was proposed by Molina et al. in[39], and controlling the compression by[40], others proposed using a reference elastomer material[44]. Fruscalzo et al.[45, 46, 47] used quasi-static methods to induce the tissue deformation. They aimed to measure the maximum deformability of the cervix. In summary, it seems there is no way to skip the limitation of strain elastography: the unknown applied pressure, quantification of absolute softness is impossible[48, 42, 49].

- **Dynamic elastography methods (DE)** Were developed to overcome the SE limitations and, mainly, to obtain quantitative elasticity maps. They are based on the propagation of shear waves within the tissue, which can be generated by a vibrating force in sonoelastography[50], a given frequency shift in vibroacoustography[51], in transient elastography[52] is a short impulsion or acoustic radiation force in ARFI and SWE[53].

  - **Acoustic radiation force imaging (ARFI):** Was introduced by Nightingale et al.[54]. This method uses focused ultrasound to generate localized displacement of a few microns via an ARF impulse within the tissue. In the time that lasts the impulse, the acoustic wave propagates through the tissue. Local displacements reflect relative mechanical properties of tissue and tissue deforms in response to the focused ARF excitation, so shear waves propagate away from it[55]. Finally, the displacement generated by the ARF is then mapped within the focal region of each push within a specified region of interest ROI at a known time after stopping the push. The tissue displacement response within the push region is directly related to the magnitude of the applied force and inversely related to the tissue stiffness[53, 54]. ARFI has been used in several clinical studies; examples can be found in[56] for breast, and in[57]for the prostate. The velocity of the shear wave generated by the ARF can be quantified in a small ROI and converted to elastic modulus[58, 59].
  - **Shear wave elastography (SWE)** Uses an ARF (Acoustic Radiation Force) to excite the medium and generate shear waves and produce a medium in a real-time quantitative elasticity map.

The technique can be subdivided into the creation of The Mach-cone, where ultrasound beams are focused successively at different depths to create spherical waves at each focal point. The different generated spherical waves interfere constructively along a Mach-cone creating two quasi-plane shear wavefronts propagating in opposite directions in the imaging plane[60]. Only one Mach-cone is needed to generate the quasi-plane shear wavefronts that travel across the medium to cover the entire ROI. The other division is Ultrafast Imaging, in which ultrasound plane waves are generated to track the shear wave displacement along the entire imaging plane with excellent temporal resolution in one single acquisition, typically up to 5000 frames per second. Therefore, there is no need to repeat the acquisition several times to acquire the entire displacement field. This allows imaging in real-time, which makes the examination easier[61].

– **Supersonic Shear Imaging (SSI)** Is an extension of the SWE method. It also quantifies the tissue elasticity estimating the shear modulus noninvasively and with a real-time image acquisition (30 milliseconds). SSI uses ARF pulses to generate shear waves and ultrafast ultrasound for tracking them[60]. The difference is that instead of simply transmitting one ARF pulse at a time, SSI transmits multiple ARF pulses in quick sequence, focal points differ marginally. The use of SSI possibilities the estimation of shear wave velocity (SWV) in a large area in one sequence. ARF pulses will generate shear waves that interfere with each other. Moving the focal point of ARF pulses is, in this case, a matter of moving a virtual shear wave source, and a source moving at supersonic speeds will create a Mach-cone. Because the source is moving faster than the shear waves, it is considered supersonic.

Non-evident results from SE to assess the cervical consistency motivated the use of dynamic elastography. Shear wave elasticity imaging (SWEI) is the most common form of dynamic elastography applied to the cervix[62, 63]. Shear wave velocity (SWV) can quantify tissue softness or stiffness because shear waves travel faster in stiffer and slower in softer tissues. Producing adequate shear waves in the cervix is not an easy job because we can not predict the wave generation in its boundaries. Even so, SWEI has been used to evaluate the pregnant cervix[64, 65, 11, 66, 67, 68]. In addition, the cervical tissue is highly attenuating because of its microstructural complexity.

Measurements of shear wave velocity were carried out by Carlson et al.[65] in human ex vivo hysterectomy samples. Their objective was to explore the feasibility of SWV to identify ripened cervices. Results show that SWV was capable of differentiating between ripened and unripened cervical tissue. H. Feltovich[41] suggested that elasticity is a very interesting biomarker for physicians since the elastic modulus varies more than 80kPa while SWV varies from approximately 1.2-5.5 m/s over the cervix. Ultrasound techniques have been used recently to expand our knowledge of the mechanical properties of the cervix. Carlson et al. [11] analyzed the feasibility of shear wave elastography, and they found that stiffness decreased with cervical ripening. Ultrasound waves over a wide frequency range were applied by Peralta et al.[69] the work shows that Maxwell's model is possibly the best rheological model for preliminary assessments of cervical viscoelastic properties. The work of Hernandez-Andrade et al.[70] manifested that it is unprovable to experience spontaneous preterm birth when pregnant women score small strain values at the internal os. Molina et al.[39] determined that the internal os and inferior portions of the cervix were stiffer than the external os and superior portions, same conclusions were obtained by Hernandez-Andrade[70]. SWV was evaluated in multiple areas of the cervix, and authors found that SWV decreased with increasing gestational age only at the internal os. Muller et al. found a decrease in SWV in women hospitalized for preterm compared to a control group[71]. Carlson et al. work about measuring the SWV before and after prostaglandin ripening before term induction of labour in 20 women determined a significant difference in SWV was reported (2.53$\pm$0.75 m/s before and 1.54$\pm$0.31 m/s 4 hours after prostaglandin application). A comparison of SWV between women in the first trimester and the third one was also made. Average SWV for 1st trimester was 4.42$\pm$0.32 m/s and 2.13$\pm$0.66 m/s for 3rd trimester[11]. Rosado-Mendez et al.[72]suggested that shear wave elastography can be improved, taking into account the viscosity of the region. In their study, they determined the viscous component of the cervix via the quantification of the shear wave dispersion. Tests were done in the Rhesus macaque cervix. Shear wave group velocity showed no difference between the prostaglandin-ripened and unripened cervix. However, taking into account local microstructure and viscosity seem to improve the accuracy of the cervical evaluation. Design numerical models for the pregnant uterus and cervix are very complex. In addition, it depends on the properties of the medium. Some numerical works were reported by Fernandez et al. SWV is determined assuming

the tissue is homogeneous and have an elastic behaviour[73]. However, the cervix is viscoelastic. Additionally, even small changes in collagen fibre waviness and diameter and orientation affect shear wave propagation velocity and dispersion[74].

2.2. Cornea

The mechanical status of the cornea is governed nearly entirely by the stroma [75]. The other layers that compose this tissue are considered to have secondary contributions, as in the endothelium, which functionality is cornea hidratation[76]. The mechanical stability of the cornea is due to the collagen, whose fibrils form stacked lamellae. This form of the fibrils makes a mechanism to resist shear and tensile forces[77, 78]. Keratoconus and other pathologies as post-surgery ectasia are caused by significant variations in the organization of the fibrils of the collagen layer[79, 80]. The increase in global elasticity[81] is because of the construction of new crosslinks within the stroma, in a related process to corneal crosslinking treatment (CXL)[82, 83]. The cornea's principal function, simultaneously with the lens, is to redirect light to the retina[84]. Contrary to the lens, the cornea has a fixed focus and cannot change its geometry to improve it. Consequently, the cornea's pathologies due to changes at the microstructure level affect its refractive capacity[85]. Evaluating mechanical biomarkers of the cornea, especially elasticity, could help in early diagnosis since it has been confirmed that alterations in cornea properties occur before any of the macroscopically visible structural changes in a clinical examination[86, 87]. Furthermore, the cornea is a viscoelastic tissue, and recent research works are trying to identify distinct viscoelastic biomarkers of the cornea[88, 89]. Encouraged by encouraging results in other soft tissues, several studies employed remote palpation by acoustic radiation force (ARF) to obtain 2D elasticity maps[90, 91, 92, 93, 94]. Polarized shear waves were induced within the field of view of the transducer, and then the displacements or velocities were tracked at a high frame rate as the waves propagated. These approaches provided valuable information, mainly due to their high resolution (>15 MHz), generating images with high sensitivity at the micro-level. Still, for the time being, it is challenging to re-engineer a clinical set-up for its in vivo implementation, techniques that required transducer translation for imaging took tens of seconds, and the characterization of the applied acoustic force remains elusive, mainly due to the thin corneal geometry, where complex wave patterns governed by guided waves could bias the results[95]. Lastly, optical coherence elastography (OCE) stands as the most prolific technique in terms of publications[96, 97]. Studies used optical coherence tomography,

where light-scattering measurements provided structural imaging, whereas OCE detected particle tissue displacements generated by mechanical loading to deduce viscoelastic parameters taking into account stress information. Its main advantages were the microscale resolution of the images and the microscale sensitivity in motion detection and the noncontact approach. Even so, it was not exempted from limitations, such as the low penetration depth, which was the trade-off for a micro-scale resolution (this was not a concern in the corneal application), long acquisition imaging times (>3 min), repeated stimulation that might lead to bias due to relaxation effects in the tissue and low frame rate in 2D imaging[98, 99].

2.3.Viscoelasticity of soft tissue

From the mechanical viewpoint, two phenomena contribute to the time-dependent or rheological behaviour of soft tissues: viscoelasticity and poroelasticity [100]. Although both viscosity and porosity contribute additively to the same phase lag between stress and strain dynamics, they are commonly quantified as an unique value called viscosity within the elastography community. However, viscoelasticity and poroelasticity stem from fundamentally different origin and are only separable playing with space and time scales. In other words, at large-size scales, tissues are viscoelastic in the short-time period and poroelastic in the long-time period, whereas the small-size scales, tissues are poroelastic in the short-time period and viscoelastic in the long-time period [101], which is clinically intractable given the limited region and frequency ranges. For this reason, it might be appropriate to rename viscoelastic elastography to rheological or dynamic elastography.

Soft tissues are generally assumed to be decomposed into their porous solid phase and their fluid phase [102]. The high fluid content in tissues is combined with the poroelastic structure of the ECM to allow motion between components under load, creating a time delay in the strain and triggering the viscoelastic response [103]. This biphasic nature implies a phase lag between the stress and strain associated with a relaxation time, or in the case of oscillatory mechanical tests, a phase angle. Then it would be advisable to start considering time-dependent effects since the strain response to load and unload conditions is a function of time, often called the velocity of deformation. During the loading cycle there is dissipation of energy, reflecting the existence of hysteretic effects. At the same time, the strain evolution is slowed to allow the viscous flow to settle. Thus, the duration and rate of loading define the dynamics of the tissue strain. Without this characteristic the stress during physiological activities would be harmful to the active structure [104].

One of the key features of viscoelastic tissues comes from the physics of wave propagation, where the dispersion is defined as a compound expression of the poroelastic and microstructural media governed by the complex fibrous multiscale microstructure of the stroma [105, 106, 107, 108]. It is also known that the amplitude and intensity of waves decays proportionally to the distance traveled. Added to a highly viscous environment, where the microvasculature and hemodynamics play an important role, it is observed that wave phase velocity changes with frequency, and wave amplitude is affected by geometric factors, such as boundary conditions and the size of scattering particles, similar or smaller than the wavelength [109]. Another important point is that the frequency-dependent behaviour complicates the comparison of different technologies since each author chooses a suited range [110]. Neglecting the viscous part introduces bias for the estimation of elasticity since the effect of wave dispersion is ignored.

The possibility of explaining these mechanical parameters by the internal structure and function of the tissue seems to be the key to improve the specificity of a pathology diagnosis. Collagen by itself exhibits a viscoelastic behaviour, attributed to fibre and fibril sliding and the crosslinking density, however, due to its short time of relaxation it seems that the global response is dominated by non-collagenous components [111]. Elastin has been found to contribute to stress relaxation, since when it was removed in arteries the relaxation time dropped significantly [112]. Nonetheless, PGs are considered as the main viscous constituents, embedding the collagen fibres, and creating a lubricating effect. Their hydrophilia generates hydrostatic pressure, which coupled with HA [113] and its large molecular size entails water attraction, filling the porous matrix [114]. The role of PGs and HA has been reviewed in tumor biology [115] and in inflammatory processes [116]. They are capable of acting as signaling pathways, interacting with diverse receptors, which affect the ultrastructure of the ECM that is transformed during inflammatory and neoplastic diseases [117]. In the case of pregnancy, as the time of delivery approaches, an inflammatory process is triggered, where the proportion of PGs to collagen increases, therefore higher viscosity is expected [29, 118, 30]. As for fibrosis disorders, there is an increased deposition of ECM constituents, especially collagen, accompanied by PGs and HA that help in cell signaling and proliferation [119]. A better understanding of these proteins and their relationship with viscosity might allow the development of concrete diagnostic and therapeutic strategies.

Similarly, higher smooth muscle cell (SMC) tone in the carotid wall has been linked to higher viscosity [120]. For its part, it has been seen that there is an increase in SMC in the internal os of the cervix as delivery approaches, and

at the time of the induction it became the most sensitive part [6], while in the liver, the development of fibrosis has been accompanied by an increase of SMC actin [121]. Investigations about the arterial viscoelasticity linked it to wall pressure [122]. From the perspective of tumours, there are changes at the cellular level, which promotes different reactions of the stroma. In breast, the viscosity of lesions has been studied in order to discriminate the nature of the masses [123, 124, 125, 126]. Higher viscosity was registered compared to healthy tissue and different ranges allowed to distinguish between benign and malignant lesions.

Thus far, most studies have ignored this behaviour, relying only on approaches based on linear elasticity simplifications. Although this has enabled progress to be made in quantitative imaging techniques, diagnoses sometimes fail because they do not deal with all the information. [127]. To reduce false-negative and false-positive results and to better understand pathological changes in soft tissues, extended dynamic mechanical parameters such as viscosity need to be investigated [128] and eventually be used as new diagnostic biomarkers. Ex vivo studies evidence the predictive relationship between viscosity and pathology, such as the marked ex vivo neuronal demyelination with development of apparent vacuoles associated with a loss of interneuronal connections and thus with a reduction of matrix dimensionality, causing an observed alteration of viscosity [129, 108, 130, 131]. The collected data from either traditional testing methods (creep and relaxation tests) or state-of-the-art imaging combined with the current computational power are allowing to retrieve viscous parameters from empirical or computational models.

It is important to note that if tissues are precompressed when they are examined, the estimation of parameters will be biased, as the time-dependency of the response is relevant. Changes over time due to mechanical stimulation are attributed to rapid alterations in cellular activity, mainly the synthesis and modification of components of the ECM (collagen and proteinases) [132]. To avoid this situation, preconditioning protocols should be proposed whenever the specimen studied allows it, so that a stabilization in the response is achieved [133]. With the aim of capturing this material behaviour, the most popular approach considers soft tissues as uniphase solids and its response to external loads or deformation is represented as a lumped relationship. This method uses linear viscoelastic models that generally include a solid-related characteristic (e.g., spring) and a viscous fluid element (e.g., dashpot). To name a few, Maxwell, Kelvin-Voigt (KV) and Zener viscoelastic models provide information on how the different scales are linked to each other [134, 135]. However, in order to fit a model when the soft

tissue shows several characteristic times, generalized linear viscoelastic models are used, such as generalized Maxwell or KV models [136, 137]. When large strains are expected, these linear models are not suitable, thus it is frequently adopted the proposed Fung's quasilinear viscoelastic model [138].

One of the most used models in the literature to fit the parameters is the KV model due to its simplicity [139]. Other models have been explored, such as Maxwell, fractional derivative versions of the above, or combined models such as the springpot model [140]. The KV formulation in terms of the stress tensor equation:

$$\sigma_{ij} = -p\delta_{ij} + \tau_{ij} \qquad p = -1/3\sigma_{kk}$$

assuming constitutive and viscous linearity have been derived with the aim of simplifying equations [141]. Following the references found in the literature [142, 143, 144],

$$\begin{aligned} p &= 3Kv + 3\eta^v \dot{v} \\ \tau_{ij} &= 2\mu d_{ij} + 2\eta \dot{d}_{ij} \end{aligned} \tag{2.3.1}$$

where K is the compressional modulus and η and η^v are the shear and volumetric viscosities, respectively, and $\dot{v}$ and $\dot{d}_{ij}$ are the derivate of the volumetric and deviatoric strains, respectively.

Assuming incompressibility, only deviatoric components ($\tau_{ij}, \quad p = \nu = 0$) are considered. According to the schematic representation of the KV model, the total stress is the sum of the elastic and viscous terms,

$$\sigma_{ij} = \tau_{ij} = 2\mu d_{ij} + 2\eta \dot{d}_{ij} = 2\mu \epsilon_{ij} + 2\eta \dot{\epsilon}_{ij} \tag{2.3.2}$$

Following the same steps as in the Kelvin-Voigt model, the implementation of the Maxwell model stems from the strain tensor of Equation:

$$\varepsilon_{ij} = -v\delta_{ij} + d_{ij} \qquad v = -1/3\varepsilon_{kk}$$

For the same reasons stated for the KV case ($d_{ij}, \quad p = \nu = 0$), exclusively deviatoric components are considered. Only elastic and viscous components of the deviatoric term of the strain tensor are adopted,

$$d_{ij} = \tau_{ij}/2\mu, \quad \dot{d}_{ij} = \tau_{ij}/2\eta \tag{2.3.3}$$

The constitutive equation for this model is obtained by adding the elastic and viscous terms by,

$$\dot{d}_{ij} = \dot{\tau}_{ij}/2\mu + \tau_{ij}/2\eta \tag{2.3.4}$$

All this evidence suggests that the viscous phase may become a biomarker for the characterization of microstructural changes [145, 146, 147, 148, 149].

2.4. Transverse wave propagation on bounded media

Previous studies have shown a close relationship between the optical system's visual function and the cornea's biomechanical properties [150]. Consequently, it is of immense interest to precisely determine these biomechanical biomarkers. For this, and when employing ultrasound elastography for tissue characterization, and due to corneas geometry (thickness of about 1mm) and position (enclosed by a softer and viscous fluid), the cornea is considered a plate-like tissue since the wavelength (λ 1-10cm) is way superior to its thickness [92, 91]. This consideration raises the concern that the relationship between wave velocity(c_s) and elasticity (E) does not follow the classical (pure) formula of $E = 3\rho c_s^2$ being ρ the tissue density. This formula is usually accepted in bulky organs since shear waves attenuate before reaching the organ boundaries. However, in plate-like tissues, shear waves propagating in the tissue experience multiple reflections on the boundaries, provoking guided waves. In the case of the cornea, and when the viscoelastic soft tissue is surrounded by fluid, the phase velocity $c(\omega)$ of a leaky Lamb wave can be determined from:

$$c(\omega) = \sqrt{\frac{\omega\, h\, c_s}{2\sqrt{3}}} \tag{2.4.1}$$

Where ω is the angular frequency, h is the plate-like tissue thickness and c_s is the group velocity given by shear modulus μ and density ρ by the equation $c_s = \sqrt{\mu/\rho}$. Equation 2.4.1 is a corrected formula of the classical Lamb wave for a plate in vacuum by a factor of $(1/\sqrt{2})$ due to the leakage of longitudinal waves at the wall interfaces [95].

2.5.Shear wave propagation in anisotropic media

Anysotropy is everywhere, to see, to measure and to model! Anysotropy is rare!

With the currently available technology, the characterization of the anisotropy of soft tissue is totally challenging. Determining the shear wave velocity in ultrasound elastography can only be done in one direction at a time. Therefore it is needed to make multiple measurements with different probe positions/angles. Furthermore, a simple model is often considered when estimating the anisotropic ratio, the transversely isotropic model, but only a few organs have this type of symmetry. To determine the full anisotropic tensor, we need technological development to access volumetric measurement of shear wave propagation[151]. The theory of elasticity studies the behaviour of solids with thermodynamically reversible deformations and independent of the deformation rate. If the outcome of the sum of actions is equal to the sum of the individual effects and the outcome of one action multiple of another is the exact multiple of the result of the mentioned action, the solid will be a linear system, and its behaviour will be studied using the linear elasticity theory. Even though most elastic solids have a non-linear behaviour, in reality, it is widespread to assimilate them to linear systems due to the regularity of their results and the predictability of their operation. Although the first expression of Hooke's law of evidence dates from the XVII century, the classical theory of linear elasticity was not developed until the XIX century, by Cauchy, Navier, Poisson, Green or Saint-Venant. The constitutive equations of linear elasticity were established in the first half of the XIX century. However, they gave rise to a long discussion about the number of independent elastic constants necessary to define material behaviour (15 or 21 in the general case, 1 or 2 for isotropic materials). This controversy was not resolved until the beginning of the XX century when it was accepted that in the general case, the tensor contains 21 independent elastic constants [152].

The fundamental equations of linear elasticity in a rectangular Cartesian coordinate system $(x1, x2, x3)$ are the equilibrium equation

$$\sigma_{ij,j} - \rho \frac{\partial^2 u}{\partial t^2} + F_i = 0 \tag{2.5.1}$$

The constitutive equation

$$\sigma_{ij,j} = C_{ijkl} \varepsilon_{kl} \tag{2.5.2}$$

and the behaviour equation

$$2\varepsilon_{kl} = u_{l,k} + u_{k,l} \tag{2.5.3}$$

where $\sigma_{ij} = \sigma_{ji}$ are the components of the symmetric stress tensor, $\varepsilon_{ij} = \varepsilon_{ji}$ are the components of the strain tensor, c_{ijkl} are the components of the fourth order tensor of elastic constants, u_i are the components of the displacement vector, F_i are the components of the force vector, ρ is the density of the material and t is time. The relationship established in 2.5.2 can be reversed

$$\varepsilon_{ij} = S_{ijkl}\sigma_{kl} \tag{2.5.4}$$

where S_{ijkl} is related to C_{ijkl} by the expression $S_{ijkl}\, C_{klrs} = \delta_{ijrs}$.

The strain energy for anisotropic materials is

$$2\Phi = C_{ijkl}\varepsilon_{ij}\varepsilon_{kl} = S_{ijkl}\sigma_{ij}\sigma_{kl} \tag{2.5.5}$$

Substituting 2.5.2 and 2.5.3 in 2.5.1 the equation of equilibrium in displacements is obtained

$$E^*_{ijkl}u_{j,kl} - \rho\frac{\partial^2 u}{\partial t^2} + F_i = 0 \tag{2.5.6}$$

$$E^*_{ijkl} = (E_{iklj+E_{ilkj}})/2 \tag{2.5.7}$$

When solving particular problems, equations 2.5.1, 2.5.2, 2.5.3 and 2.5.6 are complemented with initial and boundary conditions. From 2.5.1 and 2.5.6 the equations of equilibrium are obtained under static conditions

$$\sigma ij + F_i = 0 \tag{2.5.8}$$

$$E^*_{ijkl}u_{j,kl} + F_i = 0 \tag{2.5.9}$$

Let n_i and m_i $(i = 1, 2, 3)$ be two unit orthogonal vectors. Young's modulus E_n at address n_i has the form

$$1/E_n = n_i n_j S_{ijkl} n_k n_l \tag{2.5.10}$$

The Poisson modulus nu_{mn} in the direction m_i for an applied stress in the direction n_i is

$$\nu_{mn}/E_n = -m_i m_j S_{ijkl} n_k n_l \tag{2.5.11}$$

The shear modulus G_{nm} between areas with n_i and m_i normal is

$$1/(4G_{nm}) = n_i m_j S_{ijkl} n_k m_l \tag{2.5.12}$$

The compressibility modulus K can be expressed as $1/K = S_{ijkl}$

Soft tissues can be modelled for study as transversely isotropic materials since they have a direction (the preferential orientation of the fibres) such that in planes perpendicular to it, their behaviour is isotropic. This class of materials only have five independent elastic constants. In this case, the constitutive equation can be expressed as

$$\begin{pmatrix} \sigma_{11} \\ \sigma_{22} \\ \sigma_{33} \\ \sigma_{44} \\ \sigma_{55} \\ \sigma_{66} \end{pmatrix} = \begin{pmatrix} C_{11} & C_{11}-2C_{66} & C_{13} & & & \\ C_{11}-2C_{66} & C_{11} & C_{13} & & & \\ C_{13} & C_{13} & C_{33} & & & \\ & & & C_{44} & & \\ & & & & C_{44} & \\ & & & & & C_{66} \end{pmatrix} \begin{pmatrix} \varepsilon_{11} \\ \varepsilon_{22} \\ \varepsilon_{33} \\ \varepsilon_{44} \\ \varepsilon_{55} \\ \varepsilon_{66} \end{pmatrix} \tag{2.5.13}$$

The elastic properties of the material and its density determine the speed of propagation of mechanical waves through it. We will focus on the case of shear waves as they are the most used for tissue characterization and those used in this work. The equation that relates the various parameters are obtained from the constitutive equation and the motion equation, assuming plane waves and taking into account the symmetries of transversely isotropic

material. Thus, the speed of propagation of the wave is obtained from the expression

$$\rho c_s(\theta) = \frac{C_{44}C_{66}}{C_{44}sen^2(\theta) + C_{66}cos^2(\theta)} \tag{2.5.14}$$

where θ is the angle between the wave propagation direction and the fibre direction, c_s is the wave propagation speed, ρ is the density, C_{44} is the longitudinal shear modulus and C_{66} is the transverse shear modulus [**?**].

The values of the shear modulus G in the principal directions can be obtained using the simplified expressions

$$G(0) = C_{44} = \rho c_s^2(0) \tag{2.5.15}$$

$$G(90) = C_{66} = \rho c_s^2(90) \tag{2.5.16}$$

In order to obtain the G modulus, it is necessary to start from the wave velocity in the material. However, it is not measured directly but is calculated from the time t that the wave takes to travel a known distance d.

$$c_s = \frac{d}{t} \tag{2.5.17}$$

When measuring the time of flight of the signal, it must be considered fundamental to know the time needed by the wave to travel through the specimen material. Since, in general, the signal is not generated or received at the interface between the sensor and the sample, it is also necessary to take into account the time that the wave takes to travel through the measuring device itself. This time is called internal delay and is a specific value of each measuring device and must be rested from the measured value to obtain the calculated time.

2.6.Non linear shear elasticity

One of the main hypotheses about the pathology-mediated origin of nonlinearity changes is based on the nonlinear character of the strain response. The organization of collagen fibres and elastin, as well as their amounts, combined with the synthesis and degradation processes that are experienced due to growth and remodelling enhance the nonlinear behaviour [153, 154].

Additionally, the stress-strain behaviour of the stroma is nonlinear between tension and compression, with a stiffer response and reduced extensibility in tension, and a more compliant response in compression [25, 155].

Several experimental evidence, including the recent study of Aristizabal et al. [128], estimates the nonlinear shear modulus in ex vivo samples. Particularly, this paper is about ex vivo kidneys to diagnose end-stage renal disease, where a better contrast in the diagnosis is showed. Based on the principle of acoustoelasticity, the feasibility of obtaining nonlinear parameters through changes in the deformation and its consequent interaction with the propagated wave is proved. The application of a deformation and the use of radio frequency ultrasonic signals to quantify it, was the work of Goenezenet al. [156], where they obtained spatial maps of nonlinear elastic parameters in patients with malignant and benign tumours. Their conclusions highlight a greater magnitude in the case of malignant tumours. In the context of preterm birth assessment, Myers et al. [25] investigated the interaction between mechanical and chemical properties of several cervical samples from different human hysterectomy specimens: non-pregnant patients with previous vaginal deliveries; non-pregnant patients with no previous vaginal deliveries; and pregnant patients at time of cesarean section. The samples were tested in confined compression, unconfined compression and tension. Results indicated that cervical stroma has a nonlinear behaviour that could be explained with an accurate multi-scale model.

The significant hyperelasticity that soft tissues exhibit can manifest itself as quantifiable shear wave harmonic generation (via ultrasonic shear elastography), considering that the stored strain energy is variable with the fibre orientation. Taking this opportunity, an efficient application of nonlinear or hyperelastic constitutive equations for either finite element analysis or experimental analysis require the derivation of a strain energy function to consider adequate stress and strain relationship. A diversity of approaches on nonlinear mechanics have been developed since Landau and Murnaghan [157, 158] which are particularly well-suited for nonlinear wave modelling, until the last proposals lead by Ogden, Mooney-Rivlin, Yeoh or Fung [159, 160] which covers adjustment theories based on modelling of physiological mechanics [161].

Although the nature of soft tissue behaviour is viscoelastic [138], a simplification of hyperelasticity allows a reasonable characterization of the mechanical properties, specifically when the loss of strain energy is small (low loading rates). Veronda and Westmann [162] and Fung [163] were the first works that used hyperelasticity for soft tissue modelling. The hyperelastic approach postulates the existence of the strain energy function, which relates

the displacement of the tissue to the corresponding stress values [164]. The most common strain energy functions for the modelling of soft tissues are polynomial forms, such as Mooney–Rivlin and Ogden models. Many authors have modelled the behaviour of soft tissues such as, porcine spleen, porcine kidney, porcine liver, rat or human brain [165, 166, 167, 168, 169]. Regarding cervical tissue, uniaxial tension tests [170, 171, 172, 173, 174] and compression [172, 175, 176] have been studied in rat tissue and human tissue using load-relaxation protocols. The nonlinear stress-strain response has been shown in the tension, and compression tests and tissue response were noticeably stiffer in tension than in compression. It was observed that tissue from pregnant patients was one to two orders of magnitude more compliant than tissue from nonpregnant patients [172, 176]. In work carried out by Yoshida et al. [174], load relaxation ring tests were performed on pregnant and nonpregnant rat cervices. The pregnant tissue showed a considerable stress relaxation compared to the nonpregnant tissue. Myers et al. observed that the cervix stiffness changes along its length in the uniaxial tensile test, where the external os had a stiffer response than the internal os [172]. The relationship between stiffness and gestational age was studied by Poellmann et al., and Jayyosi et al. [173, 177]. The works concluded that stiffness decreased as gestational age increased. In the works mentioned above were uniaxial, compression and traction tests were performed, the mechanical properties of the tissues have been obtained. However, in those works, the nonlinear elastic properties of ex vivo human cervical tissue, using the Fourth Order Elastic Constants (FOECs), Ogden, and Mooney-Rivlin models, have not been obtained through uniaxial tensile tests yet.

Soft tissues are composed of several layers; each of these layers has different compositions. For instance, cervical tissues have an outer epithelial layer and a connective layer. The connective layer is composed of an extracellular matrix (ECM) that ensures the strength and integrity of the cervix, resisting shear deformation, through a fibrous scaffold [178]. The main component of the ECM is fibrillar collagen, which determines a cross-linked network interlaced with the elastin protein, enclosed by a ground substance of proteoglycans and glycosaminoglycans [179, 180, 181]. Researchers have identified three zones of structured collagen in the connective layer: the innermost and outermost rings of stroma contain collagen fibres preferentially aligned in the longitudinal direction. The middle layer contains collagen fibres preferentially aligned in the circumferential direction [182, 183]. Regarding the collagen content, the intermediate zone had higher levels of collagen content when compared with the inner and the outer zones [183]. According to the mechanical studies on soft tissues, the connective layer is often considered as

the most important from a mechanical point of view [184, 185, 186]. However, other studies, based on Torsional Wave Elastography, consider the epithelial layer as a key apart from the connective one [187, 134, 188]. The reason is that torsional waves not only propagate in-depth but along the surface before being registered by the receiver. One of the purposes of this section is to study the differences in stiffness between the epithelial and connective layers of ex vivo human cervical tissue that comes from the hyperelastic models employed.

Theory of Hyperelastic Models

This section shows the theoretical relationship between stress and strain for a proposed hyperelastic model based on the FOEC in the sense of Landau's theory, Mooney-Rivlin and Ogden models.

2.6.1.Proposed Fourth Order Elastic Constants Nonlinear Model

Nonlinear FOECs are defined in the sense of Landau's theory [189] to establish a strain energy function, considering the medium incompressible valid for the hyperelastic regime as defined Hamilton and Destrade [190, 191],

$$\mathbf{W} = \mu I_2 + \frac{1}{3} A I_3 + D I_2^2 \tag{2.6.1}$$

where $I_1 = \mathrm{tr}\boldsymbol{E}$, $I_2 = \mathrm{tr}\boldsymbol{E^2}$ and $I_3 = \mathrm{tr}\boldsymbol{E^3}$ are the classical invariant of deformation defined by Cemal et al. [192],$\boldsymbol{E}$ is the Green strain tensor, μ is the shear modulus and A and D are the Third and Fourth Order Elastic Constants of Landau respectively. The Second Piola-Kirchoff stress tensor is determined by a constitutive law as follows,

$$\boldsymbol{S} = \frac{\partial \boldsymbol{W}}{\partial \boldsymbol{E}} \tag{2.6.2}$$

where $\boldsymbol{E}$ is the Green–Cauchy strain tensor defined in terms of displacement field as the difference between actual and initial position respectively, $\boldsymbol{u} = \boldsymbol{x} - \boldsymbol{X}$. This strain tensor is defined, according to the large deformation theory, as,

$$\boldsymbol{E} = \frac{1}{2}((\nabla_X \boldsymbol{u})^T + \nabla_X \boldsymbol{u} + (\nabla_X \boldsymbol{u})^T + \nabla_X \boldsymbol{u}) \tag{2.6.3}$$

Under the hypothesis of a tensile test set-up, the initial conditions are described in Figure 2.3.

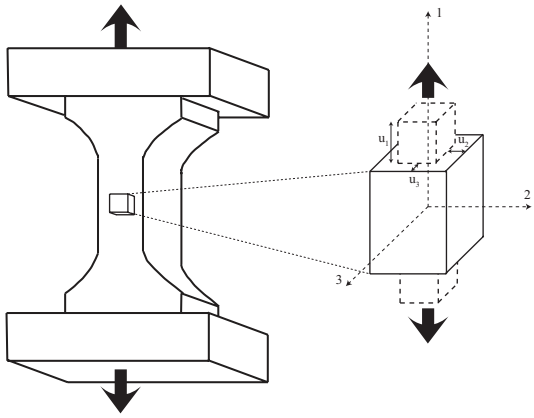

Figure 2.3: (**Left**): scheme of the uniaxial tensile test. (**Right**): zoom of a differential element of the sample. Adapted from [2] (CC BY 4.0.)

where the displacements are defined in three directions as,

$$\begin{aligned} u_1 &= ax_1 \\ u_2 &= -bx_2 \\ u_3 &= -bx_3 \end{aligned} \tag{2.6.4}$$

In this case, the Green–Cauchy strain tensor defined in Equation (2.6.3) may be described in matrix form as,

$$\boldsymbol{E} = \begin{pmatrix} a + \dfrac{1}{2}a^2 & 0 & 0 \\ 0 & -b + \dfrac{1}{2}b^2 & 0 \\ 0 & 0 & -b + \dfrac{1}{2}b^2 \end{pmatrix} \tag{2.6.5}$$

To describe the Second Piola–Kirchoff stress tensor in a nonlinear regime, it is necessary to determine the invariant I_3 in terms of strains.

$$\begin{aligned} I_3 &= E_{11}^3 + E_{22}^3 + E_{33}^3 \\ \frac{\partial I_3}{\partial \boldsymbol{E}} &= \begin{pmatrix} 3E_{11}^2 & 0 & 0 \\ 0 & 3E_{22}^2 & 0 \\ 0 & 0 & 3E_{33}^2 \end{pmatrix} \end{aligned} \tag{2.6.6}$$

The constitutive law for tensile test case in direction 1 is deduced by the

expression,

$$S_{11} = 2\mu a + (\mu + A)a^2 + (A + 4D)a^3 \tag{2.6.7}$$

The relationship between the Cauchy stress tensor and the Second Piola–Kirchoff stress tensor is defined as,

$$\boldsymbol{\sigma} = \boldsymbol{J}^{-1}\boldsymbol{F}\boldsymbol{S}\boldsymbol{F}^{T} \tag{2.6.8}$$

where $\boldsymbol{F}$ is the deformation gradient tensor and $\boldsymbol{J} = det(\boldsymbol{F})$.

The derivation of Cauchy stress tensor in the context of weakly nonlinear elasticity [155] yields the constitutive law defined in high order as follows,

$$\sigma_{11} = 2\mu a + (5\mu + A)a^2 + (7\mu + 3A + 4D)a^3 + \left(\frac{5}{2}\mu + 3A + 8D\right)a^4 + \frac{5}{2}(A + 4D)a^5 \tag{2.6.9}$$

In order to compare with the other two hyperelastic models, the aforementioned tensor is simplified (using μ and A) as follows:

$$\boldsymbol{\sigma_{NL}} = 2\mu a + (5\mu + A)a^2 \tag{2.6.10}$$

where a is defined in Equation (2.6.4).

2.6.2.Mooney-Rivlin Model

The Mooney–Rivlin model, originally derived by Mooney in 1940 [193] was formulated in terms of the Cauchy–Green deformation tensor invariants by Rivlin [194] as:

$$\boldsymbol{\Psi} = \sum_{i=1}^{2} c_i \left(I_i - 3\right) \tag{2.6.11}$$

where c_1 and c_2 are the material parameters, I_1 and I_2 the first and second strain invariants respectively and Ψ the strain energy function.

In the case of an uniaxial tension ($\sigma = \sigma_1$, $\sigma_2 = \sigma_3 = 0$) the Cauchy stress as a function of the strain invariants is

$$\boldsymbol{\sigma} = 2\left(\lambda^2 - \frac{1}{\lambda}\right)\left(\frac{\partial \boldsymbol{\Psi}}{\partial I_1} + \frac{1}{\lambda}\frac{\partial \boldsymbol{\Psi}}{\partial I_2}\right) \tag{2.6.12}$$

where $\lambda = \lambda_1$ (λ_1 is the principal stretch in 1 direction) and the invariants from the Cauchy–Green tensor for an incompressible hyperelastic material

subjected to a uniaxial tension are defined as [195],

$$\begin{aligned} I_1 &= \lambda^2 + \frac{2}{\lambda} \\ I_2 &= 2\lambda + \frac{1}{\lambda^2} \\ I_3 &= 1 \end{aligned} \tag{2.6.13}$$

For the Mooney–Rivlin model, the Cauchy stress obtained employing (2.6.12) and using two parameters (c_1 and c_2) is,

$$\boldsymbol{\sigma}_{\text{ Mooney}} = 2\left(\lambda^2 - \frac{1}{\lambda}\right)\left(c_1 + c_2\frac{1}{\lambda}\right) \tag{2.6.14}$$

2.6.3.Ogden Model

The strain energy function in the Ogden model, developed in 1972 [196], is described by,

$$\boldsymbol{\Psi} = \sum_{r=1}^{N} \frac{\mu_r}{\alpha_r}\left(\lambda_1^{\alpha_r} + \lambda_2^{\alpha_r} + \lambda_3^{\alpha_r} - 3\right) \tag{2.6.15}$$

where μ_r (infinitesimal shear modulus) and α_r (stiffening parameter) are material constants, and λ_1, λ_2 and λ_3 are the principal stretches. Taking into account that for an incompressible material, $\lambda_1 = \lambda$ and $\lambda_2 = \lambda_3 = 1/\sqrt{\lambda}$ [195], Equation (2.6.15) is simplified into,

$$\boldsymbol{\Psi} = \sum_{i=1}^{N} \frac{\mu_r}{\alpha_r}\left[\lambda^{\alpha_r} + 2\left(\frac{1}{\sqrt{\lambda}}\right)^{\alpha_r} - 3\right] \tag{2.6.16}$$

The Cauchy stress tensor as a function of the principal stretches for an incompressible material is,

$$\sigma_1 = \lambda_1\frac{\partial \boldsymbol{\Psi}}{\partial \lambda_1} - \lambda_3\frac{\partial \boldsymbol{\Psi}}{\partial \lambda_3} \tag{2.6.17}$$

Finally, using Equation (2.6.17), the Cauchy stress using two parameters (μ_r and α_r) is obtained as follows,

$$\boldsymbol{\sigma_{Ogden}} = \mu_r\left(\lambda^{\alpha_r} - \lambda^{-\alpha_r/2}\right) \tag{2.6.18}$$

The shear modulus μ in the Ogden model results from the expression,

$$\mu = \frac{\mu_r \alpha_r}{2} \tag{2.6.19}$$

Part II

METHODOLOGY

"I am among those who think that science has great beauty. A scientist in his laboratory is not only a technician: he is also a child placed before natural phenomena which impress him like a fairy tale."

Marie Curie

Chapter3

Torsional Wave Elastography (TWE)

The World Health Organization (WHO) estimated in 2017 that approximately 15 million babies would be born preterm (<37 weeks of gestation), this is a rate above 1 in 10 newborns [6]. The problem of cervical insufficiency is intimately related to the mechanical properties of the cervix, and hence any approach must involve means to quantify the biomechanical state of the cervix. The mechanical parameters are sensitive to the collagen remodelling that progresses throughout cervical ripening, and which ultimately controls the cervix's mechanical ability to dilate [197].

Although the SWEI technique has been effective in the cervical tissue description, it presents some limitations: first, shear waves are highly attenuated due to the microstructural complexity of the cervix, and secondly, the complexity of producing adequate shear waves in its boundaries. The use of torsional waves (shear elastic waves that propagate radially and in-depth in a curved geometry to sense soft tissue architecture) has been demonstrated to enable a new class of characterization to quantify the mechanical functionality of any soft tissue [198, 199, 200, 201].

Given these limitations, Melchor et al. [202] and Callejas et al. [134] introduced a novel technique, Torsional Wave Elastography (TWE). The method is based on the transmission of shear waves by a rotational electromechanical actuator and received by a sensing ring. One of the advantages of this technique when compared with SWEI, is that it is highly adequate for cylindrical, small organs, like uterine cervix, since TWE generates low energy that does not generate rebounds as SWEI. Torsional wave elastography was used to quantify the stiffness of cervix in pregnant women in vivo by Masso et al. [186]. Preliminary results reveal that TWE could become an advantageous technique capable of quantifying the decrease of cervical stiffness during gestation.

This configuration is shown to be particularly efficient in minimizing spurious

p-waves components and is sensitive to mechanical constants, especially in cylinder-shaped organs.

Application of torsional waves to sense soft tissue architecture has been proved to enable a new class of biomarkers that quantify the mechanical functionality of any soft tissue [203]. Abnormalities in the structural architecture of soft tissues are intimately linked to a broad range of pathologies, including solid tumours, atherosclerosis, liver fibrosis, and osteoarticular syndromes [53]. The unexplored nature and applicability span of these mechanical biomarkers and torsional waves provides an exciting diagnostic technology. The need for comparative and repetitive studies is clear. Validation studies are demanded of emerging techniques. This is due to the increased interest in the viscoelastic parameters obtained from elastography techniques [204].

In this dissertation, the generation and detection of torsional waves through the proposed technology (TWE) developed by our group [205, 206] was used to obtain mechanical biomarkers in terms of shear wave velocity and shear moduli of **ex vivo soft tissue**.

Torsional wave elastography was validated against; (1) Shear Wave Elasticity Imaging (SWEI) technique through the determination of shear wave velocity, shear moduli, and viscosity of ex vivo chicken liver, breast, tissue mimicking hydrogel phantoms, porcine cornea and ex vivo uterine human cervical samples, (2)Via mechanical tests.

3.1.Sensor design

3.1.1.Isotropic TWE sensor: configuration for bulk tissue

The torsional wave sensor is based on a novel arrangement of concentric sandwiches of piezo- and electromechanical elements. The emitter transmitting the waves consists of a PLA (polylactic acid) disk, printed in 3D, whose rotational movement is due to an electromechanical actuator. The receiver is formed by two PLA rings with four slots in the inner face of the ring, where the four ceramic piezoelectric elements are fitted [207, 208, 187]. This allows the precise interrogation of soft tissue mechanical functionality in cylindrical geometries. Dealing with this type of geometry is a challenge for current elastography approaches in small organs.

Figure 4.3 shows the TWE probe developed by our group. The left sub-figure shows the sensor encapsulated in a CNC (computer numerical control) system that allows measuring within an exact position and at the same time exerting a controlled pressure on the sample. The right sub-figure shows a

cross-section of the TWE probe. More details of the probe can be found in the work of Callejas et al. [134].

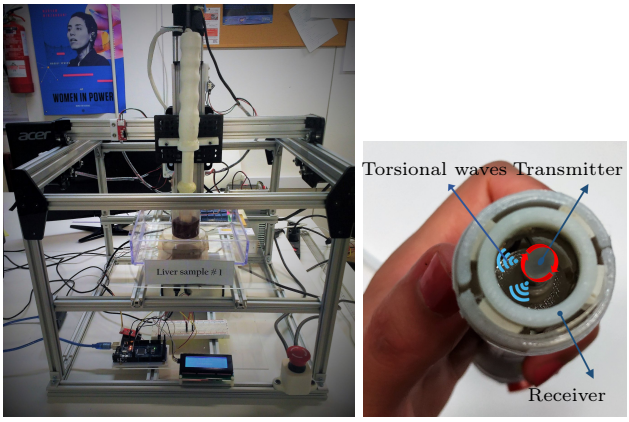

Figure 3.1: Set-up for measurements using TWE technique. The picture was taken during the measurements at the Ultrasonics Lab at the University of Granada. The figure on the left is a computer numerical control (CNC) system for positioning and pressure-control of the TWE probe. The right figure shows a cross-section of the TWE probe. Adapted from[3].

3.1.2.Isotropic TWE sensor: configuration for plate-like tissue: Cornea

To determine the viscoelatic biomarkes of the cornea (a plate-like tissue) some modifications to the TWE sensor for bulk tissue were done. The dimensions and geometry of the contacting receiving ring were selected to match the samples[209]. The external and internal diameters were 13 mm and 9.6 mm, respectively, with an internal curvature that covered the corneal shape completely, as shown in Figure 6.3. This set was assembled in a casing with mechanical attenuators that also centered the emitting disk relative to the receiving ring. All the components were 3D printed using a biocompatible photopolymer resin (MED610, Stratasys Inc., Eden Prairie, MN, USA) except for the casing that was printed in PLA (polylactic acid).

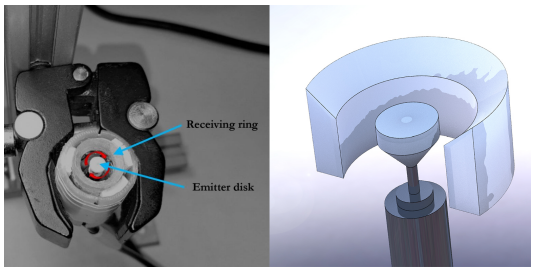

Figure 3.2: The Left subfigure shows the TWE sensor for cornea. Right subfigure shows a 3D render of the probe.

3.1.3.Anisotropic TWE sensor

The anisotropic TWE sensor design, ensemble and calibrating is different from the previous two designs. The receiving part consists of several elements assembled in a ring-shaped structure, printed in 3D using the same biocompatible photopolymer as the conical transmission element. The lower element consists of a complete ring from which six columns emerge to serve as lateral support for the upper parts. There are three slots arranged to form 0, 90 and 225 degrees (Figure 3.3), aiming to measure parallel to a selected fibre direction, perpendicular to it and an intermediate orientation, respectively. Each piezoelectric element is independently connected in an inner face slot using conductive silver resin. The assembly of the receiver is completed applying the same method in the upper part, which will contact the sample, except that there are three arcs of the circumference with a thickness equal to the lower ring. Therefore, each piezoelectric element is in contact with its electrodes, obtaining different signals according to the sensor orientation. The excitation and reception parts are assembled in a PLA casing printed in 3D. This element ensures the device's performance by keeping the contacting surface of the emitter and receiver in the same plane and relatively centred. Several attenuators fix the parts in their corresponding places to control mechanical cross-talk, conferring robustness to the final design.

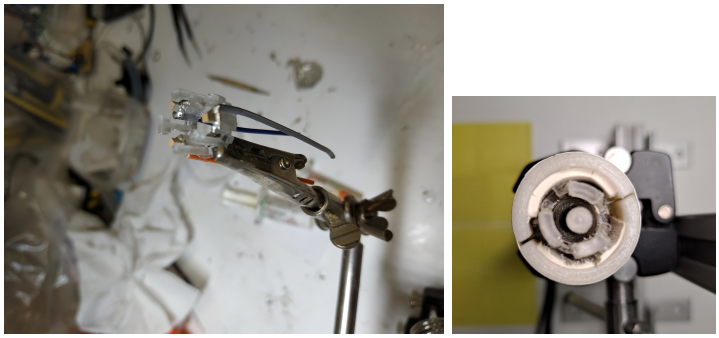

Figure 3.3: The left subfigure shows the inner TWE anisotropic sensor components. The right subfigure shows finished anisotropic probe.

3.2. TWE measurements

A multichannel AD/DA converter with 24 bits and 192 kHz sampling rate was used to generate and record the received signals. In principle, this sampling frequency increased the maximum wave speed limit sensitivity compared to ultrasound elastography modalities. The digital to analogical converter output a single sinusoidal pulse from 400 to 1400 Hz, the frequencies used in this work, connected to a sound amplifier (100 W) that transmitted a load of 25V peak-to-peak to the emitter. Immediately after that, the recording step started and the receiver's electrical signal was captured by a preamplifier (40 dB gain), to reach the AD converter, this set-up is illustrated in Figure 3.4. During this transition, no interfering effect between steps was observed. A 5 kHz low-pass filter was applied to the received signal to eliminate the high-frequency jitter. To reduce random noise, the resulting signal consisted of an average of 16 signals, acquired at 200 ms time intervals, for a total measured time of 3.2 seconds. Prior to measure the sample, a calibration signal was taken to counterbalance crosstalk effects. A dedicated algorithm was used to calculate the group shear wave speed, where the theoretical start of the received signal was estimated and used as the time-of-flight (TOF). All the elements were computer-controlled using high-speed communications ports and a Matlab environment (R2018b, The MathWorks Inc., Natick, MA, USA).

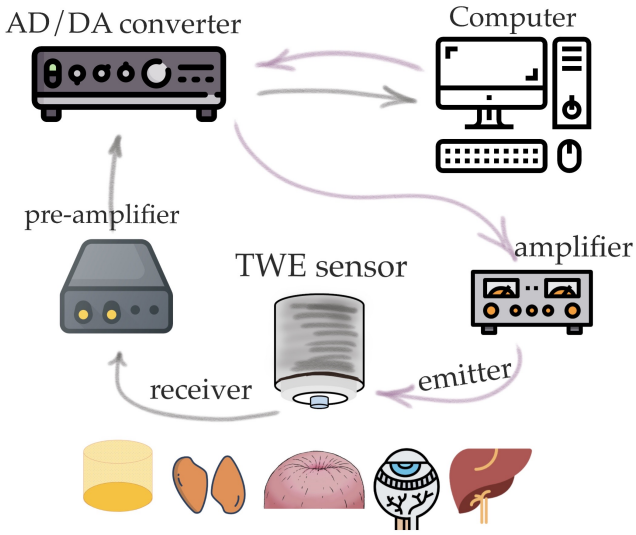

Figure 3.4: experimental set-up for tissue characterization using TWE.

3.3. Time of Flight (TOF)- Signal Processing

Physically, torsional waves are originated by the actuator and are transmitted through the specimens to the piezoelectric sensor, where they produce the deformation thereof and, consequently, an electric potential catchable by an oscilloscope.

To compensate for the mechanical and electronic crosstalk, a measurement is first taken in air, without contact with the specimen, which generates a signal transmitted mechanically inside the probe and electronically in air, under similar humidity conditions. This signal is stored and subtracted from the signals on the specimens, effectively compensating for the mechanical and electronic crosstalk. This signal is averaged 10 times for noise reduction, using a repetition rate that allows full dissipation of preceding waves. The total time of measurement is a quarter of a second, which is enough to register the desired frequency.

The remaining signal has travelled across the specimen and also through some mechanical parts of the probe. The apparent TOF is estimated from the subtracted signal as above, and after using a low pass filter at three times the center frequency, in three complementary ways: (1) by estimating the time where the signal amplitude surpasses 30% of the max level; (2) by finding the first peak after that threshold; and (3) by finding the next

negative peak, as indicated in Figure 3.6. The time of the theoretical signal start is estimated by subtracting the corresponding fractions of the period corresponding to the excitation frequency.

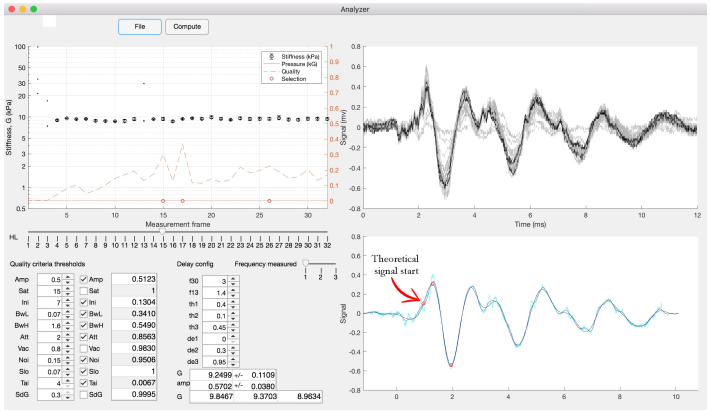

Figure 3.5: Example of an output of the analyzer software used to analyze the signals obtained from the TWE technique. The upper left sub-figure shows the stiffness obtained at each measurement frame. The lower-right sub-figure shows the theoretical signal start. Adapted from[3].

The apparent time of flight (TOF) is, therefore, the sum of the TOF within the specimen plus the TOF across the components of the probe, which is called internal delay. The latter is a probe-specific constant that needs to be calibrated against SWEI and subtracted prior to computing the speed by dividing the distance by TOF within the specimen (Equation (3.3.1)), yielding Equation (3.3.2). An example of the acquisition parameters for TWE technique used for ex vivo samples are shown in Table 4.1.

$$c_s = \frac{\text{distance}}{\text{TOF}} \tag{3.3.1}$$

$$c_s = \frac{\text{distance}}{\text{TOF} - \text{delay}} \tag{3.3.2}$$

Table 3.1
Example of torsional wave elastography (TWE) technique acquisition parameters for ex vivo soft tissue

Measurements Acquisition Parameters	**Value**
Sampling frequency	80 Hz (Decimated 10× after 800 Hz)
Ring-disc radius	3 mm
Frequency	200–800 Hz
Averaging	10 ×
Excitation power	20 V

3.4.Estimation of viscoelastic biomarkers

To characterize the viscoelasticity of the tissue given the dispersion curve, a rheological model is the most straightforward approach. The diligent task of identifying the best model is currently in discussion in the scientific community. Kelvin-Voigt, Maxwell, Zener a a fractional KV models were chosen in this work due to its widespread use in the literature [210].

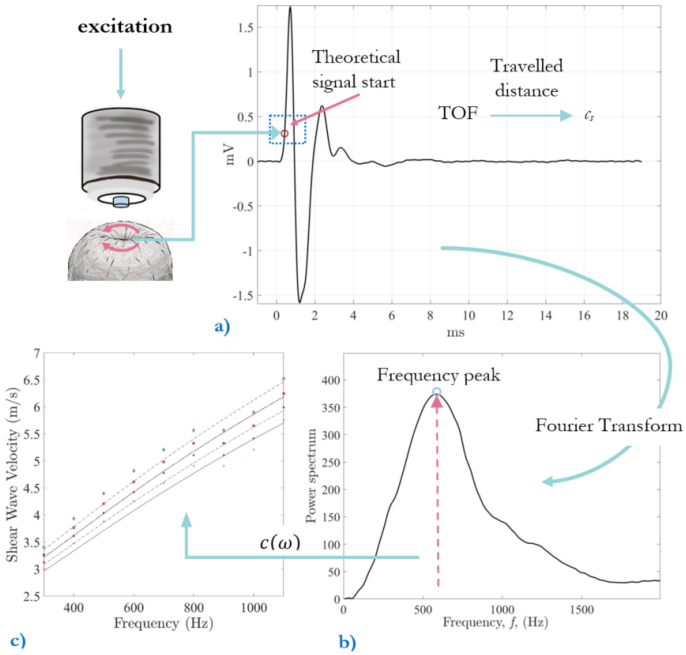

Figure 3.6: The scheme illustrates the workflow to calculate the dispersion curve from the measurements of TWE. First, a) the sample is excited and the received signal is collected, then with the theoretical signal starting point and the TOF algorithm the group shear speed is retrieved. b) a Fourier Transform is applied to this signal to get the power spectrum and the frequency peak. c) the shear wave speed dispersion curve is obtained using the frequency range where most of the energy is concentrated.

3.5.Safety considerations

Any new medical diagnostic device needs to satisfy the specifications described in the Food and Drug Administration (FDA) guidelines[211] for the application in clinical practice. Therefore, the torsional Wave Elastography technique need to accomplish these requirements to be safe for use in clinical applications on patients. Consequently, and for considering TWE safe to be used in Fetal Imaging and Other (FDA), three parameters should be evaluated according to the acoustic output: the mechanical index ($MI < 1.9$), the spatial peak pulse average intensity ($ISPPA < 190W/cm^2$), and the spatial peak temporal average intensity ($ISPTA < 94mW/cm^2$). The calculation

of these parameters was made as follows:

$$MI = PRP/\sqrt{Fc} \tag{3.5.1}$$

PRP is the peak rarefractional pressure of the torsional wave in (MPa), and Fc is the centre frequency (MHz).

$$ISPPA = P_0^2/(2 * \rho * c) \tag{3.5.2}$$

Where P_0 is the maximal acoustic pressure generated by the electromechanical actuator, ρ is the density of the medium, and c is the sound speed in the medium.

$$ISPTA = ISPPA * \Delta t/1 \tag{3.5.3}$$

Where Δt is the excitation pulse duration. The three parameters were experimentally evaluated. The excitation signal used was a low-frequency ultrasonic sine-burst at a central frequency of 1kHz, consisting of one cycle of 1ms and 16Vpp amplitude. This excitation signal was generated by a wave generator (Agilent 33220A, Santa Clara, CA, USA). The response signal was recorded using a decibel sensor (YH-610 Environment Multimeter). The signal travelled through a water layer before arriving at the decibel sensor and different distances from 5cm to 0cm. To convert the pressure recorded by the decibel sensor into water acoustic pressure, the equation that relates the impedances of the two media (air-water) was used:

$$T = \frac{2 * Z_{air}}{(Z_{air} + Z_{water})^2} \tag{3.5.4}$$

Where T is the transmission coefficient and Z_{air} and Z_{water} are the acoustic impedance of the air and water, respectively.

The maximum pressure recorded after converting the pressure reported by the decibel sensor into water acoustic pressure was $3.99x10^{-5}$ MPa. The maximal acoustic pressure and the peak rarefractional pressure of the torsional wave in water was $P0 = 3.99x10^{-4}$ bars, this calculatios were done by our group in the work of Masso et al. [186]. The three previous parameters were obtained with the cited experimental conditions:

$$MI = 0.0013 < 1.9 \tag{3.5.5}$$

$$ISPPA = P_0^2/(2 * \rho * c) = 5.3W/cm^2 < 190W/cm^2 \tag{3.5.6}$$

Considering the density of the medium $\rho = 1000kg/m^3$, and the sound speed in the medium $1500m/s$.

$$ISPTA = ISPPA * \Delta t/1 = 5.3W/cm^2 < 94W/cm^2 \tag{3.5.7}$$

The experiment results support that TWE technique is safe to be used in pregnant women. According to the Food and Drug Administration (FDA) guidelines reference parameters in Fetal Imaging and Other, all the values obtained were far below the thresholds.

3.6.Validation of TWE technique

3.6.1.Against SWEI

Acoustic radiation force imaging (ARFI) was introduced by Nightingale et al. [54]. This method uses focused ultrasound to generate localized displacement of a few microns via an ARF impulse within the tissue. During the impulse, the acoustic wave propagates through the tissue. Local displacements are related to the mechanical properties of the tissue, which deforms in response to the focused ARF excitation. Thus shear waves propagate away from it [55]. Finally, the displacement generated by the ARF is then mapped within the focal region of each push within a specified region of interest (ROI) at a known time after stopping the push. The tissue displacement response within the region of the push is directly related to the magnitude of the applied force and inversely related to the tissue stiffness [53, 54].

Shear wave elastography as ARFI also uses an ARF to excite the medium and generate shear waves and produces a quantitative elasticity map of the medium in real-time. The technique can be subdivided into the creation of the Mach-cone, where ultrasound beams are focused successively at different depths to create spherical waves at each focal point. The different generated spherical waves interfere constructively along a Mach-cone creating two quasi-plane shear wavefronts propagating in opposite directions in the imaging plane [212].

In this work Verasonics Vantage US research system (Vantage 256, Verasonics Inc., Redmond, WA, USA) generates the push sequences and then generates the shear waves. Verasonics is compatible with many transducers and offers significant flexibility in sequence design. Additionally, Verasonics

provides direct access to the raw channel data from each element of the array, as well as a software beamformer to form ultrasound images [213]. In Figure 4.13, one can see the Vantage Verasonics system during measurements and the Verasonics $L11-5v$ transducer used in this work is shown.

Verasonics vantage 128 (actualised to 256) system was used to perform the SWEI. The system uses the MATLAB programming environment to create the protocol of measurements of SWEI. The sequence of steps is as follows: the programmer writes a programming script to generate an imaging sequence, which generates a collection of objects that are loaded into the Verasonics scanner during runtime. The main parameters for the script are: (1) the push and track transmit frequencies; (2) the push duration; (3) the push and track transmit aperture; (4) the sampling frequencies; and (5) the pulse repetition interval. Details and sequences of the Verasonics script can be found in the work of Deng et al. [213].

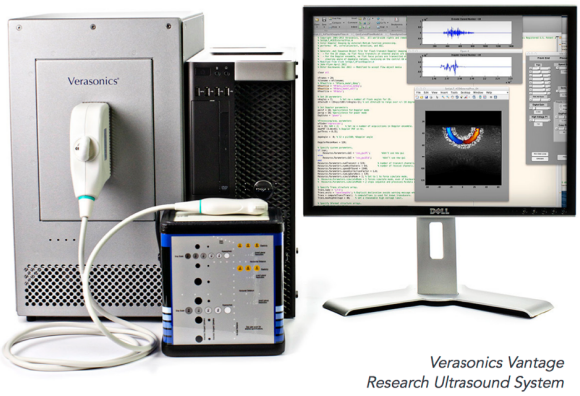

Figure 3.7: Verasonics Vantage research ultrasound system

Changes in the voltage applied for the push will make the induced push less or more powerful creating shear waves of different amplitudes. The voltage applied was stepwise increased and a value of 40 V was chosen for the ex vivo chicken liver and cervical tissue and 28 V for the hydrogel phantoms.

The measured shear wave velocity (SWV) can be used to determine tissue properties assuming a mechanical model of the tissue. For a linear, elastic, isotropic, homogeneous, and unbounded material, the SWV can be expressed in terms of the shear moduli μ and density ρ by the relation

$$SWV = \sqrt{\mu/\rho} \tag{3.6.1}$$

The density of soft tissue is typically assumed to be 1000 kg/m^3 and the SWV in units of m/s is equal to the square root of the shear moduli when it is expressed in units of kilopascals. In contrast, for a viscoelastic material, the shear moduli is a complex frequency-dependent quantity. Shear wave propagation in a viscoelastic material exhibits dispersion with a frequency-dependent phase velocity and shear attenuation [212].

The shear wave velocity dispersion curve was extracted from the ARFI using a phase difference method. First, the tissue velocity field was smoothed. This operation does not modify the phase velocity, only the amplitude, and the initial phase. The propagation of the plane wave in the sample along the x-direction is described by a 2D velocity field *v(x,t)*. The phase $\phi(x, \omega)$ of the wave at each frequency was obtained using a Fourier Transform of the tissue velocity field *v(x,t)*. For a monochromatic plane wave propagating in the direction x, the phase can be written as:

$$\phi(x, \omega) = -Re[k(\omega)]x \tag{3.6.2}$$

where $k(\omega)$ is the complex wavenumber and ω is the frequency. Thus, the shear wave phase velocity is:

$$c_s = \frac{\omega}{-Re[k(\omega)]} \tag{3.6.3}$$

and the real part $Re[k(\omega)]$ of the wave number can be estimated from a linear fit of the phase $\phi(x, \omega)$ along the propagation distance x [214, 215, 216].

Finally, dispersion curves are plots of shear wave velocity (SWV) as a function of angular frequency for ex vivo soft tissue.

Verasonics SWEI sequencing and data processing: Tissue motion estimation

Tissue motion was determined using a phase-shift algorithm that operates on IQ data (in-phase and quadrature data). In this study, Loupas 2D autocorrector algorithm was used to estimate the axial displacement caused by the propagation of the shear waves. The Loupas algorithm is an extension of the Kasai algorithm, which is used to post-process Verasonics data. It has the advantage of generating more accurate displacement estimations because it takes into account the center frequency [213, 217]. Figure 3.8 shows a flow chart of how Verasonics generates SWEI and the steps needed to obtain the IQ data from an ARFI sequence. In this work, post-processing of the IQ

data to obtain a displacement map was done using the Ultrasound Toolbox (USTB) [218].

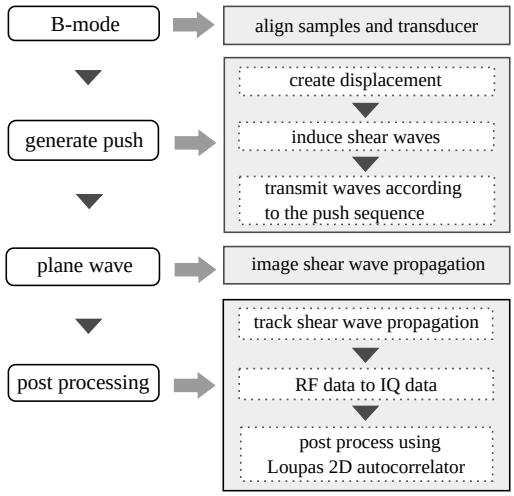

Figure 3.8: Procedure for tissue motion estimation using Shear Wave Elastography Imaging(SWEI) technique. Adapted from[3].

3.6.2.Via mechanical tests

All the mechanical tests were performed using the tensile-compression press shown in Figure 3.9. The device was equipped with a 500 N force gauge (IMADA ZTA-500N) fixed to a platform that is operated by three motors with an accuracy of 0.3μm. The tolerance of the force gauge is 0.1 N. The cervical tissue was fixed by two Acrylonitrile Butadiene Styrene (ABS) printed gripper jaws, one was attached to the press and another linked to a fixed support, that prevents the cervical tissue from undesired movements. According to the literature reviewed in soft tissue uniaxial tensile tests, the load step was 0.2 mm, and the strain ramp rate used was $1\%/s$ [219]. A rule was used in the same plane in which the sample was contained for the calculation of deformations. Finally, a conventional camera (IPEVO Ziggi-HD High Definition USB CDVU-04IP model, 5 Mpix, 1280 $\times$ 720 resolution) was employed to acquire the image sequence at each loading step until the sample breakdown (Figure3.10). The camera was synchronized with a MATLAB®programming environment (Release 2018b, MathWorks, Natick, MA , USA) at the beginning of the experimental test. The code implemented in MATLAB®allowed controlling each increment of load through an Arduino micro-controller, at the same time that recorded at a rate of 1 frame per

load increment until the sample breakdown.

For cornea

Uniaxial tensile tests were conducted to obtain the elasticity of (1) porcine corneas in the five studied groups. The device used was designed and calibrated in the 'Ultrasonics Lab' of the University of Granada (Spain). It comprised two clamps, one that was firmly anchored to the base and another that could move in the vertical direction driven by three synchronized motors. The clamps were printed in ABS (acrylonitrile butadiene styrene) with specific surface roughness to avoid sample slippage. The upper clamp was attached to a digital force gauge (ZTS-50N, Imada Co., Ltd) whose maximum capacity was 50 N, with a resolution of 0.01 N. A high resolution camera with a 4:3 ratio and 2560x1920 resolution (IPEVO Ziggi-HD 5MPix) was synchronized with the displacement of the upper clamp. The monitoring of tissue deformation and the loading steps were controlled by a Matlab routine. All the samples were cut into vertical strips with the most unfavourable part being the central cross-section of the sample. The width of the NaOH-treated samples was reduced to avoid saturation of the force gauge. The dimensions of the samples were measured using an electronic caliper (Table 1). The samples were preconditioned with 10 loading cycles at 1 N to resemble a mechanical state close to in vivo IOP conditions. The tissues underwent a quasi-static uniaxial tensile displacement to the rupture point at a rate of 0.2 mm/s. Acrylic black paint was sprayed over the sample for speckle generation in the samples to improve deformation monitoring. The corneal samples were kept continuously hydrated so as to prevent a severe alteration of the mechanical properties during the experiment by spraying them with PBS.

Although the stress-strain curve had a nonlinear behaviour for the studied deformations, the curve was analyzed in two linear regions [39], where linear elasticity, homogeneity and isotropy were assumed, and viscosity ignored, which allowed to compare the trends with the values obtained with TWE. In the first region (toe region), the mechanical response was believed to be dominated by non-collagen components of the stroma, since the collagen fibrils were initially crimped and then were progressively uncoiling as the load increased. In the second region, collagen fibrils were sufficiently elongated to control the mechanical response (Figure 5). The stress-strain curve was obtained by dividing the force measured in each increment of displacement by the initial section in the most unfavourable area, and the deformation by dividing the displacement by the initial length between clamps. This initial length was set when the sample was stretched under a load of 0.01

N. The thickness of the samples was considered constant throughout the test. For the calculation of the elasticity in the first region, a linear range of deformation 0.02-0.04% was considered. For the calculation of the elasticity in the second region (mechanical response governed the collagen fibrils), a searching algorithm was implemented to detect the region of the curve in which the minimal variation of the slope was found between successive points.

For uterine cervix

The sample preparation protocol consists of several steps:

1. All the seven cervical tissues were excised from the women and placed in phosphate buffered saline (PBS) to avoid loss of hydration after surgery. The connective layer was cut below the epithelial layer, and at a sufficient distance from the cervical canal to ensure that the preferred direction of the collagen fibres corresponds to the direction of the uniaxial tensile test [176, 220]. The samples were tested in the Ultrasonics Laboratory at the University of Granada. Two slices were cut manually from each cervical sample, one from the epithelial layer and another one from the connective layer. The epithelial layer was cut carefully to obtain a thickness between 0.5 and 1 mm. The connective layer was obtained below the epithelial layer. All the samples were cut with the same mould (see Figure 3.11) to maintain the same geometry, which is necessary to locate the most unfavourable section.

2. A random dot pattern was used in the cervix to improve deformation monitoring carried out by a cross-correlation algorithm (PTVlab software). For the speckle generation, acrylic black paint was used.

3. An optimal contrast obtained by a good illumination and a uniform background help the tracking algorithm.

4. It is worth underlining that the cervical tissue samples were kept continuously hydrated so as not to alter the mechanical properties during the experiment by spraying them with PBS.

5. All the samples were preconditioned with 10 cycles at 1 N before the uniaxial tensile test.

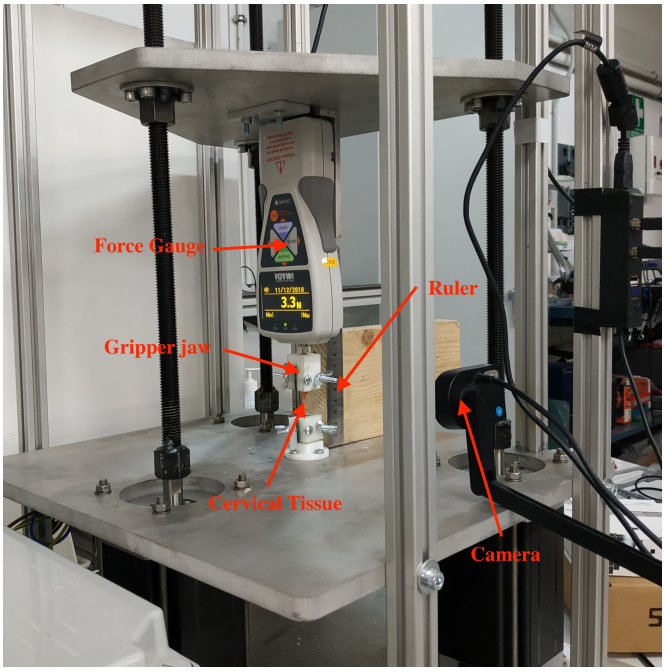

Figure 3.9: Experimental set-up comprising a 500 N force gauge, gripper jaws for holding the sample attached and a conventional camera to register the loading process. Adapted from[2].

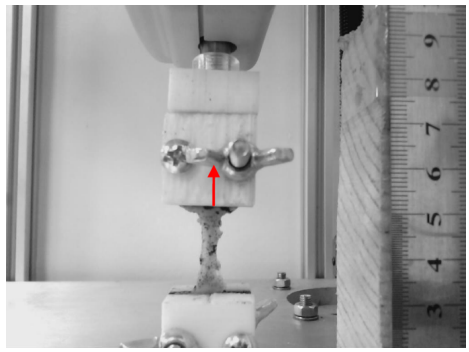

(a) Load = 2.8 N

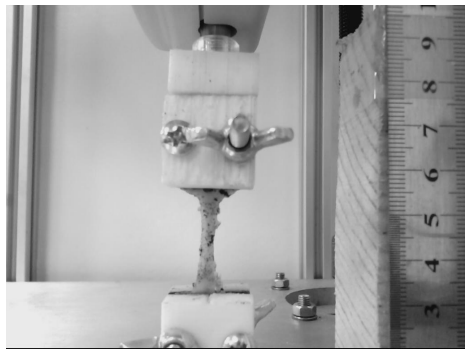

(b) Load = 10.7 N

(c) Load = 0.3 N

Figure 3.10: Three different frames from a recording of a uniaxial tensile test in a cervical tissue sample. The tissue is stretched in the direction marked with a red arrow. Adapted from[2].

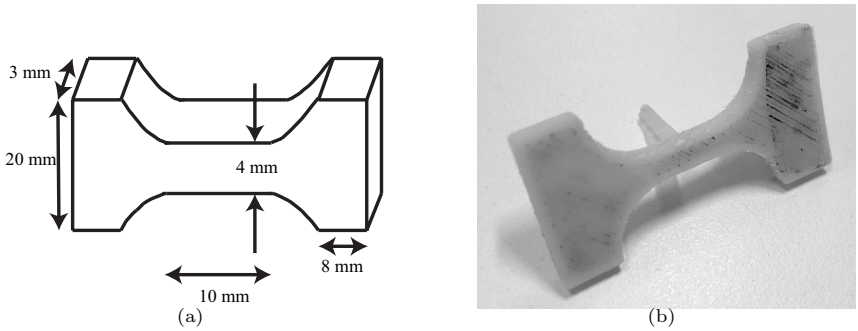

Figure 3.11: (**a**) Mold printed with Acrylonitrile Butadiene Styrene (ABS) to maintain the geometry of the samples. (**b**) Cervical tissue sample geometry. Adapted from[2].

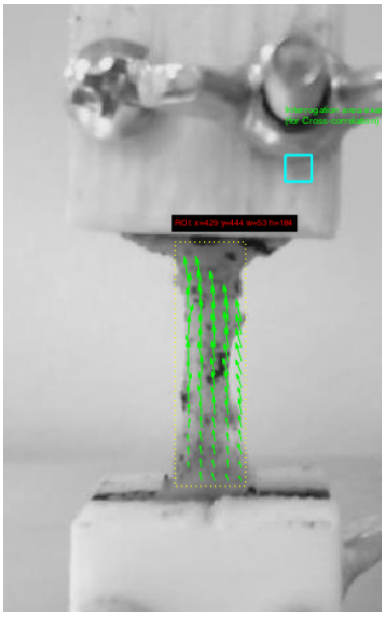

Figure 3.12: An illustrative example of cervical tissue attached to two gripper jaws that fix it during the uniaxial tensile test. A dashed yellow line was used to delimit the region of interest (ROI). The green arrows represent the displacements. Adapted from[2].

PTVlab is free software that was developed by Dr. Wernher Bre vis (mainly

developed the mathematical algorithms) and Antoine Patalano (an adaptation of the graphical user interface (GUI) in MATLAB and the development of new functionalities) [221, 222]. The Large Scale Particle Tracking Velocimetry (LSPTV) method is employed by PTVlab and uses the binary correlation, the Gaussian mask and the dynamic threshold binarization techniques for the particle detection. A Gaussian mask with a correlation threshold 0.5 and a sigma of 3 px was used for particle tracking. The Particle Tracking Velocimetry (PTV) algorithm was cross-correlated by an interrogation area of 10 px, a minimum correlation of 0.6 px, and a similarity neighbour of 25%. The deformations were calculated in the most unfavourable area of the cervical tissue, which according to the printed mold corresponds to the central area.

Part III

EXPERIMENTAL RESULTS

"Have no fear of perfection; you'll never reach it."

Marie Curie

Chapter4

Quantification of ex vivo tissue viscoelasticity using isotropic TWE

When determining tissue viscoelasticity it is important to note that if tissues are precompressed when they are examined, the estimation of parameters will be biased, as the time-dependency of the response is relevant. Changes over time due to mechanical stimulation are attributed to rapid alterations in cellular activity, mainly the synthesis and modification of components of the ECM (collagen and proteinases) [132]. To avoid this situation, preconditioning protocols should be proposed whenever the specimen studied allows it, so that a stabilization in the response is achieved [133]. With the aim of capturing this material behaviour, the most popular approach considers soft tissues as uniphase solids and its response to external loads or deformation is represented as a lumped relationship. This method uses linear viscoelastic models that generally include a solid-related characteristic (e.g., spring) and a viscous fluid element (e.g., dashpot). To name a few, Maxwell, Kelvin-Voigt (KV) and Zener viscoelastic models provide information on how the different scales are linked to each other [134, 135]. However, in order to fit a model when the soft tissue shows several characteristic times, generalized linear viscoelastic models are used, such as generalized Maxwell or KV models [136, 137]. When large strains are expected, these linear models are not suitable, thus it is frequently adopted the proposed Fung's quasilinear viscoelastic model [138].

One of the most used models in the literature to fit the parameters is the KV model due to its simplicity [139]. Other models have been explored, such as Maxwell, fractional derivative versions of the above, or combined models such as the springpot model [140]. The KV formulation in terms of the stress tensor, assuming constitutive and viscous linearity have been derived with the aim of simplifying equations [141]. Following the references found in the literature [142, 143, 144].

All this evidence suggests that the viscous phase may become a biomarker for the characterization of microstructural changes [145, 146, 147, 148, 149]. The method of shear wave speed dispersion curve used in this thesis: estimation of vicosity parameters by fitting a rheological model is the most relevant and extended technique since there is considerable amount of previous work for different types of organs to compare with. But it has the disadvantage that there is no consensus on the most appropriate rheological model for soft tissue characterization
Studies report values of viscosity for a specific rheological model (not comparable).

4.1.Ex vivo chicken liver

Two techniques were used to obtain mechanical elastic and viscoelastic biomarkers. The first, developed by our group, was TWE, and the other technique used a commercially available system for shear wave generation, a Verasonics Vantage system. The elasticity measurements using 2D SWEI and TWE may be expressed as either shear wave velocity (m/s) or shear moduli (kPa). The procedure for the samples scan is shown in Figure 4.1. Basically, it consists of preparing the samples (ex vivo liver and hydrogel phantoms) for testing; measuring them by generating torsional and shear waves; capturing the propagation of these waves; and, finally analyzing the signal to reconstruct the biomechanical markers.

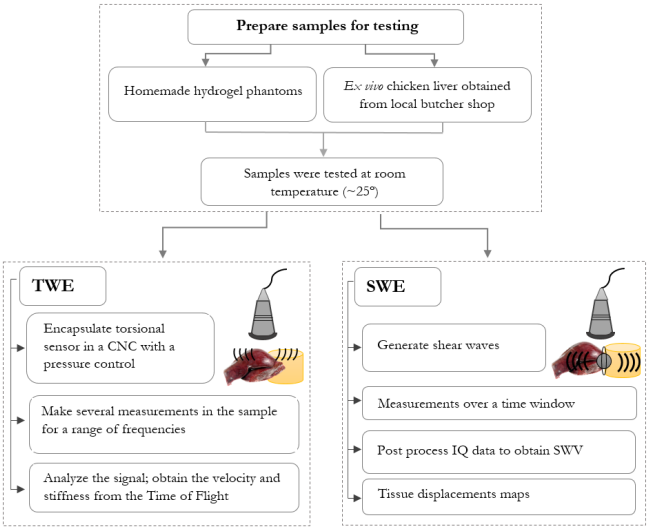

Figure 4.1: Flow chart showing the steps for scans performed with both techniques, Torsional Wave Elastography (TWE) and Shear Wave Elastography Imaging (SWEI). Adapted from[3]

4.1.1.Sample preparation

To assess the properties and feasibility of SWEI in a safe and repeatable manner, it is necessary to use phantoms with ultrasonic properties mimicking those of soft tissue, eliminating real tissue heterogeneity, anisotropy, and variability; thus, hydrogel phantoms were prepared. Three fresh ex vivo samples of chicken liver were also tested for testing real scenarios. To perform ultrasound stiffness imaging, ex vivo samples were kept at room temperature at 25° before testings. Each sample was scanned three times in two different regions.

To compare and determine the effect of the viscosity, two homemade homogeneous phantoms were prepared. Both were made from porcine gelatin powder at 7.5% gelatin concentration (Fisher Chemical, Leicestershire, UK) and 0.5% of sodium dodecyl sulfate (Sigma-Aldrich Corp., St. Louis, MO, USA). To capture the shear wave, we used enhancements for the ultrasound imaging 1% of castor oil in one phantom and 0.5% graphite particles in the second one. The manufacturing process of the phantoms followed the standard used in the literature and particularly the methodology proposed by Park et al. [223] and Dunmire et al. [224]. Figure 4.2 shows ex vivo liver samples used for this work, the ingredients for phantom manufacturing, and

one of the hydrogel phantoms being scanned.

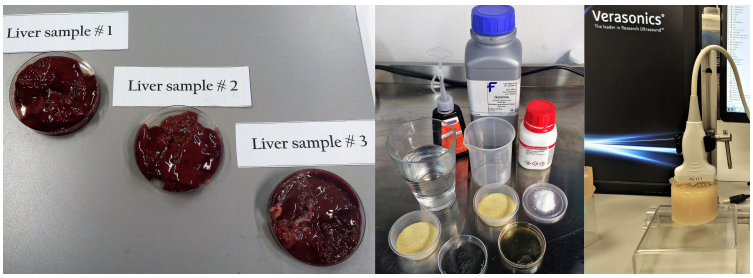

Figure 4.2: Three ex vivo liver samples, phantom ingredients, and one of the phantoms subjected to shear wave elastography imaging. Adapted from[3]

4.1.2.Experimental set-up

Figure 4.3 shows the TWE probe developed by our group. The left sub-figure shows the sensor encapsulated in a CNC (computer numerical control) system (designed and fabricated in the Ultrasonics Lab) that allows measuring within an exact position and at the same time exerting a controlled pressure on the sample. The right sub-figure shows a cross-section of the isotropic TWE probe. More details of the probe can be found in the work of Callejas et al. [134].

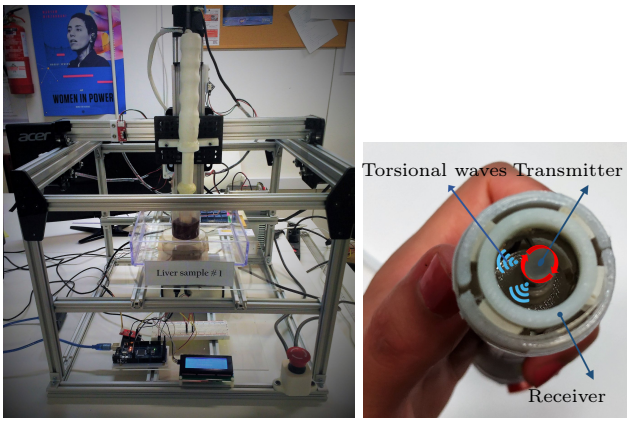

Figure 4.3: Set-up for measurements using TWE technique. The picture was taken during the measurements at the Ultrasonics Lab at the University of Granada. The figure on the left is a computer numerical control (CNC) system for positioning and pressure-control of the TWE probe. The right figure shows a cross-section of the TWE probe. Adapted from[3].

Acquisition parameters for TWE technique used for both ex vivo liver samples and tissue-mimicking hydrogel are shown in Table 4.1.

Table 4.1
Torsional wave elastography (TWE) technique acquisition parameters for both ex vivo liver samples and hydrogel phantoms.

Measurements Acquisition Parameters	**Value**
Sampling frequency	80 Hz (Decimated 10× after 800 Hz)
Ring-disc radius	3 mm
Frequency	200–800 Hz
Averaging	10 ×
Excitation power	20 V

Comparisons and validation of the results obtained via TWE were done against SWEI using a verasonics vantage 128 system. In Figure 4.13, one can see the Vantage Verasonics system during measurements and the Verasonics $L11-5v$ transducer used in this set of measurements is shown.

Figure 4.4: Set-up for measurements using SWEI. The picture was taken during the measurements at the Ultrasonics Lab at the University of Granada. In the left image, the ex vivo liver sample is measured while one of the hydrogel phantoms is shown in the right image. Adapted from[3]

Properties of the $L11-5v$ 128 elements linear array transducer are shown in Table 4.2.

Table 4.2
Properties of the $L11-5v$ Verasonics transducer.

Property	**Value**
Number of Elements	128
Pitch (mm)	0.3
Elevation focus (mm)	18
Sensitivity (dB)	-52 ± 3

Table 4.3 lists the SWEI acquisition parameters used in this study. The push transmit frequency was set to the center of the transducer to allow maximum transmission efficiency to transfer the ARFI to the tissue. An identical set can be used for the tracking frequency. However, it is recommended to use a lower push frequency to widen the push beam width compared with the track beam width to reduce the underestimation of tracked tissue displacement [225, 226] so a lower frequency was used.

Table 4.3
SWEI acquisition parameters for $L11-5v$ Verasonics transducer.

Parameter	**Value for the $L11-5v$ Transducer**
Push frequency (MHz)	4.8
Track frequency (MHz)	7.81
Push duration (cycles)	1000
Pulse repetition interval (μs)	100
Impulse duration (cycles/(μs))	1000, 128
Impulse focus (mm)	16 for ex vivo liver and 12 for hydrogel phantoms
Beam focus configuration	Plane wave, fully open
IQ data beam forming sampling frequency	0.25λ
Excitation voltage (V)	40 for ex vivo liver and 28 for hydrogel phantoms
Sampling frequency(Hz)	3000
Number of transmission channels	128
Number of reception channels	128

Changes in the voltage applied for the push will make the induced push less or more powerful creating shear waves of different amplitudes. The voltage applied was stepwise increased and a value of 40 V was chosen for the ex vivo chicken liver and 28 V for the hydrogel phantoms.

4.1.3.Results

The results of the scans are presented as mechanical biomarkers in terms of shear wave velocity, shear moduli, and viscosity. A comparison of shear wave velocity as a function of frequency for both TWE and SWEI techniques can be found in Figure 4.5. The sub-figure on the top is for fresh ex vivo liver samples and the one on the bottom is for hydrogel phantoms. Measurements were done within the frequency range of 200–800 Hz. Solid lines are optimal fits of a Kelvin–Voigt rheological model.

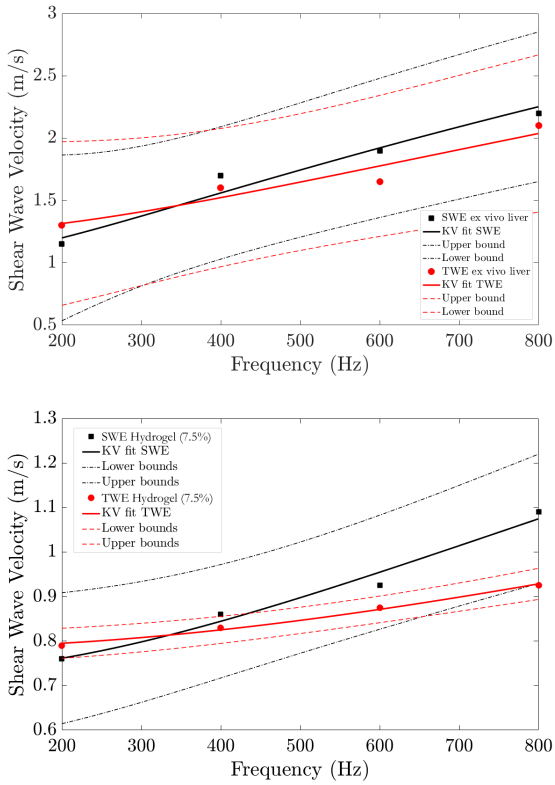

Figure 4.5: Dispersion curve for the two types of samples measured, square/circle marks are the values of shear wave velocity versus frequency via shear wave elastography imaging (SWEI) and torsional wave elastography (TWE) for ex vivo chicken liver samples (**top**) and hydrogel phantoms (**bottom**). Kelvin–Voigt (KV) fit is shown with solid lines in black color for SWEI and in red for TWE, and 95% confidence intervals are displayed with dashed lines. Adapted from[3].

The results show shear wave velocities go from 1.15 to 2.25 m/s for SWEI and from 1.3 to 2.03 m/s for TWE as mean values for the three liver samples. In the case of hydrogel phantoms, SWV values vary from 0.76 to 1.09 m/s for SWEI and from 0.79 to 0.93 m/s when scans were done via TWE. Both techniques show the same trend. These values are mean velocities for the two types of samples. ARFI based measurements were done three times in different liver areas. The results show a clear viscous trend in the samples. The results are in concordance with those presented in the literature [227,

228, 229].

A Pearson correlation coefficient was calculated to observe the degree of agreement between the reconstructed shear wave velocities obtained from both techniques, TWE and SWEI. The results are shown in Figure 4.6. A significant degree of agreement is observed, with a Pearson correlation coefficient of 0.99767 for liver samples and 0.99838 for hydrogel phantoms.

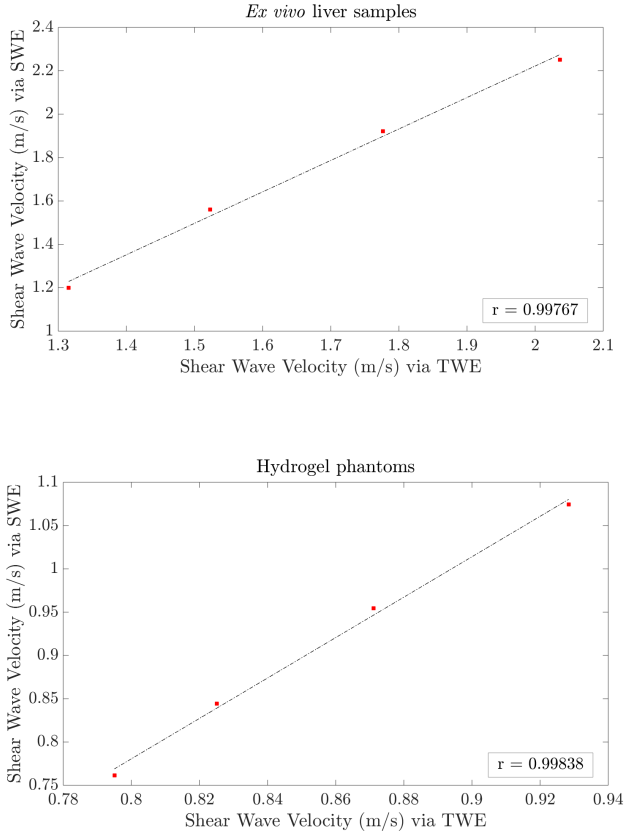

Figure 4.6: Pearson's correlation between shear wave velocities via SWEI and TWE for both ex vivo liver samples (**top**) and hydrogel phantoms (**bottom**) at a frequency range from 200 to 800 Hz. Pearson correlation coefficients are 0.99767 for liver samples and 0.99838 for hydrogel phantoms. Adapted from[3].

Biomechanical elastic parameters obtained via TWE and SWEI in terms of shear moduli, μ, for both ex vivo chicken liver samples and hydrogel

phantoms are tabulated in Table 4.4. Scans were made under a range of frequency from 200 to 800 Hz. Measurements were done in this range of frequencies based on the power spectrum obtained from the shear wave tracked by the Verasonics transducer for liver samples, as shown in Figure 4.7. It can be observed that the energy concentration is within this range of frequencies (200–800 Hz); frequencies above this range are considered noise.

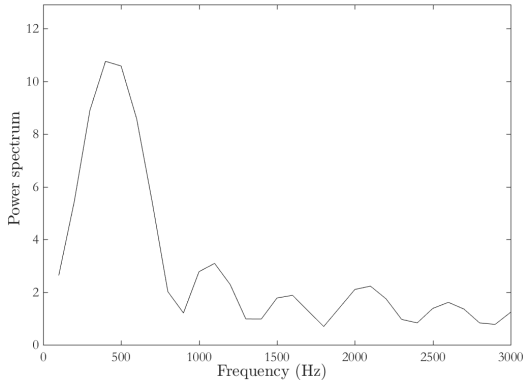

Figure 4.7: The power spectrum of the shear wave tracked by the 7.8 Mhz ($L11-5v$) transducer for the ex vivo liver sample using a Verasonics vantage system. Adapted from[3].

Next, viscosity parameters for the same samples using two different rheological adjustments, namely Kelvin–Voigt and Maxwell, were determined (see Table 4.5). The results show the same trend; shear moduli are frequency dependent and increases with increasing frequency.

Verasonics Vantage systems measure and report shear wave velocity; therefore, to obtain the mechanical biomarkers in kPa, SWV values were transformed by Equation (3.6.1) to get shear moduli μ. In this study, it was assumed that tissue density is 1000 kg/m^3.

Table 4.4
Shear moduli in kPa for both ex vivo liver samples and hydrogel phantoms obtained from torsional wave elastography (TWE) and shear wave elastography imaging (SWEI) techniques.

	Elastic Parameter: Shear Moduli in kPa			
	Ex Vivo Liver Samples		**Hydrogel Phantoms**	
Frequency (Hz)	μ_{TWE}	μ_{SWEI}	μ_{TWE}	μ_{SWEI}
200	1.69 ± 0.78	1.32	0.62 ± 0.04	0.58
400	2.66 ± 0.23	2.82	0.68 ± 0.05	0.74
600	2.69 ± 0.47	3.69	0.78 ± 0.065	0.85
800	4.00 ± 0.42	4.84	0.86 ± 0.055	1.16

Figure 4.8 shows particle displacement versus time profiles at 24 lateral positions for both an ex vivo liver sample and a hydrogel phantom.

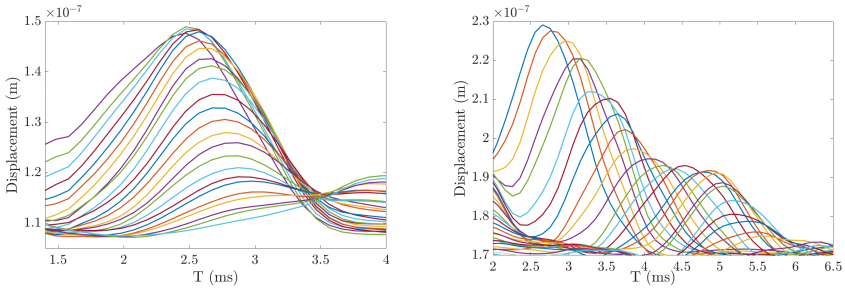

Figure 4.8: Experimental particle displacement versus time profiles at the focal depth resulting from the ARFI excitation. The ARFI moves the tissue in the axial and lateral position. In this figure, each displacement trace indicates a lateral position starting nearby the ARFI push focus to 24 lateral positions. Each individual color curve indicates the lateral position of a displacement trace for ex vivo liver sample II (**left**) and hydrogel phantom II (**right**). The curves show that, at farther distances (few milliseconds after the push), the particle displacement is reduced, since the shear wave dissipates. Adapted from[3].

Table 4.5
Viscoelastic parameters for ex vivo liver samples and hydrogel phantoms obtained from torsional wave elastography (TWE) and shear wave elastography imaging (SWEI) techniques.

Sample	**Fit**	**Viscous Parameters**				**The Goodness of Fit R-square**	
		TWE		**SWEI**		**TWE**	**SWEI**
Ex vivo liver	Kelvin–Voigt (KV)	$\mu = 1.512$ kPa	$\eta = 0.536$ Pa·s	$\mu = 1.019$ kPa	$\eta = 0.628$ Pa·s	0.9198	0.9572
	Maxwell (M)	$\mu_1 = 5.773$ kPa	$\mu_2 = 4.316$ Pa·s	$\mu_1 = 13.720$ kPa	$\mu_2 = 3.712$ Pa·s	0.835	0.9861
Hydrogel phantom	Kelvin–Voigt (KV)	$\mu = 0.615$ kPa	$\eta = 0.093$ Pa·s	$\mu = 0.532$ kPa	$\eta = 0.148$ Pa·s	0.9926	0.9764
	Maxwell (M)	$\mu_1 = 0.827$ kPa	$\mu_2 = 2.897$ Pa·s	$\mu_1 = 1.267$ kPa	$\mu_2 = 1.663$ Pa·s	0.7879	0.8237

The axial displacement map obtained using the Loupas algorithm [217, 218] after post-processing the IQ (in-phase and quadrature data) of ex vivo liver sample I is shown in Figure 4.9. We can see the ARFI push and the shear wave propagation. The y-axis represents the depth in mm of the scan, and the x-axis the lateral distance of the wave propagation. The sequence of the figure (from A to D) shows the localization of the ARF push and the shear wave lateral propagation away from the focus. Loupas $2D$ autocorrelator performs as the gold standard phase domain technique for motion estimation[230, 231].

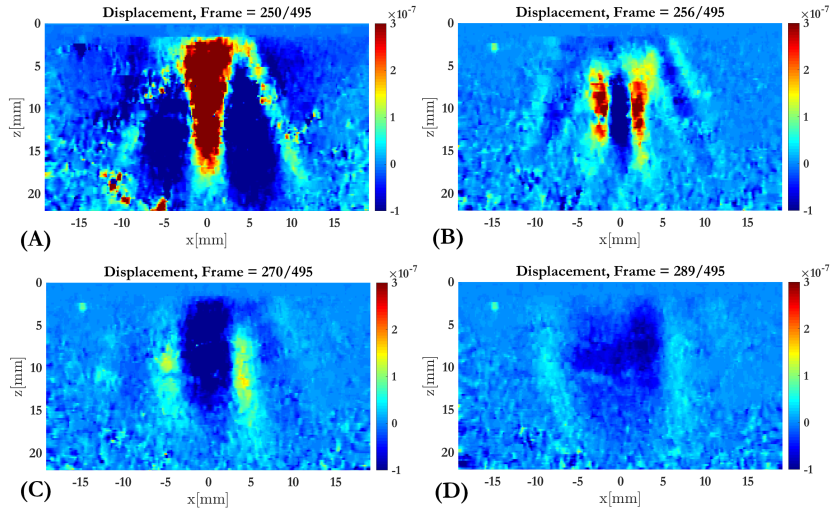

Figure 4.9: A sequence of displacement map (displacements are in meters) of ex vivo liver sample I due to ARFI excitation. The box represents the ROI (Region of Interest) chosen. The sequence from A to D show the push start (sub-figure A) and the shear wave propagation in different frames (sub-figures A-D) till its dissipation. Adapted from[3].

4.1.4.Conclusions

In this chapter, SWEI was used to validate TWE, since it is the gold standard and one of the most important noninvasive techniques in quantifying the viscoelastic parameters [232, 233]. A significant number of studies reinforce this decision; for instance, Kyoung et al. [234] showed that SWE is a good method to evaluate the usefulness of the stability index (SI) in liver stiffness measurements, demonstrating that this reduces the variability and increases the reliability in both free-breathing and breath-holding conditions. Samir et al. [235] estimated liver stiffness using SWE. The res-

ults obtained from the right upper lobe gave the best correlation with liver fibrosis severity and can potentially be used as a noninvasive test to differentiate intermediate degrees of liver fibrosis in patients with liver disease.

A validation study of five elastography techniques available commercially using individual tissue-mimicking liver fibrosis phantoms with different known Young's moduli was performed by Mulabecirovic et al. [236]. They concluded that the SWE systems have very good repeatability and interobserver agreement. Dietrich et al. [237] presented guidelines and recommendations on the clinical use of liver ultrasound elastography; in their work, they firmly recommend comparison studies of all the technologies available to improve our knowledge on cut-off values for each system. Another comparison among commercially available techniques using SWE for the assessment of chronic liver diseases was presented by Friedrich-Rust et al. [238].

The reproducibility of the TWE technique was evaluated and found consistent with previous studies. The first validation of TWE was made by Callejas et al. [134] using a classical rheometer (limited to 50 Hz), which is a quasi-static regime; the limitation of the previous work is that the measurements to obtain the shear moduli were made at frequencies well below the measurements made by TWE (300 Hz to 2 kHz). Therefore, in this work presented herein, the Verasonics Vantage system was used as the source to generate shear waves, allowing a comparison between the two methods in the same frequency range. The results are shown in Figure 4.5. The dispersion curves for the two types of samples measured, ex vivo liver samples and two tissue mimicking hydrogel phantoms, show the viscous response of the tissue. Each sample was measured several times by both techniques in different positions and under different pressures. Biological variability in the samples cannot be neglected; indeed, we observed different zones of rigidity in the same sample, which is true for all samples. Significant variability was found when different zones of the same sample were scanned by the same technique.

The values of shear wave velocities, from 1.15 to 2.25 m/s for SWEI and from 1.3 to 2.03 m/s for TWE as mean values for the three liver samples, agree with other results obtained from the literature [227, 228, 229]. However, the same figure shows that the curves representing TWE and SWEI results are spaced at high frequencies (>800 Hz). This is probably because the attenuation is too high and the signal is dissipated. A similar observation was obtained from the hydrogel phantoms results. Pearson correlation coefficient shows good agreement between shear wave velocity (SWV) via TWE and SWEI, with values of 0.99767 for liver samples and 0.99838 for hydrogel

phantoms, as reported in Figure 4.6.

Elastic biomarkers in terms of shear moduli in kPa under the frequency range of 200 to 800 Hz show a good match between the techniques and report a similar tendency as SWV and therefore shear moduli are frequency dependent; increasing the frequency increases shear moduli values (Table 4.4).

One of the advantages of elasticity based images is that many soft tissues may share a similar capacity to reflect ultrasonic waves, but they may have different mechanical properties that can be used to visualize normal anatomy and trace pathological lesions more clearly. The liver is a viscoelastic structure, which is why changes in its viscosity would be closely related to liver diseases. Several authors suggest that changes in the transmission rate of mechanical vibration depend on the frequency [239, 240, 241]. Hence, SWE has some advantages over Transient Elastography (TE) [242, 243]. Since Shear wave velocity is frequency dependent, it is possible to quantify the tissue viscosity from the shear wave dispersion curves [244, 245, 144, 246]. In this study, viscoelastic biomarkers were obtained by fitting the model to the measured frequency. The results, as listed in Table 4.5, present significant differences between the two rheological models proposed, Kelvin–Voigt (KV) and Maxwell. The goodness of the adjustment shows that, in this case, KV model characterizes better both tissue samples and hydrogel phantoms. This opens up the debate to the elastography scientific community to present guidelines on which rheological model can express in the most concise way the characterization of soft tissue. Hydrogel phantoms show slightly better results than ex vivo liver samples, possibly for being more homogenous. Table 4.5 shows the parameters related to all the frequencies in the range of 200–800 Hz, where the maximum energy is concentrated, and not all the frequencies shown in Figure 4.7. Frequencies above 800 Hz are assumed to be noise.

4.2.Ex vivo human uterine cervix

A total of eight hysterectomy specimens from women with benign gynecological conditions were obtained from Health Campus Hospital in Granada Table7.1). The study met the principles of the Declaration of Helsinki. Approvals of the Ethical Committee in Human Research of the University of Granada and Ethical Commission and Health Research of Health Campus Hospital in Granada were achieved. All women enrolled in the evaluation provided agreement by signing a written consent and reading the information of the patient report.

Table 4.6
Obstetric characteristics of the population in the study.

Patient	Age	Hysterectomy Indication
1	53	Vaginal prolapse
2	67	Subserous myoma
3	59	Vaginal prolapse
4	54	Cervical prolapse
5	50	Cervical prolapse
6	51	Cervical prolapse
7	71	Cervical prolapse
8	66	Cervical prolapse

4.2.1.Sample preparation

The cervical tissue samples were collected one by one in different weeks. Then, they were handled from the operating room and measured fresh at room temperature on the same day. When they were excised from the women, the uterine cervical specimens were placed in phosphate-buffered saline (PBS) to avoid loss of hydration after surgery.

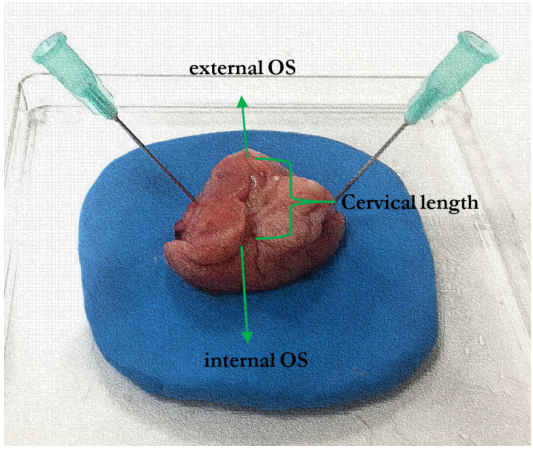

Figure 4.10: Cervical tissue sample obtained from hysterectomy

4.2.2.Experimental set-up

As in the previous section, the samples have been measured by TWE and SWEI following the flowchart in Figure**??**, the latter technique was used to validate the torsional measurements.

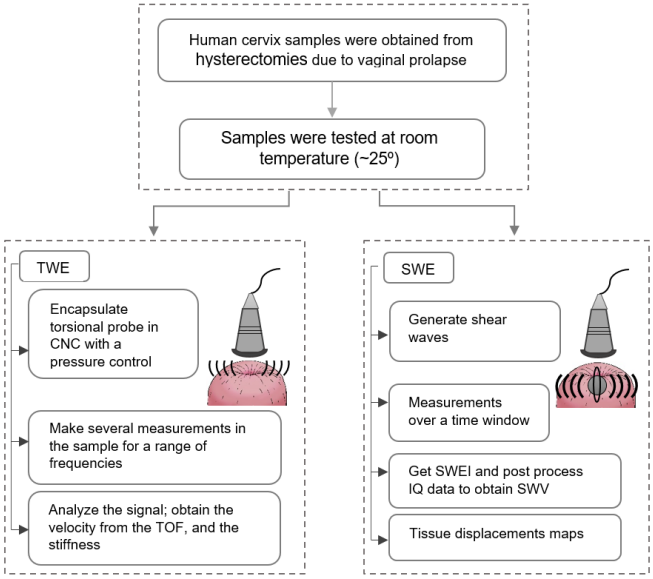

Figure 4.11: Steps for ex vivo samples scanning via TWE and SWEI.

In the TWE set-up, the cervical tissue was positioned under the torsional probe, and the sensor was encapsulated in a CNC (computer numerical control)6.9 system to control the position and pressure exerted by the operator when measuring. The samples were measured by varying the pressure from 25gr to 150gr and in different regions. An average of three measurements was made in each area. A frequency sweep from 400 to 1400hz was used in all the experiments. Acquisition parameters for the TWE are the same shown in Table4.1

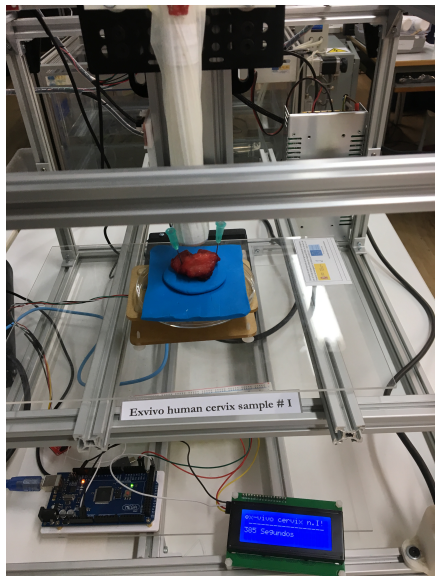

Figure 4.12: Set-up for TWE of human uterine cervix, showing the torsional wave probe encapsulated in a CNC system for pressure control.

Verasonics vantage 128 system was used for validation of the results obtained via TWE. Figure 4.13, one can see the Vantage Verasonics system set-up during measurements, Verasonics $L11-5v$ transducer was used.

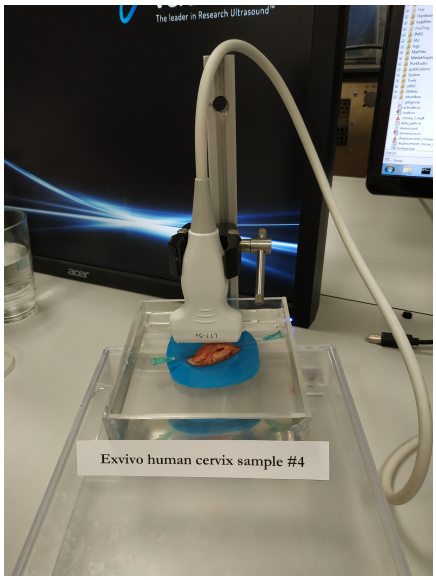

Figure 4.13: Set-up for measurements using SWEI. The picture was taken during the measurements at the Ultrasonics Lab at the University of Granada.

Properties of the $L11-5v$ 128 elements linear array transducer are shown in Table 4.2. Table 4.3 lists the SWEI acquisition parameters used in this study. The push transmit frequency was set to the center of the transducer to allow maximum transmission efficiency to transfer the ARFI to the tissue. In this case, an identical set was used for the tracking frequency.

4.2.3. Results

The results of the scans are presented as mechanical biomarkers in terms of shear wave velocity, shear moduli, and viscosity. Figure4.14 shows the stiffness values in (kPa) of the 8 uterine samples at different locations; anterior and posterior OS. This figure shows the viscosity trend of the cervical tissue.

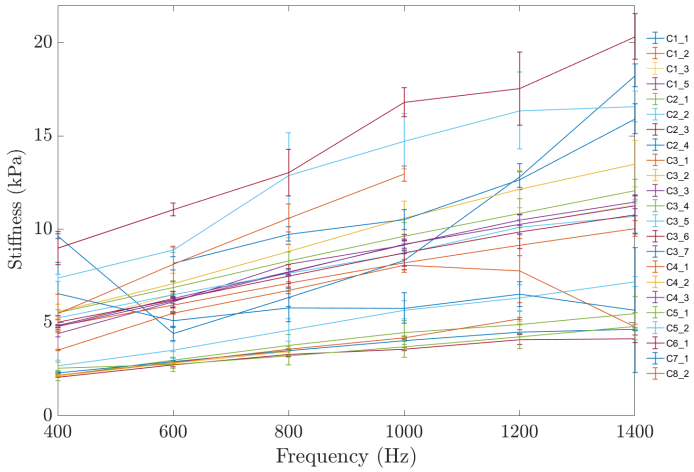

Figure 4.14: Stiffness values obtained from measuring via TWE the eight ex vivo human uterine cervix samples. Each sample was measured several times at different locations.

A comparison of shear wave velocity as a function of frequency for both TWE and SWEI techniques can be found in Figure 4.15. Similar trend and concordance in group velocities are obtained from both techniques.

Next, viscosity parameters for the same samples were determined using two different rheological adjustments, Kelvin-Voigt, Maxwell, Zener and a Fractional Kelvin-Voigt (see Table 4.7 4.8). The results show the same trend; shear moduli are frequency dependent and increases with increasing frequency.

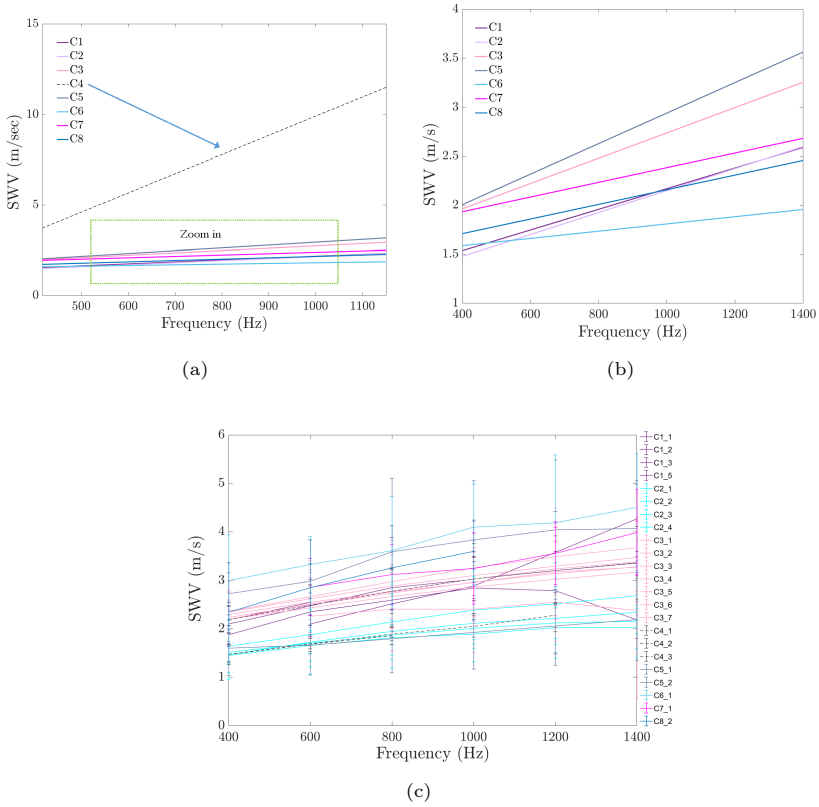

Figure 4.15: Group velocity values obtained from measuring the eight ex vivo human uterine cervix samples. Sub-figures a and b refer to Group velocity of shear waves using SWEI, while sub-figure c displays the same results via TWE. A) The total of the eight ex vivo samples is represented, so one can observe that the cervical sample number 4 shows anomaly velocity values (b) Is a zoom in from sub-figure a.

Table 4.7

Viscoelastic parameters obtained from fitting the TWE results in four rheological models; Kelvin Voigt, Maxwell, Zener and a Kelvin Voigt Fractional Derivate. Where μ is the elasticity in kPa, η is the viscosity in Pa.s, and α is the derivative power.

Cevix Uterine	**Kelvin-Voigt**			**Maxwell**			**Zener**				**Kelvin-Voigt Fractional Derivative**			
Sample	μ(kPa)	η(Pa.s)	R^2	μ(kPa)	η(Pa.s)	R^2	μ_1(kPa)	μ_2(kPa)	η(Pa.s)	R^2	μ(kPa)	η(Pa.s)	α	R^2
1	3.640	0.878	0.965	13.317	1.046	0.996	2.611	2.212	0.350	0.972	3.635	1.782	0.341	0.929
2	2.138	0.420	0.975	4.937	0.575	0.998	1.493	4.445	0.482	0.998	2.188	0.847	0.332	0.943
3	4.743	0.882	0.978	11.924	1.249	0.992	3.855	3.527	0.428	0.999	4.683	1.360	0.493	0.978
4	4.339	1.547	0.971	13.050	1.118	0.996	1.591	8.350	0.363	0.997	4.323	2.081	0.278	0.971
5	2.276	0.352	0.998	19.950	1.751	0.965	2.279	8.626	0.200	0.998	2.270	0.945	0.243	0.998
6	7.991	1.547	0.973	21.640	2.057	0.972	6.918	2.481	0.282	0.987	7.871	2.052	0.544	0.974
7	5.956	1.120	0.966	26.110	1.181	0.920	6.423	1.376	0.030	0.976	5.907	1.796	0.428	0.966
8	3.412	1.347	0.994	68.390	1.143	0.999	2.652	0.985	0.156	0.999	3.342	1.906	0.500	0.994

Table 4.8

Viscoelastic parameters obtained from fitting the SWEI results in four rheological models; Kelvin Voigt, Maxwell, Zener and a Kelvin Voigt Fractional Derivate. Where μ is the elasticity in kPa, η is the viscosity in Pa.s, and α is the derivative power.

Cevix Uterine	**Kelvin-Voigt**			**Maxwell**			**Zener**				**Kelvin-Voigt Fractional Derivative**			
Sample	μ(kPa)	η(Pa.s)	R^2	μ(kPa)	η(Pa.s)	R^2	μ_1(kPa)	μ_2(kPa)	η(Pa.s)	R^2	μ(kPa)	η(Pa.s)	α	R^2
1	2.250	0.386	0.991	17.110	0.453	0.984	1.753	5.083	0.295	0.999	2.193	0.441	0.691	0.990
2	1.533	0.480	0.999	41.080	0.404	0.989	1.576	3.862	0.239	0.999	1.526	1.967	0.157	0.999
3	3.000	0.775	0.999	14.870	0.814	0.983	2.938	3.000	0.246	0.999	2.241	0.802	0.878	0.979
4	10.71	9.150	0.7982	—	—	—	39.730	0.354	0.018	0.999	—	—	—	—
5	2.757	0.897	0.999	119.200	0.7386	0.990	2.998	1.815	0.127	0.999	2.744	4.461	0.129	0.999
6	2.545	0.262	0.989	2.318	0.979	0.928	25.560	3.165	0.276	0.999	2.450	0.898	0.188	0.989
7	3.465	0.5327	0.995	5.654	0.985	0.954	3.328	19.430	0.464	0.998	3.458	3.331	0.102	0.995
8	2.651	0.450	0.996	5.290	0.712	0.961	2.530	20.940	0.405	0.999	2.646	2.481	0.116	0.996

4.2.4.Conclusions and discussion

McFarlin et al. [247] suggested that cervical ultrasonic attenuation, which is theoretically linked to compressional viscosity (independent from shear viscosity), could identify women at risk of spontaneous preterm birth (SPTB). It seemed that low attenuation may be an additional biomarker to identify SPTB. SWEI was conducted *in vivo* on the pregnant cervix of Rhesus macaque, divided into two groups; ripened and unripened specimens [29]. Authors found dispersion (the slope of dispersion curve of SWS versus frequency) in both groups (median 5.5 m/s/kHz, interquartile range: 1.5–12.0 m/s/kHz). Peralta et al. [248] proposed Maxwell's model as the best model to use in preliminary estimations of cervical viscoelastic properties. Myers et al. [176] suggested that since the cervical tissue is mechanically anisotropic, the uniaxial response of *ex vivo* human cervix samples would depend on the load direction.

Jiang et al. [249] employed 3D multifrequency MRE to the uterus and analyzed the viscoelasticity of the uterine tissue in healthy volunteers. They observed that the uterine corpus has higher elasticity, but similar viscosity compared with the cervix, in terms of complex shear modulus (uterine corpus = 2.58 ± 0.52 kPa vs cervix = 2.00 ± 0.34 kPa). They concluded that the proposed technique shows sensitivity to structural and functional changes of the endometrium and myometrium during the menstrual cycle. Shi et al. [250] measured the compressive viscoelastic mechanical properties of *ex vivo* human cervical tissue using indentation and an inverse finite element analysis, to conclude that the human cervix is nonlinear and the area of the internal os is stiffer than the external os.

Previous works have ignored the viscosity and nonlinearity of the uterine cervical tissue. Substantial hydration changes and inflammatory processes are well known during maturation, as well as collagen decrimping, which suggests that viscous and nonlinear parameters may be of significant importance. In this work TWE explored viscosity in ex vivo human cervical tissue. To our knowledge, reporting these viscosity and elasticity values resulting from four rheological models comparing TWE and SWEI are not presented elsewhere and will be of great benefit to the clinical community of SWE. All the rheological models used showed a good adjustment except one. As mentioned at the begining of this chapter, there no consensus in the elastography scientific community on which model is the best for tissue characterization.

"After all, science is essentially international, and it is only through lack of the historical sense that national qualities have been attributed to it."

Marie Curie

Chapter5

Tissue viscoelasticity on bounded media using a modified isotropic TWE probe

5.1.Viscoelasticity of ex vivo porcine cornea samples

Recently, the concept of torsional waves applied to elastography was introduced [251]. Preliminary work was carried out in the field of obstetrics to explore the feasibility of in vivo implementation[252]. Here we propose developing an elastography method based on torsional waves (TWE) adapted to the specificities of the cornea. An emitting disk contacted the outermost layer (usually the epithelium) and generated shear waves that propagate axisymmetrically in depth and radially. A piezoelectric sensor adapted to the curvature of the cornea collected traveling waves through the specimen, which were used to derive biomechanical-related properties based on a Lamb wave empirical expression, required since the cornea geometry limited by two surfaces induces guided propagation of the shear waves. Measurements were performed on ex vivo porcine corneas within the eye, considering five groups, one control and four groups subjected to different alkaline burn treatments that modified corneal mechanical properties. After that, corneas were removed for a tensile test in order to compare the trends of the estimated results. The experimental results showed evidence that this technique could discern different mechanical states and paved the way for supporting current in vivo techniques given its methodological simplicity and fast parameter reconstruction.

5.2.Sample preparation

Porcine corneal samples were obtained from a local abattoir and enucleated immediately post-mortem, then placed in phosphate-buffered saline (PBS, pH 7.4) solution until testing to prevent moisture loss. The buffer solution was prepared using di-Sodium Hydrogen Phosphate anhydrous (Reag. Ph. Eur. 99%), Potassium di-Hydrogen Phosphate (Reag. Ph. Eur. 99% purity) and Sodium Chloride (USP, BP, Ph. Eur. JP 99%) from Panreac AppliChem. To produce changes in mechanical properties, treatment solutions associated with alkali burns that modified the structure of the stroma were selected taking into account the most frequent chemical reactants in house or industrial cleaning products[253]. More than 70% of chemical burns in the eye are accidents occurred at work and 84% of them are due to alkali chemicals[254]. A sodium hydroxide solution 1.5 M (NaOH) was used to simulate the most aggressive chemical exposure in the eye caused by caustic soda. Sodium hydroxide salt was purchased from Panreac AppliChem (98%). Ammonium hydroxide 3mM (NH_4OH at 10% v/v) was used at a similar concentration as usual fertilizers and the double concentration found in cleaning products[255]. Ammonium hydroxide solution (EMSURE ACS, Reag. Ph Eur 28-30%) was purchased from Merck. Both treatment solutions were prepared in MilliQ water. All reactants were used as received without further purification. No treatment was applied to the control group, only washing for 1 minute in PBS.

The whole porcine eyeball was placed in an immersed custom-built holder, and the cornea was orientated side up. The device covered the cornea with gentle pressure, and all samples were measured three times by repositioning for averaging. Measurements were performed at atmospheric pressure.

Preliminary safety considerations were examined. In this modality no cavitation-related problems were expected. Induced displacements were measured with an ultrafast ultrasound scanner (Vantage 256, Verasonics Inc., Redmond, WA, USA) that tracked the wave propagation with plane waves at a rate of 12.5 kHz, placing a 7.6 MHz transducer in a plane perpendicular to the axis of the emitter. Displacement peaked in the control group at around 10μm. Thus, a linear regime was assumed. In a recent study with a similar configuration[252], the maximum acoustic intensity of TWE was estimated at 5.3 mW/cm^2, well below the spatial peak temporal-average intensity limit of 17 mW/cm^2 set by the FDA for ophthalmic applications[256].

A total of 20 samples were tested within the first ten hours post-excision. They were classified considering the treatment and the exposure time (Fig. 5.1), resulting in 5 groups with 4 samples in each of them: control, NH_4OH

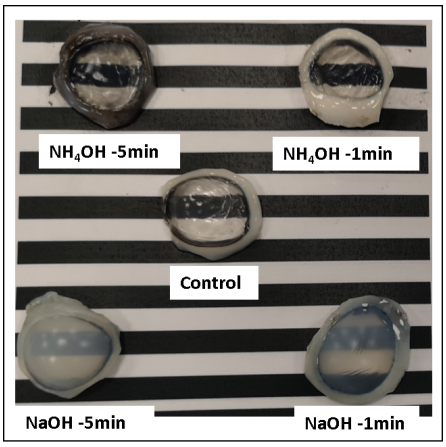

Figure 5.1: Porcine corneal samples of the control and treated groups at different exposure times. The black and white background pattern evidenced structural changes that were more aggressive after sodium hydroxide (NaOH) compared to ammonium hydroxide 3 (NH_4OH), showed by the degree of corneal opacity.

for 1 minute, NH_4OH for 5 minutes, NaOH for 1 minute and NaOH for 5 minutes. The treatment was applied to the entire eye globe by immersion in 50 mL of the respective treatment solution during the established time exposure. Then, the treated samples were washed in PBS and the epithelium was mechanically removed using a spatula. All corneal samples were used for subsequent examination with TWE and tensile test.

5.2.1.Tensile test set-up

Uniaxial tensile tests were conducted to obtain the elasticity of porcine corneas in the five studied groups. The device used was designed and calibrated in the "Ultrasonics Lab" of the University of Granada (Granada, Spain). It comprised two clamps, one that was firmly anchored to the base and another that could move in the vertical direction driven by three synchronized motors. The clamps were printed in ABS (acrylonitrile butadiene styrene) with specific surface roughness to avoid sample slippage. The upper clamp was attached to a digital force gauge (ZTS-50N, Imada Co., Ltd) whose maximum capacity was 50 N, with a resolution of 0.01 N. A high resolution camera with a 4:3 ratio and 2560x1920 resolution (IPEVO Ziggi-HD 5MPix) was synchronized with the displacement of the upper clamp. The monitoring of tissue deformation and the loading steps were controlled by a

Matlab routine.

Table 5.1
Thickness values of corneal population, divided into control and chemical treatments under different times (1 or 5 minutes) groups. No significant differences were found between groups (ANOVA). Values reported as mean ± standard deviation.

Control(mm)	NH_4OH 1-min (mm)	NH_4OH 5-min (mm)	NaOH 1-min (mm)	NaOH 5-min (mm)
1.54±0.02	1.27±0.15	1.47±0.11	1.28±0.09	1.34±0.07

All the samples were cut into vertical strips with two shoulders (that allow the grip of the sample) and a gage section in between, so the deformation of the sample occurs in this part of the central cross-section. The width of the NaOH-treated samples was reduced to avoid saturation of the force gauge. The dimensions of the samples (length, width and thickness) were measured using an electronic caliper (Table 5.1). The samples were preconditioned with 10 loading cycles at 1 N to reach a stage of stable behavior[257]. The tissues underwent a quasi-static uniaxial tensile displacement to the rupture point at a rate of 0.2 mm/s. Acrylic black paint was sprayed over the sample for speckle generation in the samples to improve deformation monitoring. The corneal samples were kept continuously hydrated by spraying them with PBS to prevent a severe alteration of the mechanical properties during the experiment.

Although the stress-strain curve had a nonlinear behavior for the studied deformations, the curve was analyzed in two linear regions for comparing trend values with TWE. In the first region (toe region), the mechanical response was believed to be dominated by non-collagen components of the stroma. The collagen fibrils were initially crimped and then were progressively uncoiling as the load increased. In the second region, collagen fibrils were sufficiently elongated to control the mechanical response (Fig. 5.2). The stress-strain curve was obtained by dividing the force measured in each increment of displacement by the initial section in the most unfavorable area, and the deformation by dividing the displacement by the initial length between clamps. This initial length was set when the sample was stretched under a load of 0.01 N. The thickness of the samples was considered constant throughout the test. For calculating the elasticity in the first region, a linear range of deformation 0.02-0.04% was considered. To determine the elasticity in the second region (mechanical response governed by the collagen fibrils), a searching algorithm was implemented to detect the region of the curve in which the minimal variation of the slope was found between successive points.

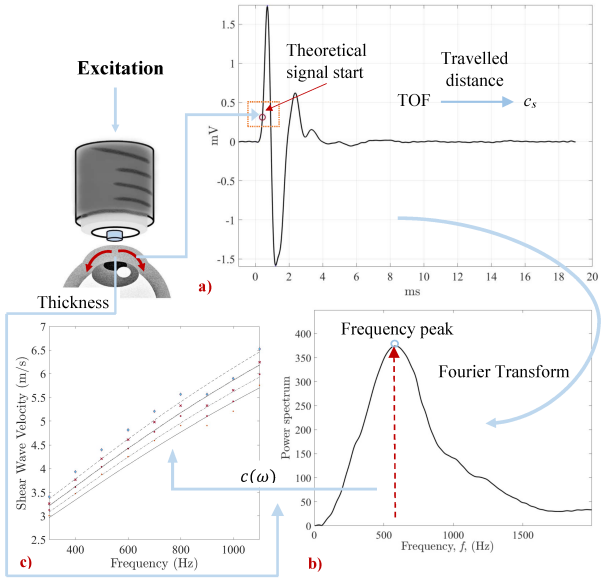

Figure 5.2: Tensile test setup and data analysis: a) front camera view, where a sample was clamped and attached to the force gauge at the top; b) typical stress-strain curve of a control group sample, the regions selected to estimate the elasticity modulus were a linear toe region K1 (non-collagenous response), and a linear collagen response region K2.

5.3.Statistical Analysis

The results of thickness, tensile testing and TWE were reported with mean and standard deviation. One-way ANOVA was applied to compare the mean of the different groups, followed up by Tukey post-hoc tests when significant differences were found to analyze specific differences between groups. Normality was checked with Q-Q plots. Statistical significance was set at two-tailed p-value 0.05 ($p<0.05$* significant, $p<0.01$** very significant, and $p<0.001$*** highly significant), and data were analyzed using R (Version 4.0.2).

5.4.Results

5.4.1.Tensile Tests

A representative stress-strain curve for each group is shown in Fig. 5.3, where the maximum value of stress marks the starting point of breaking of the sample. Visually, a steeper slope and higher stress are observed in the

treated groups with respect to the control (solid black line). No significant differences were observed between exposure times with the same treatment in any slope region ($p>0.05$). Treated groups showed a substantial modification of their elasticity with respect to the control group. In both regions (K1 and K2), significant differences were found between the NaOH group and the other groups, but they were non-significant between NH_4OH and control groups. The average values of the modulus of elasticity for each group and curve region are represented in Table 5.2.

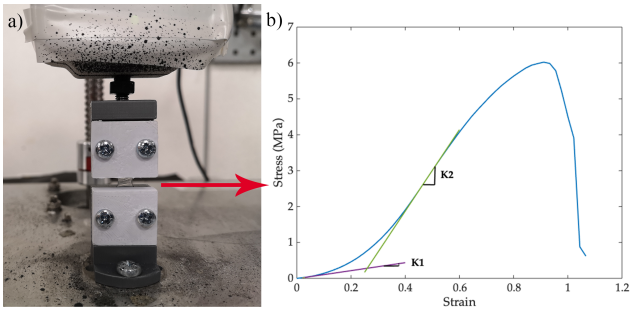

Figure 5.3: Typical stress-strain curves showing the response of each treatment group. The maximum stress marks the starting point of tissue rupture.

Table 5.2
Tensile average elasticity modulus for each treatment group and analyzed region. Differences between groups are also presented. Samples were grouped by treatment and not exposure time since they did not show significant differences.

Group	Elasticity modulus in K1 (kPa)	Elasticity modulus in K2 (kPa)
Control	717.25±451.48	4638.75±1722.92
NH_4OH	818.42±531.45	8731.28±2789.29
NaOH	3102.25±1927.04	17275.50±2832.08
Control vs NH_4OH	p=0.98	p=0.06
Control vs NaOH	p=0.02*	p<0.001***
NH_4OH vs NaOH	p=0.01*	p<0.001***

5.4.2.Corneal Elasticity by TWE

Each group was excited with three frequencies: 600, 800, and 1000 Hz. Here, only the results corresponding to 1000 Hz were presented, since they showed a lower standard error and higher bandwidth, which was better suited for further analysis and comparison with the tensile test. As in the tensile results, no significant differences were found between exposure treatment times

($p>0.05$). Figure 5.4a displays a summary of the measured elasticity values with TWE. As the chemical treatment was more aggressive using NaOH, a higher elasticity modulus was calculated, being the differences between NaOH group and the other groups highly significant. The mean values with their standard deviation were 391.08 ± 66.03 kPa, 498.99 ± 111.42 kPa, and 738.47 ± 132.21 kPa, respectively for control, NH_4OH and NaOH groups. No significant differences were found between control and NH_4OH in any method, meaning that the mechanical alteration was not relevant at the macroscopic level.

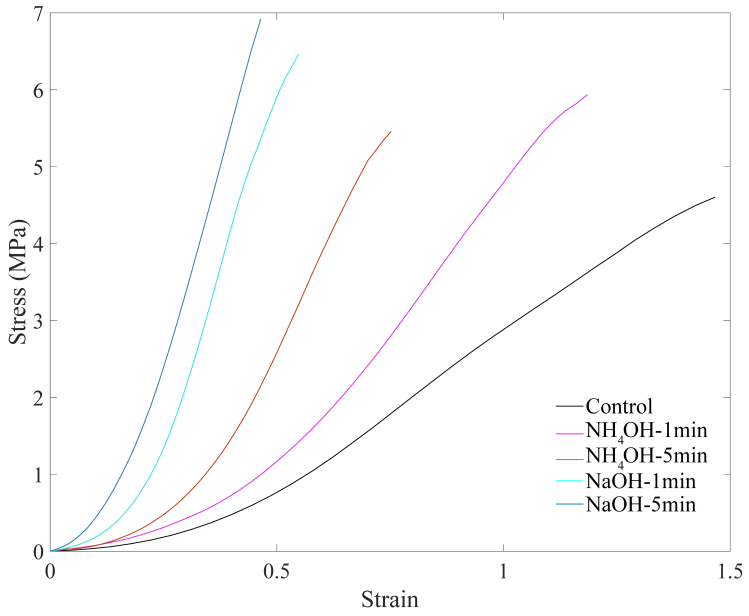

Figure 5.4: Torsional Wave Elastography (TWE) results: a) box plots of TWE elasticity values given each group. Highly significant differences were found between NaOH-group and the other groups, but they were non-significant between NH_4OH and control groups. (ns: no significant); b) bar plots of elasticity for the treated and control groups measured by TWE and tensile tests. Error bars represent the standard deviation in each group; c) representative Shear Wave Speed dispersion curves of each group. The empirical Lamb wave speed is marked every 100 Hz. Lines correspond to the Kelvin-Voigt fits for each group with the same color code.

A qualitative comparison between TWE and the tensile test was carried out,

bearing in mind the differences in temporal and spatial scales. The linear toe region (K1) was chosen for comparison, since the deformation of the samples at this interval was within a similar range to TWE (see Fig. 5.4b). In the second region (K2), samples underwent a higher deformation range, unrealistic for any elastography technique. The results showed that a similar trend was followed, and that TWE, as the tensile test, was able to distinguish mechanical alterations when they were substantial, such as the case of NaOH-treated corneas, with differences close to an order of magnitude. Furthermore, measurements obtained with TWE showed a reduced standard deviation compared to the tensile test.

5.4.3. Viscoelasticity Estimation of the Cornea

As a dispersive medium, the cornea showed that different excitation frequencies affected the final estimation, with higher speed related to higher frequencies. Phase speed was calculated between intervals of 100 Hz in the range of 300 to 1200 Hz, where the maximum energy of its power spectrum was reported. Figure 5.4c shows the KV fitted lines of the dispersion curves of representative samples. It was observed that the phase speeds in the two treated groups were higher than the control group, and this difference widened under NaOH treatment. The mean values for the KV fits are reported in Table 5.3. The results showed that both shear elasticity and viscosity increased in the treated groups compared to the control group.

Table 5.3
Viscoelastic parameters for ex vivo porcine corneal samples using Kelvin Voigt (KV) model on elastography results.

KV parameters	Control	NH_4OH 1-min	NH_4OH 5-min	NaOH 1-min	NaOH 5-min
Shear Elasticity μ_1 (kPa)	5.11±0.41	5.61±1.15	5.57±0.63	6.08±1.00	6.61±0.62
Shear Viscosity μ_2 (Pa·s)	2.83±0.22	3.11±0.63	3.09±0.35	3.37±0.55	3.66±0.34

5.5. Discussion

In this study, the diagnostic capabilities of TWE were evaluated on a geometry as specific as that of the cornea. Unlike other organs such as the cervix[252] or liver[258], the translation to measure corneal elasticity was governed by the complex propagation of guided waves. A simple calculation of the group speed assuming pure elasticity might lead to significant bias[259], since generated waves are very dispersive, thus depending on the frequency range. In our case, the antisymmetric A0 mode was assumed to be the dominant mode at the response frequencies, for which an experimental expression had already been derived. Therefore, one small source of error was expected as the contribution of other guided wave modes was ignored,

but possibly captured in the standard deviation of the estimation.

As the chemical treatment was more aggressive, a higher elasticity was recorded, for which it is hypothesized that instead of a weakening of the interlamellar integrity, at first, the alkali burn rearranged the components of the stroma through melting, whereupon the proteoglycan matrix would contribute by resisting higher deformation[260]. Another possible explanation was suggested by Nguyen et al.[261], where the removal of epithelium after treatment increased elasticity, probably due to dehydration in ex vivo conditions.

For comparison purposes, the results obtained with TWE and the uniaxial tensile test technique showed that calculated elasticities were coherent, registering higher values in the treatment groups with respect to the control group. The deformation range for the stress-strain curve (K1) was chosen because the deformation that the cornea undergoes when guided waves are generated is within the same range, providing similar values with both techniques. The large difference between methods could be justified by experimental conditions inherent to destructive evaluation. The geometrical constraints imposed, such as clamping and the edges, and loss of curvature due to stretching, directly affected the microstructure. The tensile strain rate also played a role due to viscoelasticity, since it was observed that higher rates resulted in higher elasticity[262]; yet it could be considered a convenient technique for comparative studies.

In the literature, very mixed results were found, which are a consequence of the different time- and length-scales used, wave models, as well as experimental conditions, reaching ambiguous conclusions. Still, the elasticity values presented here, 391.08 to 738.47 kPa, were consistent with previous studies, ranging from 160 to 890 kPa under different setups and treatments[263, 264, 265, 266]. Experimental variations include IOP, a factor that was found to be positively correlated with elasticity[267, 268]. Increasing IOP stretches the cornea, introducing nonlinear elastic effects and affecting wave propagation[263]. However, very recently, Ramier et al.[265] found no correlation between these magnitudes, possibly due to a convenient distribution of stress in the human cornea in vivo. Another factor essential during ex vivo experiments is hydration. It is known to be a confounding factor due to corneal dehydration, resulting in tissue thinning and increased elasticity[269, 270]. Thus, the thickness can be considered a surrogate of hydration in equation (2), where higher elasticity was expected in thinner corneas. Interestingly, the difference in thickness between samples treated for one minute and the control was nearly significant (Table 5.1), which may

explain why 1-minute groups exhibited slightly higher shear elasticity, as showed in Table 5.3.

Several studies have tried to shed some light on the potential of viscoelastic biomarkers by associating corneal hysteresis with viscosity in air-puff applanation experiments, since they observed lower hysteresis values in keratoconus, post LASIK, and Fuch's dystrophy patients[271]. In this study a simple Kelvin-Voigt model was used. The application of this model is subject to the assumption that the medium is macroscopically homogeneous, isotropic, and linear, besides no guided waves are generated. Since these conditions were not met, in addition to using an empirical expression, important differences with other studies were found. In the literature, there is a lack of corneal shear viscosity values under the same configuration for comparative purposes. Shear viscosity or viscosity parameter was mainly reported after using OCE, with values below 1 Pa·s[272, 273, 274, 259], whereas this study reported a range of 2.83 to 3.66 Pa·s. The increasing viscosity was expected since it was directly related to the increasing shear wave speed inherent to KV model. Shear elasticity results ranged 5.11 to 6.61 kPa, which was in agreement with the values reported in the same previous studies. Both shear elasticity and viscosity increased after chemical treatments, in a similar manner as described by Weng et al.[259].

The values presented by TWE were an average of global mechanical properties that translated into a fast reconstruction method, taking less than 7 seconds to calculate the group speed. In contrast to other techniques, where a map was reconstructed, no analysis artifacts were detected, such as diffraction or attenuation. However, some limitations of the current method need to be detailed. The TOF algorithm used only calculates the group speed, then, for further analysis, supplementary expressions such as equation (1) were required, where the significant dispersion and phase speed of waves were not directly considered. Boundary conditions like stress distribution generated by IOP confer a preloaded state, which could be modified if there is direct contact, biasing the results. TWE likely missed focal abnormalities since no 2D image was obtained.

The in vivo implementation of acoustic or optic-based techniques should improve the management of current applications, such as early detection of ectasia, evaluation of damaged corneas by different aggressions (e.g. chemical burns, corneal inflammation and fibrosis, etc.), corneal treatment customization, evaluation of IOP adequately corrected by mechanical corneal parameters, or the assessment of artificial corneas, just to name a few. Additionally, regular monitoring may indicate signs of corneal degeneration or ageing.

Thus, TWE has the potential to be integrated into conventional examination procedures, but several points need to be further studied. Although direct corneal contact is necessary, it is not an unfamiliar methodology with routine protocols such as tonometry or corneal pachymetry, where topical anesthetic is instilled. Besides, a stable excitation is achieved in this modality, and by changing the diameter of the emitting disk, the exploitable frequency bandwidth of the response is expected to increase. To be on the side of safety, the effect of the pressure exerted when measuring will be studied in the future, both to assure an efficient propagation of torsional waves, confirming that local induced stresses do not severely affect wave propagation, and to avoid patient discomfort. On the other hand, this applied pressure could become an opportunity to obtain nonlinear elasticity parameters, as in acoustoelasticity, whose relevance could be substantial[253, 275]. Since it is difficult for patients to maintain a fixed position or avoid involuntary movements, the short times required to take measurements are an additional benefit that helps reduce motion artifacts. As recently reported[259], the use of Lamb wave models is required for a more accurate description of the viscoelasticity of the cornea, then its feasibility with TWE should be studied. The measurement of corneal thickness here was done manually after excising it for tensile testing, but it can be done in vivo with pachymetry. Some studies suggested that the cornea is an anisotropic tissue with an accentuated mechanical heterogeneity, but when IOP was under 10 mmHg no dependency was found in the measured direction[264]. Accordingly, our results should not have been affected in this respect. Future studies should implement a suitable Lamb wave model, anisotropy and nonlinearity, and prove the feasibility of using TWE with in vivo animal studies combined with standard equipment.

"You cannot hope to build a better world without improving the individuals."

Marie Curie

Chapter6

Assessment of shear stiffness of soft tissue using anisotropic TWE probe

The field of dynamic elastography is gaining more and more attention in pathological diagnosis because it is based on the propagation of shear waves, whose velocity is directly related to the shear modulus. This is an ideal elastic parameter for examining soft tissues because it is known to be sensitive to changes in the microstructure of the extracellular matrix (ECM), related to a possible underlying pathology [276]. The content and distribution of collagen fibres have been identified as the main contributors of the mechanical response [4]. For most soft tissues, the current standard is to develop results based on the simplifications provided by a linear elastic isotropic medium [277, 278]. The consideration of isotropy implies a direction-independent quantification of elastic parameters, facilitating the implementation of in vivo measurement protocols. This has helped the publication of a significant number of studies on tissues that can be considered macroscopically isotropic, such as breast or liver [279, 278]. However, significant variations in propagation velocity have been observed within the same tissue. The relevance of mechanical anisotropy is originated from the histological composition [280, 281], and can be verified by changing the relative orientation of the measuring device [282], or the anatomical region examined [283, 118]. If a high variability in the results is observed, the effect of anisotropy cannot be ignored. This is further emphasized given the polarized nature of shear waves, yielding unexpected apparent velocities. Two directions define its physics, the propagation direction, and the particle direction, which are mutually perpendicular. This behaviour was properly illustrated by the transient elastography technique, where shear waves were generated by the contact of an external vibrator [284, 282]. It

was observed that when the polarization of the waves was parallel to the fibres, higher velocity was recorded than when it was perpendicular. On the other hand, when the excitation comes from acoustic radiation force [285], it is usually not feasible to position the probe for the polarization to be parallel to the fibre direction. That is the case of skeletal muscle and tendon, which have a unidirectional organization of collagen fibres within the ECM, and where the longitudinal dimension is not accessible to generate shear waves. To address its study, the propagation medium was modeled as transverse isotropic, with the main direction of fibres considered as an axis of symmetry, and all perpendicular planes deemed locally isotropic [286]. Given the angle of propagation respecting the plane fibres, the parallel and perpendicular shear moduli were reconstructed, resulting in higher magnitudes when the wave propagated along fibres (parallel), than across fibres (perpendicular) [284, 287, 106]. Similar conclusions were found by using phantoms to study the shear wave propagation in transverse isotropic solids [288, 289]. Therefore, it is expected that within a strong organized tissue, the wave will encounter less resistance in its path. When this organization is locally disrupted, e.g., clusters of fibres oblique to the main axis, or different preferential directions, anisotropic artifacts arise, and the velocity estimation is biased. This is the case in tissues such as the kidney or the cervix, which cannot accept the assumption of transverse isotropy. To provide a better understanding of their mechanical behaviour, it is essential to estimate their velocities given specific directions.

The cervix is a cylindrical shaped tissue located between the vagina and the uterus. It is regarded as highly anisotropic due to the presence of the cervical canal, different fibre orientations and its vasculature, rendering an heterogeneous medium. The ultrastructure of the collagen network presents different directions that are anatomically established based upon the mechanical reactions that occur during the gestation with the purpose of resisting dilation [25]. The directionality of the fibres was studied with different imaging techniques, finding that the cervix has two radial zones [290, 291, 292]. An inner zone of about 3 mm surrounding the cervical canal, aligned with its axis, to resist the tensile forces of the effacement. The outer zone is a band of circumferential aligned fibres, encircling the shape of the tissue to prevent dilation. However, Gan et al. found no trace of the inner zone in pregnant samples [293]. Also, uniaxial load trials on pregnant and non-pregnant cervix tissue showed non-linear, viscoelastic and anisotropic behaviour [172, 176]. Non-pregnant cervices had more aligned and less dispersed collagen fibres than pregnant cervices. It is now clear that the importance of the cervix lies in the fact that it has been identified as the key physiological element during

pregnancy [25]. The remodelling process that this tissue undergoes until delivery has been proposed as a biomechanical indicator for the detection of premature birth or cervical dysfunction [294]. Therefore, the characterization of wave propagation in each direction is of interest in understanding the function of the cervix and the progression of labour disorders.

Current commercial elastography-based devices are not capable of measuring tissue anisotropy directly. The use of linear or curved transducers implies insonification of the medium under study to obtain an image that is a projection of the transducer surface. To obtain a first approximation of the anisotropy of the tissue, it is necessary to collect measurements while the transducer rotates on its own axis. It has been proposed to use CNC rotating machines with a high precision of angular displacement where the transducer is fixed, standing as an efficient methodology in in vitro or ex vivo settings, where the study sample can be arranged at will. Very promising experimental results have been obtained, in addition to being able to generate a 2D maps with elastic properties [91, 295, 287, 286, 288]. However, in in vivo situations it would be very complicated to re-engineer this configuration given the complex shapes of human and animal anatomy. Also, the long scanning times of some techniques can be as long as 10 or 30 minutes, even if ultrafast imaging is used. This would be a challenge to apply in vivo due to movement and discomfort on the patient. Other techniques, such as elastic tensor imaging, provide the projection of the direction of the fibres in the measuring plane, also involving the rotation of the transducer [296].

The lack of measurements using dynamic elastography on the anisotropy of the cervix motivated this study. Experimental evidences come from traditional tensile or indentation studies on histological sections that follow the direction of fibres [30, 250]. Interestingly, our group has developed a torsional wave sensor that emits and receives shear waves, whose main advantages are the absence of spurious longitudinal waves and a good safety margin since the projected frequency range is low and the deposited energy minimal [202, 134]. This new technique allowed the quantification of the shear modulus in three different directions of the specimen at the same time.

6.1. Tested samples

We proposed a three-step device validation. First, phantoms configured with different fibre orientations were used to check the ability to measure different directions. Secondly, an ex vivo animal model, such as a chicken breast, where the fibre direction could be clearly observed, verified that the

ranges of values were in agreement for soft tissues. Finally, the fea sibility of characterizing the anisotropy in ex vivo cervical tissue was tested.

Homemade homogeneous phantoms were prepared. They were made from porcine gelatin powder at 7.5% gelatin concentration (Fisher Chemical, Lei cester shire, UK) and 0.5% of sodium dodecyl sulfate (Sigma-Aldrich Corp., St. Louis, MO, USA). A sonicator (Fisherbrand 505, Thermo Fisher Scientific, Inc., Waltham, MA, USA) was used to homogenize the mixture. The energy amplitude was set at 70% of 500 W maximum, and the frequency at 20kHz with cycles of 55s on-time and 5s off-time for 20min. The final mixture was allowed to reach room temperature, and when visible bubbles disappeared, it was poured into the chosen moulds. One phantom was poured without fibres inclusions, the second one had fibres embedded in one direction, and the last one had non-aligned fibres (PLA 3D printed) Figure 6.1.

Figure 6.1: Ingredients for fabrication of hydrogel phantoms with embedded fibres.

A silicone phantom was used with fibres inserted inside and 2mm apart Figure 6.2. This distance allows a relatively simple assembly. Measurements were made on the silicone surface in parallel, perpendicular, and intermediate positions to fibres orientation.

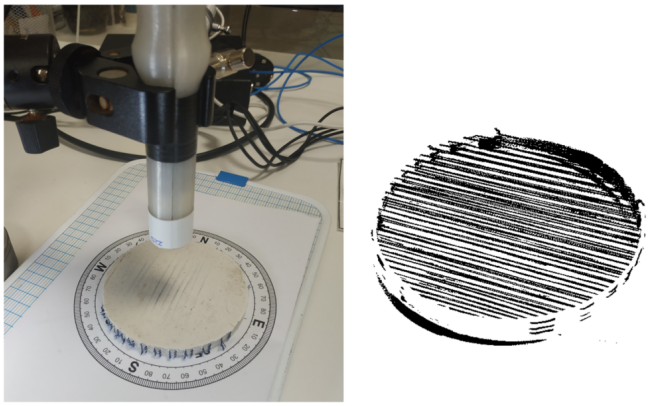

Figure 6.2: Silicone phantom with embedded textile fibres in a in a selected direction.

6.2.Experimental set-up

The anisotropic TW probe Figure 6.3 was placed in contact with the samples at a controlled pressure. Each piece was measured three times for repeatability. The procedure for TWE scans is as mentioned in chapter 3 of this document. The probe was first calibrated using three *cirs* commercial phantoms Figure 6.4. Figure 6.5 illustrates the TWE set-up for a hydrogel phantom.

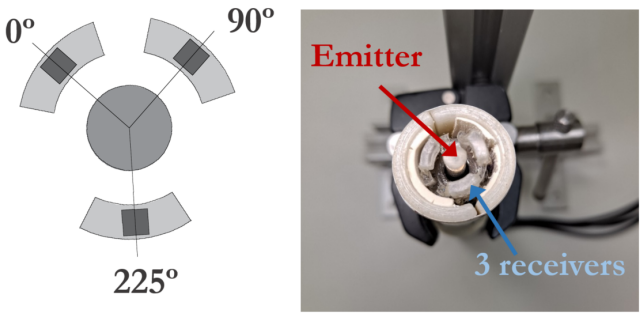

Figure 6.3: Left: Cross-section of the anisotropic TWE probe representing the 0^{o}, 90^{o} and 225^{o} sectors. the right subfigure shows the emitter and the receivers

Figure 6.4: Calibration of the TWE probes was done using commercial cirs phantoms.

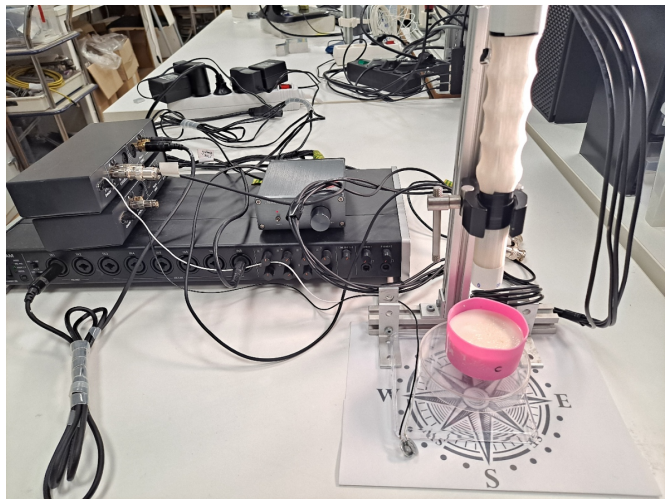

Figure 6.5: TWE set-up to scan hydrogel phantoms with embedded fibres.

6.3.Results

6.3.1.Phantoms with embedded fibres

Hydrogel gelatin phantoms were tested via TWE technique. Scans were made in a homogeneous control phantom (with no fibres) and in another two phantoms, one with aligned 3D printed fibres in one direction and the other with randomly distributed fibres. All were scanned at a frequency of 1000Hz. From Table 6.1 One can see that the control phantom stiffness values are similar in the three directions. In the second case, when the fibres are aligned in only one direction, we can see that the stiffness (μkPa) is considerably higher when we measure aligned to its direction. The third and last case shows the chaos when the scans are done to the randomly distributed fibres phantom.

Table 6.1
Tissue mimicking phantoms, without and with aligned and non-aligned 3D printed fibres measured with TW sensor

Control tissue mimicking phantom (without fibres)				
Frequency (Hz)	Mean Stiffness μ (kPa) and standard deviation			N=3
	0^o sensor	90^o sensor	225^o sensor	
1000	20.8827±2.6983	19.1632±3.2681	20.1189±2.5196	
Tissue mimicking phantom (with aligned fibres orientatet towards north direction)				
Frequency (Hz)	Mean Stiffness μ (kPa) and standard deviation			N=4
	0^o sensor	90^o sensor	225^o sensor	
1000	145.8259±34.4923	21.2633±1.0278	19.6110±3.2694	
Tissue mimicking phantom (with non-aligned fibres)				
Frequency (Hz)	Mean Stiffness μ (kPa)			N=5
	0^o sensor	90^o sensor	225^o sensor	
1000	37.7980	22.0811	26.7027	
	136.8140	8.2650	11.5826	
	39.6569	10.7216	9.7150	
	43.8111	37.7980	19.8619	
	106.1326	23.7739	15.8237	

Table 6.2
Silicone phantom with aligned fibres measured by the different channels

Frequency (Hz)	silicone phantom with aligned fibres	Stiffness μ (kPa) 0° sensor	90° sensor	225° sensor
700	mean of 6 meassurements	179.549±6.306	84.342±3.445	123.771±3.886
1000	mean of 6 meassurements	207.560±6.193	90.452±4.585	144.424±4.126
1300	mean of 6 meassurements	229.926±3.977	106.715±4.958	177.075±5.856

Scans over silicone phantom return similar results, TWE was done at 700, 1000 and 1300Hz, the values in Table 6.2 are mean values of six measurements.

6.3.2.Ex vivo chicken breast samples

As in previous chapters, ultrafast imaging was done by a Verasonics US research system (Vantage 256, Verasonics Inc., Redmond, WA, USA). The $L11_5v$ transducer was placed once aligned with the breast fibres, and another scan was done with the transducer across the sample fibres. The experimental set-up is shown in Figure 6.6.

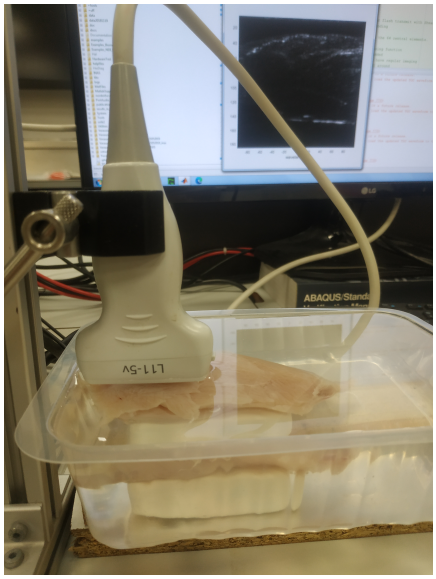

Figure 6.6: Set-up for ex vivo chicken breast scans via SWEI

From the Bmode we can see the perfectly distributed and aligned fibres in this type of soft tissue (Figure 6.7).

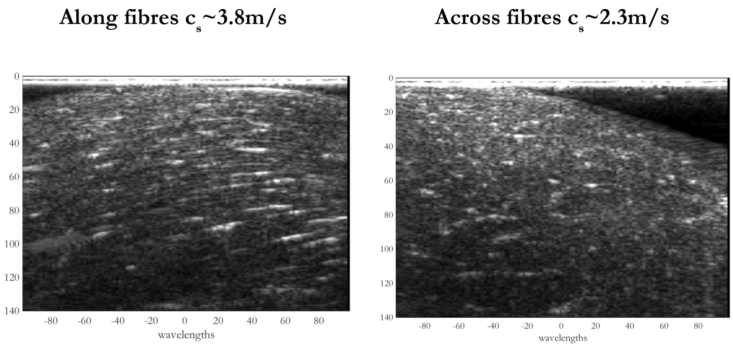

Figure 6.7: Bmode of ex vivo chicken breast positioning the SWE $L11_5v$ transducer along and across its fibres.

Table 6.3
Ex vivo chicken breast measured by TWE using the three different channels at once.

Frequency (Hz)	Ex vivo chicken breast	Stiffness μ (kPa) 0° sensor	90° sensor	225° sensor
700	mean of 3 meassurements	40.752±1.407	16.247±1.631	32.258±0.960
1000	mean of 3 meassurements	43.573±1.555	17.848±1.073	33.603±2.017
1300	mean of 3 meassurements	56.253±2.359	19.846±1.644	36.719±1.198

The push transmit frequency was set to the transducer centre to allow maximum transmission efficiency to transfer the ARFI to the tissue. An identical set was used for tracking frequency. Shear wave group velocity of ex vivo chicken breast along and across its fibres is determined after post-process the IQ data, and results are shown in Figure 6.8. As expected, the group velocity is higher when the shear wave travels along the fibres.

Same samples were measured using the anisotropic TWE probe, at three frequencies 700, 1000 and 1300Hz. Results are tabulated in Table 6.3 and are in concordance with those obtained from SWEI.

6.3.3.Ex vivo human uterine cervix

A total of three hysterectomy specimens from women with benign gynaecological conditions were obtained from Health Campus Hospital in Granada Table 6.4. The study met the principles of the Declaration of Helsinki. Approvals of the Ethical Committee in Human Research of the University of Granada and Ethical Commission and Health Research of Health Campus Hospital in Granada were achieved. All women enrolled in the evaluation

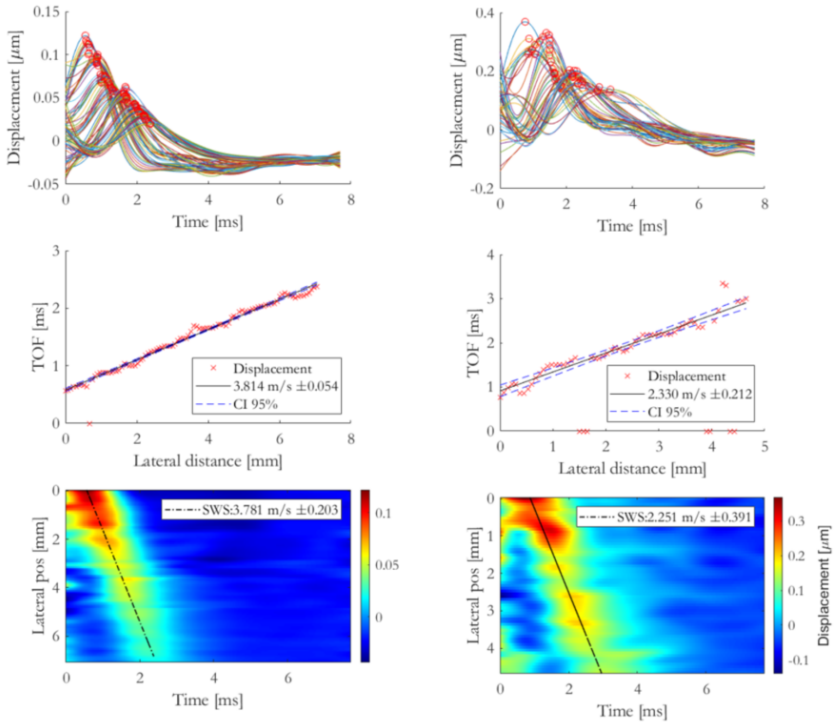

Figure 6.8: Shear wave group velocity of ex vivo chicken breast along and across its fibres.

provided an agreement by signing a written consent and reading the information of the patient report.

Table 6.4
Patient demographics of specimens used for this study, parity data are presented in the TPAL recording system. TPAL stands for term, preterm, aborted, and living deliveries, corresponding, respectively, to each of the four digits

Specimen number	Age	Pregnancy status	Parity	Obstetric Histology
1	77	NP	4004	Vaginal Prolapse
2	69	NP	3003	Vaginal Prolapse
3	85	NP	5005	Vaginal Prolapse

The same steps for ex vivo chicken breast were repeated to test the three ex vivo human uterine cervical tissue samples. The torsional experimental set-up is shown in Figure 6.9. Each sample was measured at a controlled pressure, three times, and within a frequency range from 700 to 1000Hz. Results are shown in table 6.5.

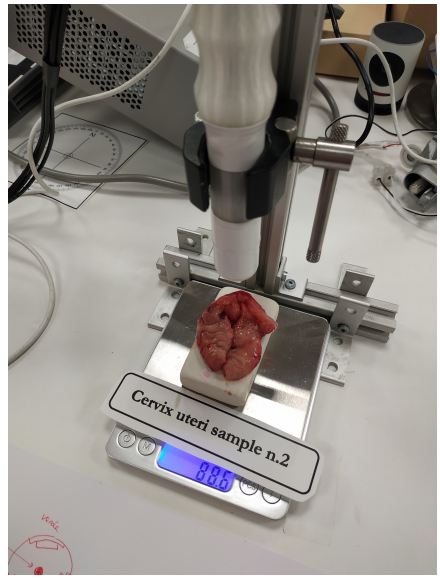

Figure 6.9: TWE set-up for ex vivo human uterine cervix.

Table 6.5
Ex vivo human uterine cervix measured by the different channels

Frequency	ex vivo human uterine cervix	Stiffness μ (kPa)		
		0° sensor	90° sensor	225° sensor
700	1	25.350±0.798	18.879±1.022	12.960±1.630
900	1	25.251±1.457	20.492±1.461	12.854±1.423
700	2	13.421±0.898	10.703±0.203	7.125±0.584
1000	2	26.997±1.578	20.534±1.511	13.413±1.207
900	3	56.020±3.805	32.863±2.738	22.230±2.909
1000	3	63.390±3.045	40.251±2.763	22.214±2.613

6.4.discussion

Any technique that has the potential to be used *in vivo* must have the ability to measure in different directions. For a more accurate quantification the effect of anisotropy cannot be neglected, otherwise it would limit the interpretation of the findings. We have shown how TWE could be adopted to study the effect of anisotropy in various media with respect to the shear modulus. The mechanical complexity of the cervix, reflected in part by the anisotropy, should not be an obstacle, but an opportunity to demonstrate the value of TWE.

Propagation perpendicular to the fibres was reported to be noisier, with higher variability and attenuation, which was also related to higher viscosity [106].

The variability of the results, as well as their comparison with other studies, may be justified by the different ranges of collagen content that have been published in the literature [179, 1]. Shi et al. reported that the posterior and anterior parts had a more marked fibre alignment than the left and right parts [250]. Just as it is important to know the excitation frequency for possible dispersion effects, it is also important to start reporting the direction of measurement. This will facilitate future comparisons. In addition, for longitudinal studies where the evolution of the mechanical remodelling is observed, the measurement orientation should be recorded to avoid confusing misdiagnosis. Advantages of TWE: the acquisition process took less than 3 seconds, it can be easily converted into a freehand portable system, a sufficient frequency range can be generated for dispersion and rheological characterization.

The differences between values obtained are an indirect measure of the degree of anisotropy, probably associated with fibre alignment. This gives insights

into the in vivo potential of this technique, since it has been shown that there are no significant differences from an in vivo to an ex vivo cervix environment [297]. There are several factors that made it difficult to compare the results obtained. First, the cervix has a complex geometry with very specific boundary conditions, such as cylindrical shape and the existence of a canal. Secondly, there is a dependence on the obstetrical and gynaecological history of the samples. This information is essential in order to rule out possible alterations in shear modulus, and to conclude that the variation in results were mostly due to anisotropy. And yet, samples with the same history have showed significant variability [176].

TWE opens the way to in vivo studies in combination with shear wave elastography (SWE). Current SWE equipment measures in the sagittal plane of the cervix by placing several Q-boxes in different regions of interest. Although it is difficult to obtain information about the local velocity distribution, TWE could indicate the directions and regions of greatest interest.

The major aim of elastography should be to understand the pathogenesis of the tissue under examination. A histological study would have complemented the interpretation of results, by allowing mechanics and microstructure, especially the collagen ultrastructure, to be related.

Future: increase the number of measuring sectors. It would be of great interest to differentiate the contribution of anisotropy and attenuation. For further exploring the torsional wave propagation, the fabrication of cylindrical phantoms with a similar fibre distribution as the cervix will be proposed. Increase the sample size of ex vivo samples with different obstetric records to explore its effect on collagen distribution.

"All my life through, the new sights of Nature made me rejoice like a child."

Marie Curie

Chapter7

Nonlinear viscoelastic characterization of the cervical tissue

Modelling of soft tissue implies new perspectives that carry several clinical applications. It could be used, for example, in tissue engineering [298, 299, 300], for finite element modeling [301, 302, 303, 304], to analyze virtual reality in clinical practice [305, 306] and for surgery planning [307, 308]. To simulate those applications, the theory of linear elasticity has been employed to understand the results of mechanical tests on soft tissues [309, 310]. However, surgical procedures lead to consider large displacements and linear elasticity is a simplification when considering small strains. There is a need among researchers to use simplified models which can represent the nonlinear behavior of soft tissues. The simplicity of the proposed model in conjunction with a good correlation with the experimental data can be presented as an accurate and simple model in computational solid mechanics field.

Although the nature of soft tissue behaviour is viscoelastic [138], a simplification of hyperelasticity allows a reasonable characterization of the mechanical properties, specifically when the loss of strain energy is small (low loading rates). Veronda and Westmann [162] and Fung [163] were the first works that used hyperelasticity for soft tissue modeling. The hyperelastic approach postulates the existence of the strain energy function which relates the displacement of the tissue to the corresponding stress values [164]. The most common strain energy functions for the modeling of soft tissues are polynomial forms, such as Mooney–Rivlin and Ogden models. Many authors have modeled the behaviour of soft tissues such as, porcine spleen, porcine kidney, porcine liver, rat or human brain [165, 166, 167, 168, 169]. Regarding cervical tissue, uniaxial tension tests [170, 171, 172, 173, 174] and compression [172, 175, 176] have been studied in rat tissue and human tissue using load-relaxation protocols. A nonlinear stress–strain response has been shown in the tension and compression tests and the response of the

tissue was noticeably stiffer in tension than in compression. It was observed that tissue from pregnant patients was one to two orders of magnitude more compliant than tissue from nonpregnant patients [172, 176]. In a work carried out by Yoshida et al. [174], load relaxation ring tests were performed on pregnant and nonpregnant rat cervices. The pregnant tissue showed a very large stress-relaxation compared to the nonpregnant tissue. Myers et al. observed that the cervix stiffness changes along its length in the uniaxial tensile test, where the external os had a stiffer response than the internal os [172]. The relationship between stiffness and gestational age was studied by Poellmann et al. and Jayyosi et al. [173, 177]. The works concluded that stiffness decreased as gestational age increased. In the works mentioned above were uniaxial, compression and traction tests were performed, the mechanical properties of the tissues have been obtained. However, in those works the nonlinear elastic properties of ex vivo human cervical tissue, using the Fourth Order Elastic Constants (FOECs), Ogden, and Mooney-Rivlin models have not been obtained through uniaxial tensile tests yet.

Soft tissues are composed of several layers; each one of these layers has different compositions, for instance, cervical tissues have an epithelial outer layer and a connective layer. The connective layer is composed by an extracellular matrix (ECM) that ensures the strength and integrity of the cervix, resisting shear deformation, through a fibrous scaffold [178]. The main component of the ECM is fibrillar collagen, which determines a cross-linked network interlaced with the elastin protein, enclosed by a ground substance of proteoglycans and glycosaminoglycans [179, 180, 181]. Researchers have identified three zones of structured collagen in the connective layer: the innermost and outermost rings of stroma contain collagen fibres preferentially aligned in the longitudinal direction, and the middle layer contains collagen fibres preferentially aligned in the circumferential direction [182, 183]. Regarding the collagen content, the middle zone had higher levels of collagen content when compared with the inner and the outer zones [183]. According to the mechanical studies on soft tissues, the connective layer is often considered as the most important from a mechanical point of view [184, 185, 186]. However, other studies, based on Torsional Wave Elastography, consider the epithelial layer as a key apart from the connective one [187, 134, 188]. The reason is that torsional waves not only propagate in depth but along the surface before being registered by the receiver. One of the purposes of this work is to study the differences in stiffness between the epithelial and connective layers of ex vivo human cervical tissue that comes from the hyperelastic models employed.

The main aim of this part is to propose a new hyperelastic model based on

FOEC in the sense of Landau's theory. The evaluation of the agreement between classical hyperelasticity theory and acoustoelasticity theory, in particular third and fourth order elastic constants, in predicting the mechanical response has potentially high impact. Recent advances in medical imaging techniques for non-invasive evaluation of rheological behavior of soft tissues provides new perspectives, in particular for in vivo quantification of nonlinear shear wave-based elastographic biomarkers, which could be diagnostic predictors of a broad spectrum of labor disorders.

7.1.Nonlinear shear waves in tissue

7.1.1.Evidence 1: Prestress-dependency

Soft tissue is highly nonlinear: highly hiperelastic, that means that stiffness changes what we precompressed it which, and this is visible by apparent changes in phase velocity. An example of the effect of the applied pressure on ex vivo human uterine cervical tissue is shown in Figure 7.1

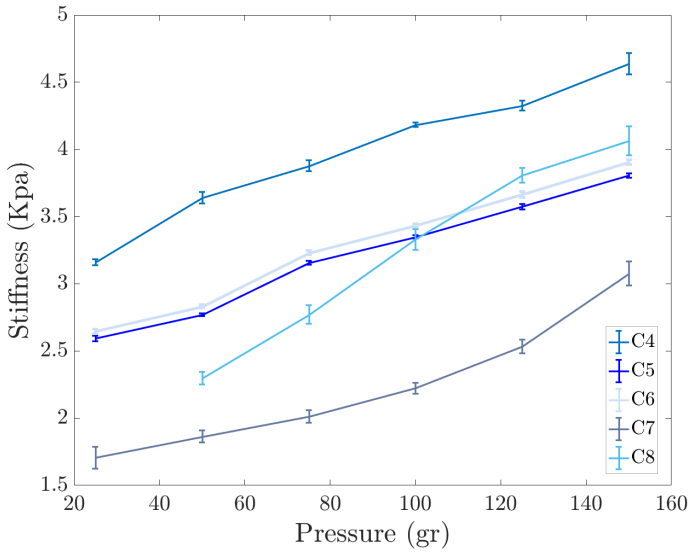

Figure 7.1: Effect of the applied pressure on the stiffness (a pressure ranging from 25 to 150gr was exerted). Measurements were done via TWE on ex vivo cervical samples.

7.1.2.Evidence 2: Harmonic generation

The extreme hyperelasticity that soft tissue exhibits clearly manifests as quantifiable shear wave harmonic generation, and is here hypothesized to depend strongly on the unfolding of its collagen fibres, which again controls the tissue's mechanical functionality and completes the biomarker definition. A tissue mimicking homogeneous hydrogel phantom and a human skin were measured via TWE as shown in Figure 7.2, at 5 cycles a frequency of 800Hz and a range of amplitudes starting from 0.25 to 1 of the maximum capacity of the amplifier.

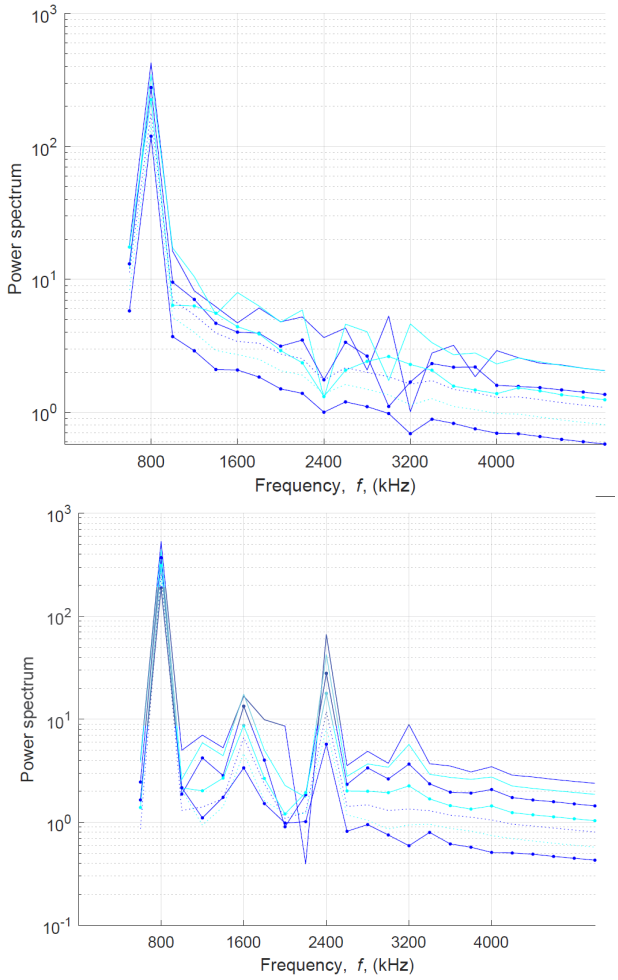

Figure 7.2: The upper figure shows a set of measurements via TWE in a homogeneous phantom while in the bottom figure the TW scan was done to a human skin.

7.2.Materials and Methods

A total of seven hysterectomy specimens from women with benign gynecological conditions were obtained from Health Campus Hospital in Granada (Table 7.1). The study met the principles of the Declaration of Helsinki. Approvals of the Ethical Committee in Human Research of the University of Granada and Ethical Commission and Health Research of Health Campus Hospital in Granada were achieved. All women enrolled in the evaluation

provided agreement by signing a written consent and reading the information of the patient report.

Table 7.1
Obstetric characteristics of the population in the study.

Patient	Age	Hysterectomy Indication
1	53	Vaginal prolapse
2	67	Subserous myoma
3	59	Vaginal prolapse
4	54	Cervical prolapse
5	50	Cervical prolapse
6	51	Cervical prolapse
7	71	Cervical prolapse

7.3.Comparison between Hyperelastic Models

The experimental data of the uniaxial tensile tests for each of the cervical tissue samples are represented as stress–strain curves (Figure 7.3). In these curves, it can be appreciated the three zones that are explained in Figure 7.4: nonlinear, quasi-linear and rupture. The results of the fits of the experimental data with the three hyperelastic models are shown in Tables 7.2–7.4. These fitted curves were performed with MATLAB ® (Release 2018b, MathWorks, Natick, United States) Curve Fitting Toolbox. The median and the confident intervals have been calculated for each parameter. The relationship between woman's age and the Third Order Elastic Constant A from the proposed model, the infinitesimal shear modulus μ_r from the Ogden model, c_1 parameter from the Mooney–Rivlin model, and c_2 parameter from the Mooney–Rivlin model for the connective layer are shown in Figures 7.5–7.8.

An illustrative example of the comparison of the hyperelastic theoretical models with the experimental results obtained from the connective layer of Cervix 2 is shown in Figure 7.9.

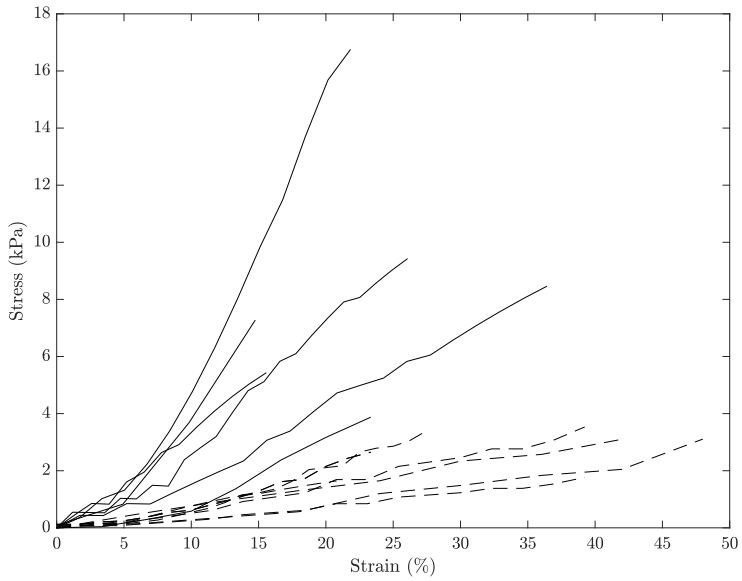

Figure 7.3: Experimental stress-strain relationship for cervical samples tested under uniaxial tensile test. Solid black and discontinue lines represent the connective and layer respectively. The stress is the true stress. Adapted from[2].

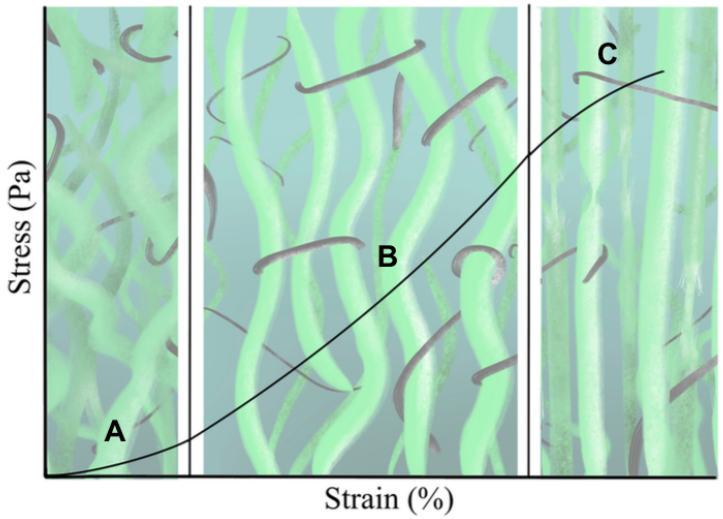

Figure 7.4: Representation of stress–strain behavior of soft tissues. The curve is divided into three zones: nonlinear (**A**), quasi-linear (**B**) and rupture (**C**). The state of elastin (black color) and collagen (green color) is represented at the bottom of each zone. Adapted from[2].

Table 7.2
Results of the fits of experimental data with the proposed nonlinear model. Shear modulus μ and TOEC A in MPa. IQR: Interquartile Range.

	Nonlinear Model			
	Epithelial Layer		**Connective Layer**	
Cervix	μ	A	μ	A
1	1.13	22.6	3.58	3.49
2	1.22	−6.08	4.72	−7.63
3	1.35	−3.06	2.64	−5.92
4	1.57	28.3	3.30	27.6
5	1.35	−2.35	3.51	73.6
6	1.13	2.32	3.49	70.1
7	1.27	30.72	3.96	25.7
Median (IQR)	1.27 (1.13 1.35)	2.32 (−3.06 28.3)	3.51 (3.30 3.96)	25 (−5.92 70.1)

Table 7.3
Results of the fits of the experimental data with the Ogden model. The infinitesimal shear modulus μ_r in MPa. IQR: Interquartile Range.

	Ogden Model			
	Epithelial Layer		**Connective Layer**	
Cervix	μ_r	α_r	μ_r	α_r
1	0.41	7.94	0.941	6.01
2	1.01	1.62	1.16	5.63
3	0.42	4.54	0.97	4.13
4	0.35	9.94	0.85	11.1
5	0.47	4.31	0.82	10.25
6	0.39	5.27	0.57	11.54
7	0.40	9.05	1.29	6.40
Median (IQR)	0.41 (0.39 0.47)	5.27 (4.31 9.05)	0.94 (0.82 1.16)	6.40 (5.63 11.1)

Table 7.4
Results of the fits of the experimental data with the Mooney–Rivlin model. IQR: Interquartile Range.

	Mooney-Rivlin Model			
	Epithelial Layer		**Connective Layer**	
Cervix	c_1	c_2	c_1	c_2
1	6.93	−6.73	5.87	−4.77
2	0.33	−0.08	4.7	−3.15
3	1.22	−0.78	2.51	−1.68
4	8.25	−7.84	59.9	−59.3
5	1.47	−1.05	20.56	−19.67
6	2.35	−2.06	15.7	−15.9
7	8.69	−8.44	12.1	−11.1
Median (IQR)	2.35 (1.22 8.25)	−2.06 (−7.84 −0.78)	12.10 (4.70 20.56)	−11.1 (−19.67 −3.15)

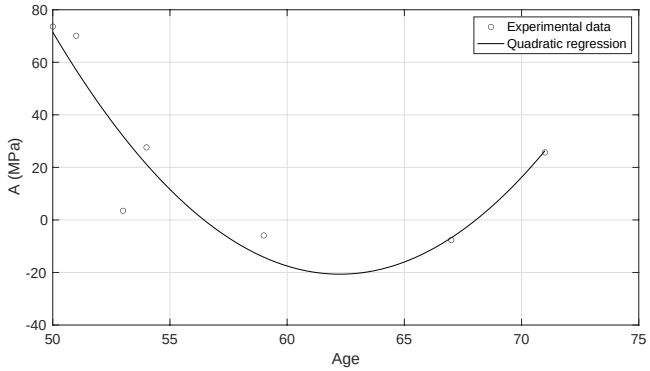

Figure 7.5: Quadratic regression of the Third Order parameter A of the connective layer against the woman's age. $R^2 = 0.84$. Adapted from[2].

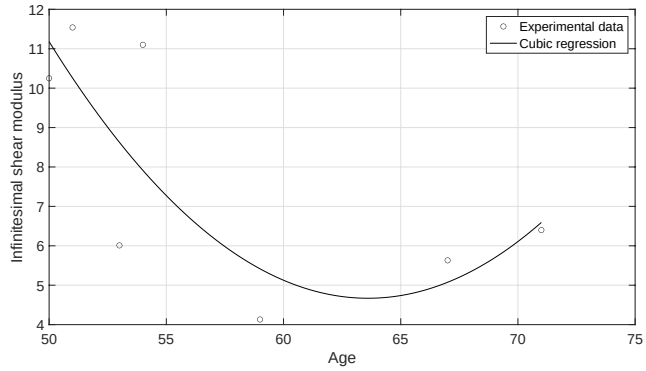

Figure 7.6: Cubic regression of the infinitesimal shear modulus μ_r of the connective layer from the Odgen model against the woman's age. $R^2 = 0.60$. Adapted from[2].

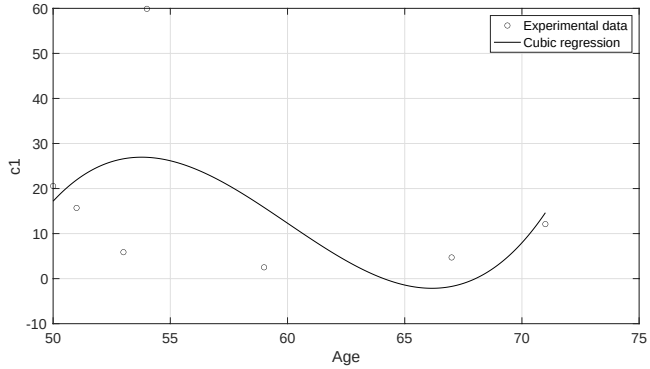

Figure 7.7: Cubic regression of the c_1 parameter of the connective layer from the Mooney–Rivlin model against the woman's age. $R^2 = 0.24$. Adapted from[2].

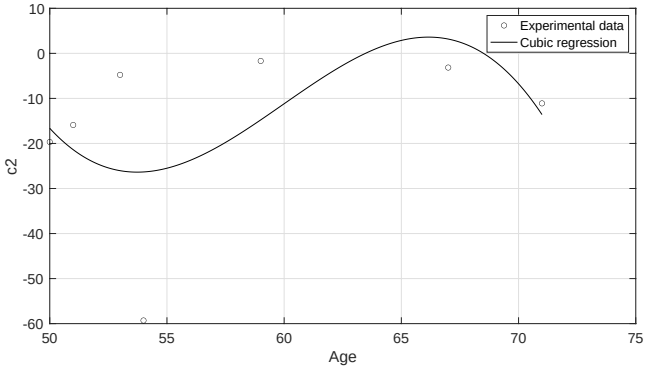

Figure 7.8: Cubic regression of the c_2 parameter of the connective layer from the Mooney–Rivlin model against the woman's age. $R^2 = 0.25$. Adapted from[2].

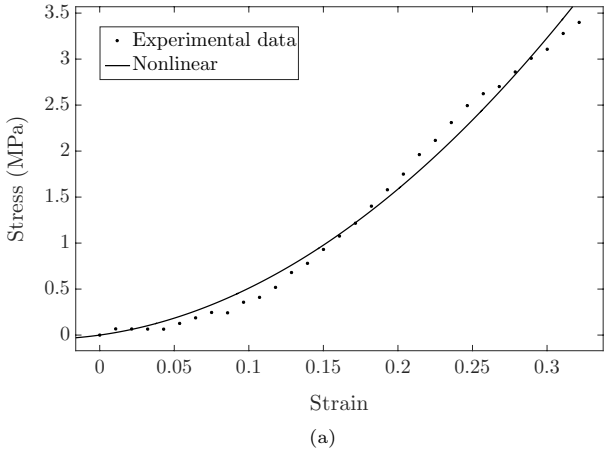

(a)

Figure 7.9: *Cont.*

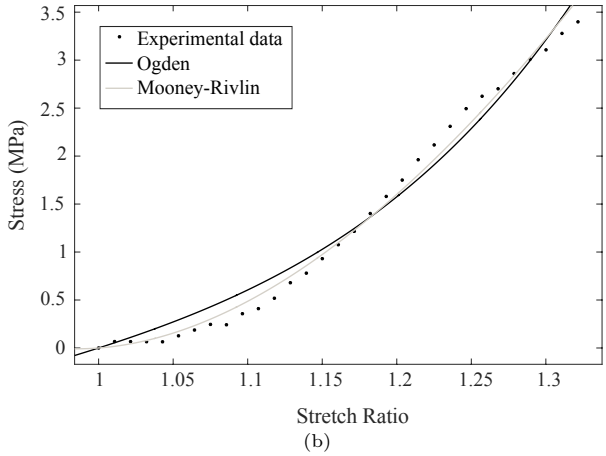

Figure 7.9: Comparison of the hyperelastic theoretical models with the experimental results obtained from the connective layer of Cervix 2. (**a**) The proposed nonlinear Fourth Order Elastic Constant (FOEC) nonlinear model; (**b**) Mooney–Rivlin and Ogden models. Adapted from[2].

7.4.Shear Modulus Estimation

The shear modulus can be obtained directly by means of the μ parameter of the FOEC proposed model, through the slope of the stress–strain curve in the linear region or also trough a combination of the two parameters of the Ogden model, the infinitesimal shear modulus μ_r and the stiffening parameter α_r (see Equation (2.6.19)). Table 7.5 shows the values of the shear modulus for each procedure and for each sample.

Table 7.5
Shear modulus estimation for the proposed nonlinear model, the Ogden model and the slope of the linear region of the stress–strain curve. The mean and standard deviation of the values for the seven samples are presented in MPa.

	Shear Modulus					
	Epithelial Layer			**Connective Layer**		
Cervix	**Nonlinear**	**Ogden**	**Curve**	**Nonlinear**	**Ogden**	**Curve**
1	1.13	1.65	0.82	3.58	2.83	4.17
2	1.22	0.82	0.69	4.72	3.28	3.78
3	1.35	0.95	1.43	2.64	2.01	3.62
4	1.57	1.77	1.82	3.30	4.71	3.26
5	1.35	1.02	0.44	3.51	4.22	5.25
6	1.13	1.03	0.90	3.49	3.30	4.42
7	1.27	1.84	1.08	3.96	4.15	3.17
Mean ± Std	1.29 ± 0.15	1.30 ± 0.43	1.02 ± 0.46	3.60 ± 0.63	3.50 ± 0.92	3.95 ± 0.72

In order to study the differences between the obtained shear modulus with the nonlinear model, Ogden model and the slope of the curve stress-strain for each cervical layer, a Student's t-test was used (see Figure 7.10).

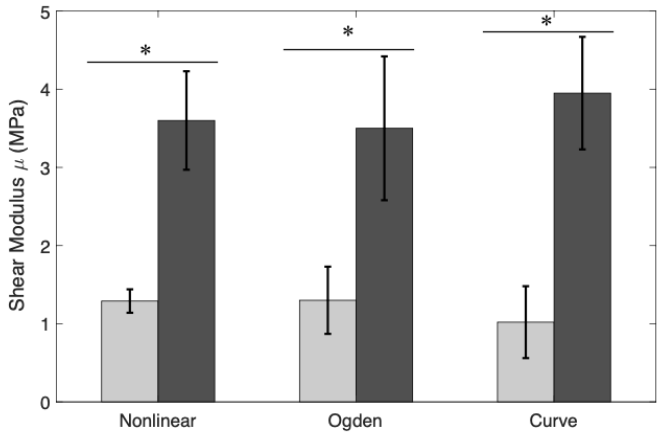

Figure 7.10: Comparison between shear modulus of epithelial and connective layers using the proposed nonlinear model, the Ogden model, and the slope of the linear region of the stress-strain curve. The results are presented as mean ± standard deviation. The light gray bars represent the epithelial layer and the dark gray bars the connective layer. P-value obtained from the Student's t-test was the metric used for this comparison. (* p-value < 0.001). Adapted from[2].

Another parameter that shows significant differences between the epithelial

and the connective layers is the infinitesimal shear modulus. Figure 7.11 shows the mean and deviation values of the infinitesimal stiffness modulus, derived from the Ogden model, for the epithelial and connective layers. The metric used for the comparison was the p-value obtained from the Student's T-test.

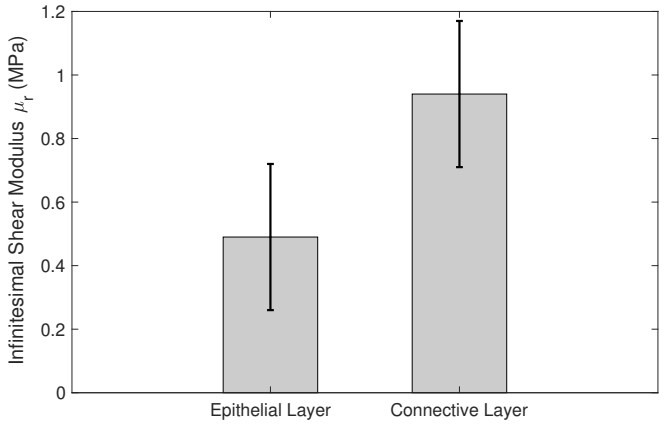

Figure 7.11: Comparison between the infinitesimal shear modulus (μ_r) of epithelial and connective layers using the Ogden model. The results are presented as mean ± standard deviation. P-value obtained from the Student's T-test was the metric used. (* p-value = 0.0016). Adapted from[2].

7.5. Discussion

According to the evidence found in literature, Myers et al. [176] investigated the nonlinear time-dependent stress response of cervical samples from different human hysterectomy specimens. Results showed the nonlinear response of cervical stroma, which was dependent on obstetric history. However, to our knowledge, the nonlinear elastic properties of ex vivo human cervical tissue, using the aforementioned hyperelastic models, have not been obtained by uniaxial tensile tests yet.

This work aims at representing a first step toward a nonlinear characterization of human cervical tissue. The nonlinear elastic properties of ex vivo cervical tissue have been obtained for the first time by uniaxial tensile tests.

The first contribution of this study is to propose a new hyperelastic model (nonlinear model) based on the FOEC in the sense of Landau's theory [311]

and compare the obtained results with the most used hyperelastic models in the literature, Mooney–Rivlin, and Ogden models [194, 196].

As a second contribution, the differences in shear modulus between epithelial and connective layers of ex vivo human cervical tissue are analyzed. The TWE technique proposed in the literature aims to locally measure the mechanical parameters of the cervix that can be correlated with the different stages of the cervix maturing during pregnancy [134]. These waves interact not only with the superficial layer, the epithelial layer, but also with the deeper layers, i.e., connective layer. Therefore, a validation of the mechanical parameters reconstructed in both layers is necessary through uniaxial tensile tests of ex vivo samples from hysterectomies of healthy women.

The mechanical behavior of the cervix is nonlinear, as are most of the soft biological tissues. The nonlinear parameters of the FOEC proposed model were obtained through a fit of the experimental data measured in the uniaxial tensile tests with the theoretical law that governs the hyperelastic model. The same procedure was carried out in order to get the nonlinear parameters from the two most employed hyperelastic models to characterize soft biological tissue in the literature, Mooney–Rivlin and Ogden models.

The proposed FOEC hyperelastic model, Equation 2.6.9, presents three parameters, the shear modulus μ, the third order elastic constant A and the fourth order elastic constant D. In this study, the proposed theoretical stress-strain relationship has been simplified with the aim of comparing with the two-term Mooney–Rivlin and Ogden models. The two parameters that have adjusted the experimental data were the shear modulus μ and the third order elastic constant A. Analyzing the results of the shear modulus, there was no significant variation in both, the epithelial 1.29 ± 0.15 MPa and the connective layer 3.60 ± 0.63 MPa for each of the hysterectomy samples, see Table 7.5. The values of the shear stiffness are highly dependent on the strain ramp rate used, the larger strain rate, the larger shear modulus [312, 313]. The values obtained for cervical tissue agree with those found in the literature [170, 176]. However, regarding the nonlinear parameter A, large variation was observed, varying the parameter from positive to negative values (see Table 7.2). Previous studies in the literature have obtained the value of parameter A in tissue-mimicking phantoms and breast tissue [314, 315]. Gennisson et al. [314] investigated the nonlinear behavior of quasi-incompressible agar-gelatin-based phantoms using supersonic shear imaging technique. The study concluded that, for different samples of tissue-mimicking phantoms, the value of parameter A varied from a negative value to a positive one. Similar results were obtained by Bernal et al. [315] in

breast tissue, parameter A presents high variability due to internal changes in tissue consistency. According to the present study, it is worth pointing out that, to our knowledge, this is the first work that studies the nonlinear parameters of the FOEC hyperelastic model in cervical tissue. The variability found in the third elastic constant parameter A could be associated with the heterogeneity of the tissue, like the two previous studies [250], also depends on the particular epidemiological aspect of each patient, as reported by Myers et al. [25]. Despite the variability of parameter A, and the low number of samples, the quadratic regression studied in the connective tissue samples showed a high correlation with women's age ($R^2 = 0.84$) (Figure 7.5). On the other hand, the cubic regressions in the connective layer of the infinitesimal shear modulus μ_r from the Ogden model, the c_1 parameter from the Mooney–Rivlin model, and the c_2 parameter from the Mooney–Rivlin model against the women's age have smaller correlations, Figures 7.6–7.8 ($R^2 = 0.60$, $R^2 = 0.24$, and $R^2 = 0.25$ respectively). This result is very preliminary because only seven samples have been considered, so future studies to explore other relationships with physiological markers require a greater number of patients, despite the difficulty of obtaining ex vivo samples.

On the one hand, the shear modulus is one of the most used parameters in the characterization of soft biological tissues by various techniques. This value can be extracted directly by means of the μ parameter of the FOEC proposed model, through the slope of the stress–strain curve in the linear region or also through a combination of the two parameters of the Ogden model, the infinitesimal shear modulus μ_r and the stiffening parameter α_r. The values of the shear modulus for each reconstruction technique and for each sample are shown in Table 7.5. The parameters that govern the Mooney–Rivlin model have no physical sense and, therefore, the shear modulus value can not be extracted from them. The results of the shear modulus for each reconstruction technique and for each cervical layers were compared by using a Student's t-test. t-test results are shown in Figure 7.10, in terms of p-values. All of these values were below 0.001, which can be considered to represent a significant difference in the shear modulus between the epithelial and connective layers. In conclusion, the shear modulus was dependent on the anatomical location of the cervical tissue as shown in Table 7.5 and Figure 7.10. On the other hand, the infinitesimal shear modulus (μ_r) is one of the parameters that governs the hyperelastic Ogden model. The p-value obtained for the comparison between the epithelial and connective layers (p-value = 0.0016) shows that there is a significant difference (see Figure 7.11), therefore, this parameter could also indicate differences in stiffness for both layers.

In general, by the obtained results, it can be concluded that the nonlinear parameter A could be an important biomarker in the characterization of connective cervical tissue. In addition, the calculated shear modulus depended on the anatomical location of the cervical tissue. The protocol of measurements is applicable to other tissues and it is possible to explore a set of new nonlinear measurements from different procedures, for example in vivo measurements in women using ultrasound wave propagation by employing Hamilton's formulation, one step further from the diagnostic point of view.

7.6.Conclusions

In this chapter, as a first contribution, we proposed a new hyperelastic model (nonlinear model) based on the Fourth Order Elastic Constants (FOECs) in the sense of Landau's theory to reconstruct the nonlinear parameters in cervical tissue by fitting the experimental data with this model. The experimetal data were also fitted by the most used hyperelastic models in the literature, Mooney–Rivlin, and Ogden. The nonlinear parameter A from the proposed model could be an important biomarker in connective cervical tissue diagnosis. As a second contribution, a comparison of the shear modulus, extracted from three different procedures, between the epithelial and connective layers of ex vivo cervical tissue was performed. The conclusion is that shear modulus was dependent on anatomical location of the cervical tissue. Despite the difficulties encountered in the characterization of the hyperelastic behaviour of cervical tissue, the proposed nonlinear model should be considered as the basis of more complex constitutive equations. Nevertheless, the nonlinear FOEC model should remain as the starting point in the hyperelastic characterization of the cervical tissue in future studies.

Part IV

CONCLUSIONS AND FUTURE WORKS

I was taught that the way of progress is neither swift nor easy.

Marie Curie

Chapter8

Discussion and conclusions

In perspective, the purpose of this dissertation is to manifest ground and clinical evidence that goes a little step beyond linear elasticity. Abnormalities in the viscosity and nonlinearity of soft tissues are intimately linked to a broad range of pathologies including labour disorders, solid tumours, atherosclerosis, liver fibrosis, and osteoarticular syndromes, just to name but a few. This suggests that it is crucial to rethink where we are in terms of soft tissue mechanics and how pathologies affect them, opening a timely opportunity of moving forward defining new mechanical biomarkers, enabling earlier more specific and precise diagnostic and therapeutic decision making.

On the one hand, viscoelasticity, or more generally, tissue rheology or dynamic dispersion, is recognized from the physics of wave propagation as a compound expression of the rheological, poroelastic, and microstructural scattering phenomena governed by the complex fibrous multiscale microstructure of the stroma, which mainly stems from the interaction of collagen and elastin with the viscous proteoglycans, which undergo characteristic changes during pathologies.

On the other hand, the significant hyperelasticity that soft tissues exhibit can manifest itself as quantifiable shear wave harmonic generation. One of the main hypotheses about the pathology-mediated origin of nonlinearity changes is the crimping crosslinking of tissue fibres. In the same manner that shear waves have recently been believed far more sensitive to tissue classification than standard compressional waves but are troublesome to quantify, some experimental observation may tangentially suggest nonlinear mechanical properties may be a key signature to quantify and classify and diagnose a range of soft tissue pathologies.

For instance, within the field of labour disorders, despite the decrimping of fibres along gestation and the inflammatory process, it is suggested a strong diagnostic potential of those biomarkers. Nonetheless, no attempts to measure viscoelastic and nonlinear parameters using elastography as biomarkers have been reported in the literature, which opens a promising research field. Viscosity measurement with ultrasonic techniques is currently less extended

than by MR techniques, but this shortcoming is only attributable to the immaturity of the ultrasonic technique. Thus, barriers to its future potential are foreseen.

In conclusion, several front lines have been exposed, yet many other questions call for a response. For instance, how will the ultrasound elastography industry develop techniques considering these biomarkers to adapt them to an actual application? Quantitative answers to these questions would improve many clinical protocols.

Objective 1: Tissue viscoelasticity

The objective of this chapter was to validate the (TWE) technique against Shear Wave Elasticity Imaging (SWEI) technique through the determination of shear wave velocity, shear moduli, and viscosity of ex vivo chicken liver samples, tissue-mimicking hydrogel phantoms and ex vivo human uterine cervices. Preliminary results show that the proposed technique successfully reconstructs shear wave velocity, shear moduli, and viscosity mechanical biomarkers from the propagated torsional wave, establishing a proof of principle and warranting further studies.
TWE presents these advantages:

- Being able to reduce and isolate the spurious waves contamination (P-waves)
- In small cylindrical organs, like uterine cervix, SWE would generate bounces on the tissue walls and mask the signal received by the receiver. However, in the TWE technique little energy is generated that does not generate rebounds
- TWE technique deposit extremely low energy in the tissue which makes it exceptionally safe. When the acoustic waves are used for fetal imaging, three parameters should be evaluated for safety considerations.

Objective 2: TWE in bounded media

In this section, and for the first time, torsional waves were used as the source of excitation for elastography measurements in corneal (thin-layer) tissue. Corneas were subjected to chemical treatment to modify their mechanical behaviour. An empirical expression was used to calculate the phase speed of A0 Lamb waves from the estimated group speed, through which the modulus of elasticity was obtained, and the dispersion curve was fitted to a Kelvin-Voigt rheological model. The trends of measured elasticity values agreed with tensile test results and literature reports, being TWE able to

differentiate substantial changes. Shear elasticity was within the range of thin-layer tissues, whereas shear viscosity has not been reported after the used empirical Lamb wave expression. The management of corneal surgery and treatments should not solely depend on complex models of geometry and topographical parameters but also rely on quantifiable mechanical parameters that improve diagnostic sensitivity, changing from generalized empirical-based models to customized approaches. Future studies should implement a suitable Lamb wave model and prove the feasibility of using TWE with in vivo animal studies combined with standard equipment.

Objective 3: TWE for anisotropic media

The preliminary results are promising; From the results tabulated in chapter 6, one can observe the difference in the stiffness values obtained from the three sectors of the torsional wave probe, that is, parallel to the fibre orientation of the breast fibres, returns higher values of stiffness as expected. Results are encouraging; the anisotropic probe has been shown to be able to capture the tissue variability concerning the fibre orientation and frequency with a tendency close enough to the gold standard in elastography. Therefore, this new technology can be considered as a baseline for future studies on TWE.

Objective 4: Non-linear shear elasticity

In this chapter, as a first contribution, we proposed a new hyperelastic model (nonlinear model) based on the Fourth Order Elastic Constants (FOECs) in the sense of Landau's theory to reconstruct the nonlinear parameters in cervical tissue by fitting the experimental data with this model. The experimental data were also fitted by the most used hyperelastic models in the literature, Mooney–Rivlin, and Ogden. The nonlinear parameter A from the proposed model could be an important biomarker in connective cervical tissue diagnosis. As a second contribution, a comparison of the shear modulus, extracted from three different procedures, between the epithelial and connective layers of ex vivo cervical tissue was performed. The conclusion is that the shear modulus was dependent on the anatomical location of the cervical tissue. Despite the difficulties encountered in the characterization of the hyperelastic behaviour of cervical tissue, the proposed nonlinear model should be considered the basis of more complex constitutive equations. Nevertheless, the nonlinear FOEC model should remain the starting point in the hyperelastic characterization of the cervical tissue in future studies.

"One never notices what has been done; one can only see what remains to be done."

Marie Curie

Chapter9

Limitations and directions for the future

Limitations

- Anisotropy has the potential to be a significant biomarker, and a large number of reasons come to our mind to support this. However, let's point out one potential limitation to further make it independent of this work: there is a practical operational limitation of quantifying anisotropy using current equipment: the geometrical alignment of the probe, or more specifically the wavefront with the preferential fibres is a non-trivial task that involves strong variabilities and uncertainties in clinical practice.
- Torsional Wave Elastography (TWE) propagates both radially and in depth, the propagation path along the surface reaches the receiver first, because this represents the shortest distance in some cases. In other cases, if the tissue has two well distinguished layers (for example human uterine cervix) were the second one is stiffer than the superficial one, and since torsional waves travel faster trough stiffer layers the propagation pattern will be different.
- The values presented by TWE were an average of global mechanical properties that translated into a fast reconstruction method, taking less than 7 seconds to calculate the group speed. In contrast to other techniques, where a map was reconstructed, no analysis artifacts were detected, such as diffraction or attenuation. However, some limitations of the current method need to be detailed. The TOF algorithm used only calculates the group speed, then, for further analysis, supplementary expressions were required, where the significant dispersion and phase speed of waves were not directly considered.
- Boundary conditions like stress distribution generated by IOP confer a preloaded state, which could be modified if there is direct contact, biasing the results. TWE likely missed focal abnormalities since no 2D

image was obtained.

Future work

Future short-term work will explore new corneal and anisotropy sensor designs, with dimensions adapted to different types of samples. The ethical committee has been requested to perform in vivo measurements on the corneas of sedated animals. With these tests, we will explore the viability of the anisotropic sensor in vivo. Another of the lines started is to investigate the non-linearity of the cervix more deeply by sampling at different amplitudes and cycles and locating the harmonics and the adjustment with a numerical model. I will explore the possible relationship between the fractional alpha of fractional viscoelastic models and tissue vascularization (or fractality) within the coming months.

Bibliography

[1] Jorge Torres, Inas Faris, and Antonio Callejas. Histobiomechanical remodeling of the cervix during pregnancy: Proposed framework. *Mathematical Problems in Engineering*, 2019, 2019.

[2] Antonio Callejas, Juan Melchor, Inas H Faris, and Guillermo Rus. Hyperelastic ex vivo cervical tissue mechanical characterization. *Sensors*, 20(16):4362, 2020.

[3] Inas H Faris, Juan Melchor, Antonio Callejas, Jorge Torres, and Guillermo Rus. Viscoelastic biomarkers of ex vivo liver samples via torsional wave elastography. *Diagnostics*, 10(2):111, 2020.

[4] Gerhard A Holzapfel et al. Biomechanics of soft tissue. *The handbook of materials behavior models*, 3:1049–1063, 2001.

[5] Jay D Humphrey. Continuum biomechanics of soft biological tissues. *Proceedings of the Royal Society of London. Series A: Mathematical, Physical and Engineering Sciences*, 459(2029):3–46, 2003.

[6] Joy Y Vink, Sisi Qin, Clifton O Brock, Noelia M Zork, Feltovich Helen M, Xiaowei Chen, Urie Paul, Kristin M Myers, Timothy J Hall, Ronald Wapner, et al. A new paradigm for the role of smooth muscle cells in the human cervix. *American journal of obstetrics and gynecology*, 215(4):478–e1, 2016.

[7] Yoshida Kyoko, Mala Mahendroo, Joy Vink, Ronald Wapner, and Kristin Myers. Material properties of mouse cervical tissue in normal gestation. *Acta Biomaterialia*, 36:195–209, may 2016.

[8] Susan Tucker. Blackburn. *Parturition and uterine physiology. Maternal, fetal, & neonatal physiology : a clinical perspective.* Elsevier Saunders, 2013.

[9] Albert Singer and Joseph A. Jordan. The Functional Anatomy of the Cervix, the Cervical Epithelium and the Stroma (2009). In *The Cervix*, pages 13–37. Blackwell Publishing Ltd., Oxford, UK.

[10] Lorie M. Harper, Aaron B. Caughey, Anthony O. Odibo, Kimberly A. Roehl, Qiuhong Zhao, and Alison G. Cahill. Normal Progress of Induced Labor. *Obstetrics & Gynecology*, 119(6):1113–1118, jun 2012.

[11] Lindsey C Carlson, Stephanie T Romero, Palmeri Mark L, A Muñoz del Rio, Sean M Esplin, Rotemberg Veronica M, Timothy J Hall, and Feltovich Helen. Changes in shear wave speed pre-and post-induction of labor: a feasibility study. *Ultrasound in Obstetrics & Gynecology*, 46(1):93–98, 2015.

[12] Tristan Gauthier, Sophie Mazeau, François Dalmay, Eyraud Jean-Luc, Cyril Catalan, Benoit Marin, and Aubard Yves. Obesity and cervical ripening failure risk. *The Journal of Maternal-Fetal & Neonatal Medicine*, 25(3):304–307, mar 2012.

[13] Jacob R. Lassiter, Nicolette Holliday, David F. Lewis, Madhuri Mulekar, Abshire Jacob, and Brian Brocato. Induction of labor with an unfavorable cervix: how does BMI affect success? *The Journal of Maternal-Fetal & Neonatal Medicine*, pages 1–3, nov 2015.

[14] Read Charles P, Word R Ann, Monika A Ruscheinsky, Brenda C Timmons, and Mala S Mahendroo. Cervical remodeling during pregnancy and parturition: molecular characterization of the softening phase in mice. *Reproduction*, 134(2):327–340, aug 2007.

[15] S Y Yu, Tozzi C A, J Babiarz, and P C Leppert. Collagen changes in rat cervix in pregnancy–polarized light microscopic and electron microscopic studies. *Proceedings of the Society for Experimental Biology and Medicine. Society for Experimental Biology and Medicine (New York, N.Y.)*, 209(4):360–8, sep 1995.

[16] F G Cunningham, N F Gant, K J Leveno, L C Gilstrap 3rd, Hauth J C, and K D Wenstrom. General considerations and maternal evaluation. *Williams obstetrics*, pages 912–925, 2010.

[17] Cameron G. Barclay, Brennand Janet E., Rodney W. Kelly, and Andrew A. Galder. Interleukin-8 production by the human cervix. *American Journal of Obstetrics and Gynecology*, 169(3):625–632, sep 1993.

[18] E. El Maradny, Kanayama N., Kobayashi H., B. Hossain, S. Khatun, Liping S., Kobayashi T., and T. Terao. The role of hyaluronic acid as a mediator and regulator of cervical ripening. *Human Reproduction*, 12(5):1080–1088, may 1997.

[19] Mikitaka Obara, Hideto Hirano, Masaki Ogawa, Tsubaki Hiromitsu, Hosoya Naoko, Yoshida Yuko, Miyauchi Satoshi, and Tanaka Toshinobu. Changes in molecular weight of hyaluronan and hyaluronidase activity in uterine cervical mucus in cervical ripening. *Acta Obstetricia et Gynecologica Scandinavica*, 80(6):492–496, jan 2001.

[20] Catherine L Elliott, Brennand Janet E, and Andrew A Calder. The effects of mifepristone on cervical ripening and labor induction in primigravidae. *Obstetrics & Gynecology*, 92(5):804–809, nov 1998.

[21] Word R, Li Xiang-Hong, Michael Hnat, and Kelley Carrick. Dynamics of Cervical Remodeling during Pregnancy and Parturition: Mechanisms and Current Concepts. *Seminars in Reproductive Medicine*, 25(1):069–079, jan 2007.

[22] S. M. Yellon, A. M. Mackler, and M. A. Kirby. The Role of Leukocyte Traffic and Activation in Parturition. *Journal of the Society for Gynecologic Investigation*, 10(6):323–338, sep 2003.

[23] Kristin M. Myers, Feltovich Helen, Mazza Edoardo, Joy Vink, Bajka Michael, Ronald J. Wapner, Timothy J. Hall, and House Michael. The mechanical role of the cervix in pregnancy. *Journal of Biomechanics*, 48(9):1511–1523, jun 2015.

[24] Wang Yao, Yu Gan, Kristin M. Myers, Joy Y. Vink, Ronald J. Wapner, and Christine P. Hendon. Collagen Fiber Orientation and Dispersion in the Upper Cervix of Non-Pregnant and Pregnant Women. *PLOS ONE*, 11(11):e0166709, nov 2016.

[25] Kristin M Myers, Feltovich Helen, Mazza Edoardo, Joy Vink, Bajka Michael, Ronald J Wapner, Timothy J Hall, and House Michael. The mechanical role of the cervix in pregnancy. *Journal of biomechanics*, 48(9):1511–1523, 2015.

[26] V Dubrauszky. Further observations on the structure of the uterine wall during pregnancy]. *Archiv fur Gynakologie*, 202:41–3, 1965.

[27] House Michael, Bhadelia Rafeeque A., Kristin Myers, and Socrate Simona. Magnetic resonance imaging of three-dimensional cervical anatomy in the second and third trimester. *European Journal of Obstetrics & Gynecology and Reproductive Biology*, 144:S65–S69, may 2009.

[28] P C Leppert. Anatomy and physiology of cervical ripening. *Clinical obstetrics and gynecology*, 38(2):267–79, jun 1995.

[29] Ivan M Rosado-Mendez, Palmeri Mark L, Lindsey C Drehfal, Quinton W Guerrero, Heather Simmons, Feltovich Helen, and Timothy J Hall. Assessment of structural heterogeneity and viscosity in the cervix using shear wave elasticity imaging: initial results from a rhesus macaque model. *Ultrasound in medicine & biology*, 43(4):790–803, 2017.

[30] Wang Yao, Yoshida Kyoko, Michael Fernandez, Joy Vink, Ronald J Wapner, Ananth Cande V, Michelle L Oyen, and Kristin M Myers. Measuring the compressive viscoelastic mechanical properties of human cervical tissue using indentation. *Journal of the mechanical behavior of biomedical materials*, 34:18–26, 2014.

[31] Andrea R. Westervelt, Michael Fernandez, House Michael, Joy Vink, Nhan-Chang Chia-Ling, Ronald Wapner, and Kristin M. Myers. A Parameterized Ultrasound-Based Finite Element Analysis of the Mechanical Environment of Pregnancy. *Journal of Biomechanical Engineering*, 139(5):051004, apr 2017.

[32] M. Fernandez, House M., S. Jambawalikar, N. Zork, J. Vink, R. Wapner, and K. Myers. Investigating the mechanical function of the cervix during pregnancy using finite element models derived from high-resolution 3D MRI. *Computer Methods in Biomechanics and Biomedical Engineering*, 19(4):404–417, mar 2016.

[33] K J Parker, M M Doyley, and D J Rubens. Corrigendum: Imaging the elastic properties of tissue: the 20 year perspective. *Physics in Medicine and Biology*, 2012.

[34] J Ophir, I Ccspedes, Ponnekanti H, Yazdi Y, and Li X. ELASTOGRAPHY A QUANTITATIVE METHOD FOR IMAGING THE ELASTICITY OF BIOLOGICAL TISSUES. Technical report, 1991.

[35] Venkatesh Sudhakar K., Meng Yin, and Richard L. Ehman. Magnetic resonance elastography of liver: Technique, analysis, and clinical applications. *Journal of Magnetic Resonance Imaging*, 37(3):544–555, 2013.

[36] Lamiaa Mobarak, Mohammed M. Nabeel, Ehsan Hassan, Dalia Omran, and Zakaria Zeinab. Real-time elastography as a noninvasive assessment of liver fibrosis in chronic hepatitis C Egyptian patients: A prospective study. *Annals of Gastroenterology*, 2016.

[37] A. Thomas. Imaging of the cervix using sonoelastography. *Ultrasound in Obstetrics and Gynecology*, 2006.

[38] Anke Thomas, Sherko Kümmel, Ole Gemeinhardt, and Thomas Fischer. Real-Time Sonoelastography of the Cervix: Tissue Elasticity of the Normal and Abnormal Cervix. *Academic Radiology*, 2007.

[39] Molina FS, Gómez LF, Florido J, Padilla MC, and Nicolaides KH. Quantification of cervical elastography: a reproducibility study. *Ultrasound in Obstetrics & Gynecology*, 39(6):685–689, 2012.

[40] Hernandez-Andrade E., S. S. Hassan, H. Ahn, Korzeniewski S. J., L. Yeo, Chaiworapongsa T., and R. Romero. Evaluation of cervical stiffness during pregnancy using semiquantitative ultrasound elastography. *Ultrasound in Obstetrics and Gynecology*, 2013.

[41] Feltovich H. and T. J. Hall. Quantitative imaging of the cervix: setting the bar. *Ultrasound in Obstetrics & Gynecology*, 41(2):121–128, feb 2013.

[42] M. M. Maurer, S. Badir, Pensalfini M., Bajka M., Abitabile P., R. Zimmermann, and Mazza E. Challenging the in-vivo assessment of biomechanical properties of the uterine cervix: A critical analysis of ultrasound based quasi-static procedures. *Journal of Biomechanics*, 2015.

[43] A. Fruscalzo, R. Schmitz, Klockenbusch W., and Steinhard J. Reliability of cervix elastography in the late first and second trimester of pregnancy. *Ultraschall in der Medizin*, 2012.

[44] Hee Lene, Puk Sandager, Olav Petersen, and Uldbjerg Niels. Quantitative sonoelastography of the uterine cervix by interposition of a synthetic reference material. *Acta Obstetricia et Gynecologica Scandinavica*, 2013.

[45] Arrigo Fruscalzo, Ambrogio P. Londero, and Ralf Schmitz. Quantitative cervical elastography during pregnancy: influence of setting features on strain calculation. *Journal of Medical Ultrasonics*, 2015.

[46] A. Fruscalzo, A. P. Londero, Fröhlich C., U. Möllmann, and R. Schmitz. Quantitative elastography for cervical stiffness assessment during pregnancy. *BioMed Research International*, 2014.

[47] A. Fruscalzo, R. Schmitz, Klockenbusch W., and Steinhard J. Reliability of cervix elastography in the late first and second trimester of pregnancy. *Ultraschall in der Medizin*, 2012.

[48] Mazza Edoardo, Parra-Saavedra Miguel, Bajka Michael, Eduard Gratacos, Kypros Nicolaides, and Jan Deprest. In vivo assessment of the biomechanical properties of the uterine cervix in pregnancy. *Prenatal Diagnosis*, 34(1):33–41, jan 2014.

[49] Arrigo Fruscalzo, Mazza Edoardo, Feltovich Helen, and Ralf Schmitz. Cervical elastography during pregnancy: a critical review of current approaches with a focus on controversies and limitations. *Journal of Medical Ultrasonics*, 43(4):493–504, oct 2016.

[50] Robert M. Lerner, Huang S. R., and Kevin J. Parker. "Sonoelasticity" images derived from ultrasound signals in mechanically vibrated tissues. *Ultrasound in Medicine and Biology*, 1990.

[51] Mostafa Fatemi and James F. Greenleaf. Ultrasound-stimulated vibroacoustic spectrography. *Science*, 280 5360:82–5, 1998.

[52] Laurent Sandrin, Mickaël Tanter, Catheline Stefan, and Mathias Fink. Shear modulus imaging with 2-d transient elastography. *IEEE transactions on ultrasonics, ferroelectrics, and frequency control*, 49(4):426–435, 2002.

[53] Brian J. Fahey, Kathryn Nightingale, R. C. Nelson, Mark L. Palmeri, and Gregg E. Trahey. Acoustic radiation force impulse imaging of the abdomen: demonstration of feasibility and utility. *Ultrasound in medicine & biology*, 31 9:1185–98, 2005.

[54] Kathryn Nightingale, Mark L. Palmeri, Roger W. Nightingale, and Gregg E. Trahey. On the feasibility of remote palpation using acoustic radiation force. *The Journal of the Acoustical Society of America*, 110 1:625–34, 2001.

[55] G. R. Torr. The acoustic radiation force. *American Journal of Physics*, 52(5):402–408, 1984.

[56] Wei Meng, Guangchen Zhang, Changjun Wu, Guozhu Wu, Yan Song, and Zhaoling Lu. Preliminary results of acoustic radiation force impulse (arfi) ultrasound imaging of breast lesions. *Ultrasound in medicine & biology*, 37 9:1436–43, 2011.

[57] Zhai Liang, John Madden, Wen-Chi Foo, Palmeri Mark L, Vladimir Mouraviev, Thomas J Polascik, and Nightingale Kathryn R. Acoustic radiation force impulse imaging of human prostates ex vivo. *Ultrasound Med. Biol.*, 36(4):576–588, 2010.

[58] Kathryn Nightingale, Stephen A. McAleavey, and Gregg E. Trahey. Shear-wave generation using acoustic radiation force: in vivo and ex vivo results. *Ultrasound in medicine & biology*, 29 12:1715–23, 2003.

[59] Jeffrey Bamber, Cosgrove D, Dietrich CF, J Fromageau, Bojunga J, Calliada F, Cantisani V, J-M Correas, M Donofrio, Drakonaki EE, et al. Efsumb guidelines and recommendations on the clinical use of ultrasound elastography. part 1: Basic principles and technology. *Ultraschall in der Medizin-European Journal of Ultrasound*, 34(02):169–184, 2013.

[60] Bercoff Jérémy, Mickael Tanter, and Mathias Fink. Supersonic shear imaging: a new technique for soft tissue elasticity mapping. *IEEE transactions on ultrasonics, ferroelectrics, and frequency control*, 51(4):396–409, 2004.

[61] J-L Gennisson, Thomas Deffieux, Mathias Fink, and Michaël Tanter. Ultrasound elastography: principles and techniques. *Diagnostic and interventional imaging*, 94(5):487–495, 2013.

[62] Armen P Sarvazyan, Oleg V Rudenko, Scott D Swanson, J.Brian Fowlkes, and Stanislav Y Emelianov. Shear wave elasticity imaging: a new ultrasonic technology of medical diagnostics. *Ultrasound in medicine & biology*, 24(9):1419 – 1435, 1998.

[63] Nightingale Kathryn, Palmeri Mark, and Gregg Trahey. Analysis of contrast in images generated with transient acoustic radiation force. *Ultrasound in Medicine and Biology*, 2006.

[64] Lindsey C. Carlson, Feltovich Helen, Palmeri Mark L., Alejandro Muñoz Del Rio, and Timothy J. Hall. Statistical analysis of shear wave speed in the uterine cervix. *IEEE Transactions on Ultrasonics, Ferroelectrics, and Frequency Control*, 2014.

[65] Lindsey C. Carlson, Helen Feltovich, Mark L. Palmeri, Jeremy J. Dahl, Alejandro Munoz del Rio, and Timothy J. Hall. Shear wave speed estimation in the human uterine cervix. *Ultrasound Obstet Gynecol*, 43:452–458, 2014.

[66] Marie Muller, Dora Aït-Belkacem, Hessabi Mahdieh, Jean-Luc Gennisson, Gilles Grangé, François Goffinet, Edouard Lecarpentier, Dominique Cabrol, Mickaël Tanter, and Vassilis Tsatsaris. Assessment of the cervix in pregnant women using shear wave elastography: a feasibility study. *Ultrasound in medicine & biology*, 41(11):2789–2797, 2015.

[67] Hernandez-Andrade Edgar, Alma Aurioles-Garibay, Garcia Maynor, Korzeniewski Steven J., Alyse G. Schwartz, Hyunyoung Ahn, Martinez-Varea Alicia, Lami Yeo, Chaiworapongsa Tinnakorn, Sonia S. Hassan, and Roberto Romero. Effect of depth on shear-wave elastography estimated in the internal and external cervical os during pregnancy. *Journal of Perinatal Medicine*, 2014.

[68] Lindsey C. Carlson, Timothy J. Hall, Ivan M. Rosado-Mendez, Mark L. Palmeri, and Helen Marcie Feltovich. Detection of changes in cervical softness using shear wave speed in early versus late pregnancy: An in vivo cross-sectional study. *Ultrasound in medicine & biology*, 44 3:515–521, 2017.

[69] Peralta L., G. Rus, Bochud N., and Molina F.S. Assessing viscoelasticity of shear wave propagation in cervical tissue by multiscale computational simulation. *Journal of Biomechanics*, 48(9):1549–1556, jun 2015.

[70] Hernandez-Andrade et al. Effect of depth on shear-wave elastography estimated in the internal and external cervical os during pregnancy. *J Perinat Med.*, 42(5):549–557, 2014.

[71] Marie Muller, Dora Aït-Belkacem, Mahdieh Hessabi, Jean luc Gennisson, Gilles Grange, F. Goffinet, Edouard R Lecarpentier, Dominique Cabrol, Mickaël Tanter, and Vassilis Tsatsaris. Assessment of the cervix in pregnant women using shear wave elastography: A feasibility study. *Ultrasound in medicine & biology*, 41 11:2789–97, 2015.

[72] Ivan M Rosado-Mendez, Lindsey C Carlson, Kaitlin M Woo, Andrew P Santoso, Quinton W Guerrero, Palmeri Mark L, Feltovich Helen, and Timothy J Hall. Quantitative assessment of cervical softening during pregnancy in the rhesus macaque with shear wave elasticity imaging. *Physics in Medicine & Biology*, 63(8):085016, 2018.

[73] M Fernandez, House M, S Jambawalikar, N Zork, J Vink, R Wapner, and K Myers. Investigating the mechanical function of the cervix during pregnancy using finite element models derived from high-resolution 3d mri. *Computer methods in biomechanics and biomedical engineering*, 19(4):404–417, 2016.

[74] K.M. Myers, Paskaleva A.P., House M., and Socrate S. Mechanical and biochemical properties of human cervical tissue. *Acta Biomaterialia*, 4(1):104–116, jan 2008.

[75] Blackburn Brecken J, Jenkins Michael W, Rollins Andrew M, and Dupps William J. A review of structural and biomechanical changes in the cornea in aging, disease, and photochemical crosslinking. *Frontiers in bioengineering and biotechnology*, 7:66, 2019.

[76] Singh Manmohan, Han Zhaolong, Li Jiasong, Vantipalli Srilatha, Aglyamov Salavat R, Twa Michael D, and Larin Kirill V. Quantifying the effects of hydration on corneal stiffness with noncontact optical coherence elastography. *Journal of Cataract & Refractive Surgery*, 44(8):1023–1031, 2018.

[77] Petsche Steven J, Chernyak Dimitri, Martiz Jaime, Levenston Marc E, and Pinsky Peter M. Depth-dependent transverse shear properties of the human corneal stroma. *Investigative ophthalmology & visual science*, 53(2):873–880, 2012.

[78] Hjortdal Jesper Ø. Regional elastic performance of the human cornea. *Journal of biomechanics*, 29(7):931–942, 1996.

[79] Binder Perry S. Ectasia after laser in situ keratomileusis. *Journal of Cataract & Refractive Surgery*, 29(12):2419–2429, 2003.

[80] Meek Keith M, Tuft Stephen J, Huang Yifei, Gill Paulvinder S, Hayes Sally, Newton Richard H, and Bron Anthony J. Changes in collagen orientation and distribution in keratoconus corneas. *Investigative ophthalmology & visual science*, 46(6):1948–1956, 2005.

[81] Cartwright Nathaniel E Knox, Tyrer John R, and Marshall John. Age-related differences in the elasticity of the human cornea. *Investigative ophthalmology & visual science*, 52(7):4324–4329, 2011.

[82] Wollensak Gregor, Spoerl Eberhard, and Seiler Theo. Riboflavin/ultraviolet-a–induced collagen crosslinking for the treatment of keratoconus. *American journal of ophthalmology*, 135(5):620–627, 2003.

[83] Meiri Zohar, Keren Shay, Rosenblatt Amir, Sarig Tal, Shenhav Liat, and Varssano David. Efficacy of corneal collagen cross-linking for the treatment of keratoconus: a systematic review and meta-analysis. *Cornea*, 35(3):417–428, 2016.

[84] Gonzalez-Andrades Miguel, Argüeso Pablo, and Gipson Ilene. Corneal anatomy. In *Corneal Regeneration*, pages 3–12. Springer, 2019.

[85] Meek Keith M and Knupp Carlo. Corneal structure and transparency. *Progress in retinal and eye research*, 49:1–16, 2015.

[86] Vinciguerra Riccardo, Ambrósio Jr Renato, Roberts Cynthia J, Azzolini Claudio, and Vinciguerra Paolo. Biomechanical characterization of subclinical keratoconus without topographic or tomographic abnormalities. *Journal of Refractive Surgery*, 33(6):399–407, 2017.

[87] Roy Abhijit Sinha, Shetty Rohit, and Kummelil Mathew Kurian. Keratoconus: a biomechanical perspective on loss of corneal stiffness. *Indian Journal of Ophthalmology*, 61(8):392, 2013.

[88] Antoine Ramier, Behrouz Tavakol, and Seok-Hyun Yun. Measuring mechanical wave speed, dispersion, and viscoelastic modulus of the cornea using optical coherence elastography. *Optics express*, 27(12):16635–16649, 2019.

[89] Han Zhaolong, Li Jiasong, Singh Manmohan, Wu Chen, Liu Chih-hao, Raghunathan Raksha, Aglyamov Salavat R, Vantipalli Srilatha, Twa Michael D, and Larin Kirill V. Optical coherence elastography assessment of corneal viscoelasticity with a modified rayleigh-lamb wave model. *Journal of the mechanical behavior of biomedical materials*, 66:87–94, 2017.

[90] David Touboul, Jean-Luc Gennisson, Thu-Mai Nguyen, Antoine Robinet, Cynthia J Roberts, Mickael Tanter, and Nicolas Grenier. Supersonic shear wave elastography for the in vivo evaluation of transepithelial corneal collagen cross-linking. *Investigative ophthalmology & visual science*, 55(3):1976–1984, 2014.

[91] Thu-Mai Nguyen, Jean-Francois Aubry, Mathias Fink, Bercoff Jeremy, and Mickael Tanter. In vivo evidence of porcine cornea anisotropy using supersonic shear wave imaging. *Investigative ophthalmology & visual science*, 55(11):7545–7552, 2014.

[92] Mickaël Tanter, David Touboul, Jean-Luc Gennisson, Bercoff Jeremy, and Mathias Fink. High-resolution quantitative imaging of cornea elasticity using supersonic shear imaging. *IEEE transactions on medical imaging*, 28(12):1881–1893, 2009.

[93] Chen Pei-Yu, Shih Cho-Chiang, Lin Wei-Chen, Ma Teng, Zhou Qifa, Shung K Kirk, and Huang Chih-Chung. High-resolution shear wave imaging of the human cornea using a dual-element transducer. *Sensors*, 18(12):4244, 2018.

[94] Qian Xuejun, Ma Teng, Shih Cho-Chiang, Heur Martin, Zhang Jun, Shung Koping Kirk, Varma Rohit, Humayun Mark S, and Zhou Qifa.

Ultrasonic microelastography to assess biomechanical properties of the cornea. *IEEE Transactions on Biomedical Engineering*, 66(3):647–655, 2018.

[95] Couade Mathieu, Pernot Mathieu, Prada Claire, Messas Emmanuel, Emmerich Joseph, Bruneval Patrick, Criton Aline, Fink Mathias, and Tanter Mickael. Quantitative assessment of arterial wall biomechanical properties using shear wave imaging. *Ultrasound in medicine & biology*, 36(10):1662–1676, 2010.

[96] Mitchell A Kirby, Ivan Pelivanov, Song Shaozhen, Ambrozinski Lukasz, Soon Joon Yoon, Liang Gao, Li David, Tueng T Shen, Wang Ruikang K, and Matthew O'Donnell. Optical coherence elastography in ophthalmology. *Journal of biomedical optics*, 22(12):121720, 2017.

[97] Zaitsev Vladimir Y, Matveyev Alexander L, Matveev Lev A, Sovetsky Alexander A, Hepburn Matt S, Mowla Alireza, and Kennedy Brendan F. Strain and elasticity imaging in compression optical coherence elastography: The two-decade perspective and recent advances. *Journal of Biophotonics*, 14(2):e202000257, 2021.

[98] Matt S Hepburn, Wijesinghe Philip, Lixin Chin, and Brendan F Kennedy. Analysis of spatial resolution in phase-sensitive compression optical coherence elastography. *Biomedical optics express*, 10(3):1496–1513, 2019.

[99] Song Shaozhen, Wei Wei, Hsieh Bao-Yu, Ivan Pelivanov, Tueng T Shen, Matthew O'Donnell, and Wang Ruikang K. Strategies to improve phase-stability of ultrafast swept source optical coherence tomography for single shot imaging of transient mechanical waves at 16 khz frame rate. *Applied physics letters*, 108(19):191104, 2016.

[100] Yuhang Hu and Zhigang Suo. Viscoelasticity and poroelasticity in elastomeric gels. *Acta Mechanica Solida Sinica*, 25(5):441–458, 2012.

[101] Wang Qi-Ming, Anirudh C Mohan, Michelle L Oyen, and Xuan-He Zhao. Separating viscoelasticity and poroelasticity of gels with different length and time scales. *Acta Mechanica Sinica*, 30(1):20–27, 2014.

[102] Al Mayah Adil. *Biomechanics of Soft Tissues: Principles and Applications*. CRC Press, 2018.

[103] Helen Muir. Proteoglycans as organizers of the intercellular matrix, 1983.

[104] Michael A Soltz and Gerard A Ateshian. Experimental verification and theoretical prediction of cartilage interstitial fluid pressurization at an impermeable contact interface in confined compression. *Journal of biomechanics*, 31(10):927–934, 1998.

[105] Luis Cardoso and Stephen C Cowin. Role of structural anisotropy of biological tissues in poroelastic wave propagation. *Mechanics of Materials*, 44:174–188, 2012.

[106] J Brum, M Bernal, JL Gennisson, and M Tanter. In vivo evaluation of the elastic anisotropy of the human achilles tendon using shear wave dispersion analysis. *Physics in Medicine & Biology*, 59(3):505, 2014.

[107] Peralta L, G Rus, Bochud N, and Molina FS. Assessing viscoelasticity of shear wave propagation in cervical tissue by multiscale computational simulation. *Journal of biomechanics*, 48(9):1549–1556, 2015.

[108] Nitta Naotaka, Shiina Tsuyoshi, and Ei Ueno. Quantitative assessment and imaging of viscoelastic properties of soft tissue. In *2002 IEEE Ultrasonics Symposium, 2002. Proceedings.*, volume 2, pages 1885–1889. IEEE, 2002.

[109] Sack Ingolf, Jöhrens Korinna, Würfel Jens, and Braun Jürgen. Structure-sensitive elastography: on the viscoelastic powerlaw behavior of in vivo human tissue in health and disease. *Soft Matter*, 9(24):5672–5680, 2013.

[110] Shiina Tsuyoshi, Nightingale Kathryn R, Palmeri Mark L, Timothy J Hall, Jeffrey C Bamber, Richard G Barr, Castera Laurent, Choi Byung Ihn, Yi-Hong Chou, Cosgrove David, et al. Wfumb guidelines and recommendations for clinical use of ultrasound elastography: Part 1: basic principles and terminology. *Ultrasound in medicine & biology*, 41(5):1126–1147, 2015.

[111] Gautieri Alfonso, Vesentini Simone, Redaelli Alberto, and Ballarini Roberto. Modeling and measuring visco-elastic properties: From collagen molecules to collagen fibrils. *International Journal of Non-Linear Mechanics*, 56:25–33, 2013.

[112] García A, Martínez MA, and Pena E. Viscoelastic properties of the passive mechanical behavior of the porcine carotid artery: influence of proximal and distal positions. *Biorheology*, 49(4):271–288, 2012.

[113] L Soby, AM Jamieson, J Blackwell, Choi HU, and Rosenberg LC. Viscoelastic and rheological properties of concentrated solutions of proteoglycan subunit and proteoglycan aggregate. *Biopolymers: Original Research on Biomolecules*, 29(12-13):1587–1592, 1990.

[114] M Sridhar, J Liu, and Insana MF. Viscoelasticity imaging using ultrasound: parameters and error analysis. *Physics in Medicine & Biology*, 52(9):2425, 2007.

[115] Liliana Schaefer, Claudia Tredup, Gubbiotti Maria A, and Renato V Iozzo. Proteoglycan neofunctions: regulation of inflammation and autophagy in cancer biology. *The FEBS journal*, 284(1):10–26, 2017.

[116] Helena Frey, Nina Schroeder, Tina Manon-Jensen, Renato V Iozzo, and Liliana Schaefer. Biological interplay between proteoglycans and their innate immune receptors in inflammation. *The FEBS journal*, 280(10):2165–2179, 2013.

[117] Losa Gabriele A and Alini Mauro. Sulfated proteoglycans in the extracellular matrix of human breast tissues with infiltrating carcinoma. *International journal of cancer*, 54(4):552–557, 1993.

[118] Lone K Petersen, Oxlund H, Uldbjerg N, and A Forman. In vitro analysis of muscular contractile ability and passive biomechanical properties of uterine cervical samples from nonpregnant women. *Obstetrics and gynecology*, 77(5):772–776, 1991.

[119] Shibnath Ghatak, Edward V Maytin, Judith A Mack, Vincent C Hascall, Atanelishvili Ilia, Ricardo Moreno Rodriguez, Markwald Roger R, and Misra Suniti. Roles of proteoglycans and glycosaminoglycans in wound healing and fibrosis. *International journal of cell biology*, 2015, 2015.

[120] Ricardo L Armentano, Barra Juan G, Santana Daniel Bia, Pessana Franco M, Graf Sebastian, Damian Craiem, Brandani Laura M, Hugo P Baglivo, and Ramiro A Sanchez. Smart damping modulation of carotid wall energetics in human hypertension: effects of angiotensin-converting enzyme inhibition. *Hypertension*, 47(3):384–390, 2006.

[121] Yamaoka Kazuaki, Nouchi Toshihiko, Fumiaki Marumo, and Chifumi Sato. α-smooth-muscle actin expression in normal and fibrotic human livers. *Digestive diseases and sciences*, 38(8):1473–1479, 1993.

[122] GJ Langewouters, Wesseling KH, and Goedhard WJA. The pressure dependent dynamic elasticity of 35 thoracic and 16 abdominal human

aortas in vitro described by a five component model. *Journal of biomechanics*, 18(8):613–620, 1985.

[123] Viksit Kumar, Max Denis, Adriana Gregory, Mahdi Bayat, Mehrmohammadi Mohammad, Robert Fazzio, Fatemi Mostafa, and Alizad Azra. Viscoelastic parameters as discriminators of breast masses: Initial human study results. *PloS one*, 13(10):e0205717, 2018.

[124] Nabavizadeh Alireza, Mahdi Bayat, Viksit Kumar, Adriana Gregory, Webb Jeremy, Alizad Azra, and Fatemi Mostafa. Viscoelastic biomarker for differentiation of benign and malignant breast lesion in ultra-low frequency range. *Scientific reports*, 9(1):5737, 2019.

[125] Ralph Sinkus, Katja Siegmann, Tanja Xydeas, Mickael Tanter, Claus Claussen, and Mathias Fink. Mr elastography of breast lesions: understanding the solid/liquid duality can improve the specificity of contrast-enhanced mr mammography. *Magnetic Resonance in Medicine: An Official Journal of the International Society for Magnetic Resonance in Medicine*, 58(6):1135–1144, 2007.

[126] C Balleyguier, Canale S, W Ben Hassen, Vielh P, EH Bayou, MC Mathieu, C Uzan, C Bourgier, and C Dromain. Breast elasticity: principles, technique, results: an update and overview of commercially available software. *European Journal of Radiology*, 82(3):427–434, 2013.

[127] Palmeri Mark L and Nightingale Kathryn R. What challenges must be overcome before ultrasound elasticity imaging is ready for the clinic? *Imaging in medicine*, 3(4):433, 2011.

[128] Sara Aristizabal, Carolina Amador Carrascal, Ivan Z Nenadic, Greenleaf James F, and Matthew W Urban. Application of acoustoelasticity to evaluate nonlinear modulus inex vivokidneys. *IEEE transactions on ultrasonics, ferroelectrics, and frequency control*, 65(2):188–200, 2018.

[129] Katharina Schregel, Eva Wuerfel née Tysiak, Philippe Garteiser, Ines Gemeinhardt, Prozorovski Timour, Orhan Aktas, Hartmut Merz, Dirk Petersen, Jens Wuerfel, and Ralph Sinkus. Demyelination reduces brain parenchymal stiffness quantified in vivo by magnetic resonance elastography. *Proceedings of the National Academy of Sciences*, 109(17):6650–6655, 2012.

[130] Kaspar-Josche Streitberger, Ingolf Sack, Krefting Dagmar, Caspar Pfüller, Jürgen Braun, Friedemann Paul, and Jens Wuerfel. Brain vis-

coelasticity alteration in chronic-progressive multiple sclerosis. *PloS one*, 7(1):e29888, 2012.

[131] Ingolf Sack, Beierbach Bernd, Jens Wuerfel, Dieter Klatt, Uwe Hamhaber, Sebastian Papazoglou, Peter Martus, and Jürgen Braun. The impact of aging and gender on brain viscoelasticity. *Neuroimage*, 46(3):652–657, 2009.

[132] Monica E Susilo, Jeffrey A Paten, Edward A Sander, Thao D Nguyen, and Ruberti Jeffrey W. Collagen network strengthening following cyclic tensile loading. *Interface focus*, 6(1):20150088, 2016.

[133] Lianghao Han, Michael Burcher, and Noble J Alison. Non-invasive measurement of biomechanical properties of in vivo soft tissues. In *International Conference on Medical Image Computing and Computer-Assisted Intervention*, pages 208–215. Springer, 2002.

[134] Callejas Antonio, Gomez Antonio, Melchor Juan, Riveiro Miguel, Massó Paloma, Torres Jorge, López-López Modesto, and Rus Guillermo. Performance study of a torsional wave sensor and cervical tissue characterization. *Sensors*, 17(9):2078, 2017.

[135] Shigao Chen, Matthew W Urban, Cristina Pislaru, Randall Kinnick, Zheng Yi, Aiping Yao, and Greenleaf James F. Shearwave dispersion ultrasound vibrometry (sduv) for measuring tissue elasticity and viscosity. *IEEE transactions on ultrasonics, ferroelectrics, and frequency control*, 56(1):55–62, 2009.

[136] Serra-Aguila A, Puigoriol-Forcada JM, Reyes G, and Menacho J. Viscoelastic models revisited: characteristics and interconversion formulas for generalized kelvin–voigt and maxwell models. *Acta Mechanica Sinica*, pages 1–19, 2019.

[137] Cedric Schmitt, Henni Anis Hadj, and Guy Cloutier. Characterization of blood clot viscoelasticity by dynamic ultrasound elastography and modeling of the rheological behavior. *Journal of biomechanics*, 44(4):622–629, 2011.

[138] Fung Yuan-cheng. *Biomechanics: mechanical properties of living tissues*. Springer Science & Business Media, 2013.

[139] KJ Parker, T Szabo, and S Holm. Towards a consensus on rheological models for elastography in soft tissues. *Physics in Medicine & Biology*, 64(21):215012, 2019.

[140] RC Koeller. Applications of fractional calculus to the theory of viscoelasticity. 1984.

[141] Rus Guillermo. Nature of acoustic nonlinear radiation stress. *Applied Physics Letters*, 105(12):121904, 2014.

[142] Antonio Gomez. *Transurethral Shear Wave Elastography for prostate cancer*. PhD thesis, University College London, 2018.

[143] Marko Orescanin, Wang Yue, and Insana Michael F. 3-d fdtd simulation of shear waves for evaluation of complex modulus imaging. *IEEE transactions on ultrasonics, ferroelectrics, and frequency control*, 58(2):389–398, 2011.

[144] Bercoff Jérémy, Tanter Mickaël, Muller Marie, and Fink Mathias. The role of viscosity in the impulse diffraction field of elastic waves induced by the acoustic radiation force. *IEEE transactions on ultrasonics, ferroelectrics, and frequency control*, 51(11):1523–1536, 2004.

[145] Li-Hua Chen, Ng Sun-Pui, Winnie Yu, Jie Zhou, and KW Frances Wan. A study of breast motion using non-linear dynamic fe analysis. *Ergonomics*, 56(5):868–878, 2013.

[146] Salameh Najat, Frank Peeters, Ralph Sinkus, Jorge Abarca-Quinones, Laurence Annet, Leon C Ter Beek, Isabelle Leclercq, and Bernard E Van Beers. Hepatic viscoelastic parameters measured with mr elastography: correlations with quantitative analysis of liver fibrosis in the rat. *Journal of Magnetic Resonance Imaging: An Official Journal of the International Society for Magnetic Resonance in Medicine*, 26(4):956–962, 2007.

[147] Palacio-Torralba Javier, Steven Hammer, Good Daniel W, S Alan McNeill, Grant D Stewart, Robert L Reuben, and Yuhang Chen. Quantitative diagnostics of soft tissue through viscoelastic characterization using time-based instrumented palpation. *journal of the mechanical behavior of biomedical materials*, 41:149–160, 2015.

[148] Jonathan Vappou, Maleke Caroline, and Elisa E Konofagou. Quantitative viscoelastic parameters measured by harmonic motion imaging. *Physics in Medicine & Biology*, 54(11):3579, 2009.

[149] Zhang Man, Castaneda Benjamin, Zhe Wu, Nigwekar Priya, Joseph Jean V, Rubens Deborah J, and Parker Kevin J. Congruence of

imaging estimators and mechanical measurements of viscoelastic properties of soft tissues. *Ultrasound in medicine & biology*, 33(10):1617–1631, 2007.

[150] Mittanamalli S Sridhar. Anatomy of cornea and ocular surface. *Indian journal of ophthalmology*, 66(2):190, 2018.

[151] Gennisson Jean-luc, Provost Jean, Deffieux Thomas, Papadacci Clément, Imbault Marion, Pernot Mathieu, and Tanter Mickael. 4-d ultrafast shear-wave imaging. *IEEE transactions on ultrasonics, ferroelectrics, and frequency control*, 62(6):1059–1065, 2015.

[152] Annin B.D. and Ostrosablin N.I. Anisotropy of elastic properties of materials. *Journal of Applied Mechanics and Technical Physics*, 49(6):998–1014, 2008.

[153] Yoram Lanir. Multi-scale structural modeling of soft tissues mechanics and mechanobiology. *Journal of Elasticity*, 129(1-2):7–48, 2017.

[154] Pritchard Robyn H, Huang Yan Yan Shery, and Eugene M Terentjev. Mechanics of biological networks: from the cell cytoskeleton to connective tissue. *Soft matter*, 10(12):1864–1884, 2014.

[155] Rafael Muñoz and Juan Melchor. Nonlinear classical elasticity model for materials with fluid and matrix phases. *Mathematical Problems in Engineering*, 2018, 2018.

[156] Sevan Goenezen, Dord Jean-Francois, Zac Sink, Barbone Paul E, Jiang Jingfeng, Timothy J Hall, and Oberai Assad A. Linear and nonlinear elastic modulus imaging: an application to breast cancer diagnosis. *IEEE transactions on medical imaging*, 31(8):1628–1637, 2012.

[157] Landau Lev Davidovich and Lifshitz Eugin M. *Course of Theoretical Physics Vol 7: Theory and Elasticity*. Pergamon press, 1959.

[158] FD Murnaghan. The compressibility of media under extreme pressures. *Proceedings of the national academy of sciences of the United States of America*, 30(9):244, 1944.

[159] T Christian Gasser, Ray W Ogden, and Gerhard A Holzapfel. Hyperelastic modelling of arterial layers with distributed collagen fibre orientations. *Journal of the royal society interface*, 3(6):15–35, 2005.

[160] Ray W Ogden and Gerhard A Holzapfel. *Mechanics of biological tissue*. Springer, 2006.

[161] NC Ovenden and Walsh CL. Fundamentals of physiological solid mechanics. In *Fluid and Solid Mechanics*, pages 169–217. World Scientific, 2016.

[162] Veronda DR and RA Westmann. Mechanical characterization of skin—finite deformations. *Journal of biomechanics*, 3(1):111–124, 1970.

[163] Fung YC. Elasticity of soft tissues in simple elongation. *American Journal of Physiology-Legacy Content*, 213(6):1532–1544, 1967.

[164] Wex Cora, Arndt Susann, Stoll Anke, Bruns Christiane, and Kupriyanova Yuliya. Isotropic incompressible hyperelastic models for modelling the mechanical behaviour of biological tissues: a review. *Biomedical Engineering/Biomedizinische Technik*, 60(6):577–592, 2015.

[165] M Kohandel, S Sivaloganathan, Tenti G, and Drake JM. The constitutive properties of the brain parenchyma: Part 1. strain energy approach. *Medical engineering & physics*, 28(5):449–454, 2006.

[166] Rashid Badar, Destrade Michel, and Michael D Gilchrist. Mechanical characterization of brain tissue in simple shear at dynamic strain rates. *Journal of the mechanical behavior of biomedical materials*, 28:71–85, 2013.

[167] Zhan Gao and Desai Jaydev P. Estimating zero-strain states of very soft tissue under gravity loading using digital image correlation. *Medical image analysis*, 14(2):126–137, 2010.

[168] Yuan-Chiao Lu, Andrew R Kemper, and Costin D Untaroiu. Effect of storage on tensile material properties of bovine liver. *Journal of the mechanical behavior of biomedical materials*, 29:339–349, 2014.

[169] Costin D Untaroiu and Yuan-Chiao Lu. Material characterization of liver parenchyma using specimen-specific finite element models. *Journal of the mechanical behavior of biomedical materials*, 26:11–22, 2013.

[170] Baah-Dwomoh Adwoa, McGuire Jeffrey, Tan Ting, and De Vita Raffaella. Mechanical properties of female reproductive organs and supporting connective tissues: a review of the current state of knowledge. *Applied Mechanics Reviews*, 68(6), 2016.

[171] Barnum Carrie E, Fey Jennifer L, Weiss Stephanie N, Barila Guillermo, Brown Amy G, Connizzo Brianne K, Shetye Snehal S, Elovitz Michal

A, and Soslowsky Louis J. Tensile mechanical properties and dynamic collagen fiber re-alignment of the murine cervix are dramatically altered throughout pregnancy. *Journal of biomechanical engineering*, 139(6), 2017.

[172] Myers Kristin M, Paskaleva AP, House Michael, and Socrate Simona. Mechanical and biochemical properties of human cervical tissue. *Acta biomaterialia*, 4(1):104–116, 2008.

[173] Michael J Poellmann, Edward K Chien, Barbara L McFarlin, and Amy J Wagoner Johnson. Mechanical and structural changes of the rat cervix in late-stage pregnancy. *Journal of the mechanical behavior of biomedical materials*, 17:66–75, 2013.

[174] Yoshida Kyoko, Mahendroo Mala, Vink Joy, Wapner Ronald, and Myers Kristin. Material properties of mouse cervical tissue in normal gestation. *Acta biomaterialia*, 36:195–209, 2016.

[175] Barone William R, Feola Andrew J, Moalli Pamela A, and Abramowitch Steven D. The effect of pregnancy and postpartum recovery on the viscoelastic behavior of the rat cervix. *Journal of mechanics in medicine and biology*, 12(01):1250009, 2012.

[176] Myers Kristin M, Socrate Simona, Paskaleva Anastassia, and House Michael. A study of the anisotropy and tension/compression behavior of human cervical tissue. *Journal of biomechanical engineering*, 132(2):021003, 2010.

[177] Jayyosi C, Lee N, A Willcockson, S Nallasamy, M Mahendroo, and K Myers. The mechanical response of the mouse cervix to tensile cyclic loading in term and preterm pregnancy. *Acta biomaterialia*, 78:308–319, 2018.

[178] Joseph Jordan, Albert Singer, Howard Jones, and Shafi Mahmood. *The cervix*. John Wiley & Sons, 2009.

[179] House Michael, David L Kaplan, and Socrate Simona. Relationships between mechanical properties and extracellular matrix constituents of the cervical stroma during pregnancy. In *Seminars in perinatology*, volume 33, pages 300–307. Elsevier, 2009.

[180] Phyllis C Leppert. Anatomy and physiology of cervical ripening. *Clinical obstetrics and gynecology*, 38(2):267–279, 1995.

[181] Jorge Torres, Inas Faris, and Antonio Callejas. Histobiomechanical remodeling of the cervix during pregnancy: proposed framework. *Mathematical Problems in Engineering*, vol(no):000–001, 2019.

[182] Kristin Myers, Socrate Simona, Dimitrios Tzeranis, and House Michael. Changes in the biochemical constituents and morphologic appearance of the human cervical stroma during pregnancy. *European Journal of Obstetrics & Gynecology and Reproductive Biology*, 144:S82–S89, 2009.

[183] Zork Noelia M, Myers Kristin M, Yoshida Kyoko, Cremers Serge, Jiang Hongfeng, Ananth Cande V, Wapner Ronald J, Kitajewski Jan, and Vink Joy. A systematic evaluation of collagen cross-links in the human cervix. *American journal of obstetrics and gynecology*, 212(3):321–e1, 2015.

[184] Elaine Nicpon Marieb and Katja Hoehn. *Human anatomy & physiology*. Pearson Education, 2007.

[185] Natali Arturo N, Emanuele L Carniel, and Hans Gregersen. Biomechanical behaviour of oesophageal tissues: material and structural configuration, experimental data and constitutive analysis. *Medical engineering & physics*, 31(9):1056–1062, 2009.

[186] Massó Paloma, Callejas Antonio, Melchor Juan, Molina Francisca S, and Rus Guillermo. In vivo measurement of cervical elasticity on pregnant women by torsional wave technique: A preliminary study. *Sensors*, 19(15):3249, 2019.

[187] Rus Guillermo, Muñoz Rafael, Melchor Juan, Molina Ruben, Callejas Antonio, Riveiro Miguel, Massó Paloma, Torres Jorge, Moreu Gerardo, Molina Francisca, et al. Torsion ultrasonic sensor for tissue mechanical characterization. In *2016 IEEE International Ultrasonics Symposium (IUS)*, pages 1–4. IEEE, 2016.

[188] Callejas Antonio, Gomez Antonio, Faris Inas H, Melchor Juan, and Rus Guillermo. Kelvin–voigt parameters reconstruction of cervical tissue-mimicking phantoms using torsional wave elastography. *Sensors*, 19(15):3281, 2019.

[189] LD Landau and EM Lifshitz. Elasticity theory. 1975.

[190] Hamilton Mark F, Ilinskii Yurii A, and Zabolotskaya Evgenia A. Separation of compressibility and shear deformation in the elastic energy density (l). *The Journal of the Acoustical Society of America*, 116(1):41–44, 2004.

[191] Destrade Michel and Raymond W Ogden. On the third-and fourth-order constants of incompressible isotropic elasticity. *The Journal of the Acoustical Society of America*, 128(6):3334–3343, 2010.

[192] A Cemal Eringen and Suhubi ES. Nonlinear theory of simple micro-elastic solids. *International Journal of Engineering Science*, 2(2):189–203, 1964.

[193] Melvin Mooney. A theory of large elastic deformation. *Journal of applied physics*, 11(9):582–592, 1940.

[194] RS Rivlin. Large elastic deformations of isotropic materials iv. further developments of the general theory. *Philosophical Transactions of the Royal Society of London. Series A, Mathematical and Physical Sciences*, 241(835):379–397, 1948.

[195] Martins PALS, Natal Jorge RM, and Ferreira AJM. A comparative study of several material models for prediction of hyperelastic properties: Application to silicone-rubber and soft tissues. *Strain*, 42(3):135–147, 2006.

[196] Raymond William Ogden. Large deformation isotropic elasticity–on the correlation of theory and experiment for incompressible rubberlike solids. *Proceedings of the Royal Society of London. A. Mathematical and Physical Sciences*, 326(1567):565–584, 1972.

[197] O'Hara Sandra, Marilyn Zelesco, and Zhonghua Sun. Can shear wave elastography of the cervix be of use in predicting imminent cervical insufficiency and preterm birth?-preliminary results. *Ultrasound in Medicine and Biology*, 45:S111–S112, 2019.

[198] Eric Reissner and Sagoci HF. Forced torsional oscillations of an elastic half-space. i. *Journal of Applied Physics*, 15(9):652–654, 1944.

[199] Hadj Henni Anis, Cédric Schmitt, Isabelle Trop, and Guy Cloutier. Shear wave induced resonance elastography of spherical masses with polarized torsional waves. *Applied physics letters*, 100(13):133702, 2012.

[200] Ouared Abderrahmane, Emmanuel Montagnon, and Guy Cloutier. Generation of remote adaptive torsional shear waves with an octagonal phased array to enhance displacements and reduce variability of shear wave speeds: Comparison with quasi-plane shear wavefronts. *Physics in Medicine & Biology*, 60(20):8161, 2015.

[201] Sanjay S Yengul, Barbone Paul E, and Madore Bruno. Dispersion in tissue-mimicking gels measured with shear wave elastography and torsional vibration rheometry. *Ultrasound in medicine & biology*, 45(2):586–604, 2019.

[202] J Melchor and G Rus. Torsional ultrasonic transducer computational design optimization. *Ultrasonics*, 54(7):1950–1962, 2014.

[203] Abderrahmane Ouared, Emmanuel Montagnon, and Guy Cloutier. Generation of remote adaptive torsional shear waves with an octagonal phased array to enhance displacements and reduce variability of shear wave speeds: comparison with quasi-plane shear wavefronts. *Physics in medicine and biology*, 60 20:8161–85, 2015.

[204] S. R. Aglyamov, S. Park, Y. A. Ilinskii, and S. Y. Emelianov. Ultrasound imaging of soft tissue shear viscosity. In *IEEE Symposium on Ultrasonics, 2003*, volume 1, pages 937–940 Vol.1, 2003.

[205] INNITIUS Patent. Transductor ultrasónico de torsión para diagnóstico tisular. *Extensiones Internacionales, PCT/ES2012/070380*, 2011.

[206] INNITIUS Patent. Dispositivo emisor de ondas ultrasónicas de torsión y transductor que lo comprende. *Extensiones Internacionales, PCT/ES2016/070540*, 2015.

[207] Juan Manuel Melchor and Guillermo Rus. Torsional ultrasonic transducer computational design optimization. *Ultrasonics*, 54 7:1950–62, 2014.

[208] Melchor Juan, Muñoz Rafael, and Guillermo Rus. Torsional ultrasound sensor optimization for soft tissue characterization. *Sensors*, 17(6):1402, 2017.

[209] Jens Heichel, Frank Wilhelm, Kathleen S Kunert, and Thomas Hammer. Topographic Findings of the Porcine Cornea. *Med. hypothesis, Discov. Innov. Ophthalmol. J.*, 5(4):125–131, 2016.

[210] Mitchell A. Kirby, Ivan Pelivanov, Shaozhen Song, Łukasz Ambrozinski, Soon Joon Yoon, Liang Gao, David Li, Tueng T. Shen, Ruikang K. Wang, and Matthew O'Donnell. Optical coherence elastography in ophthalmology. *J. Biomed. Opt.*, 22(12):1, dec 2017.

[211] Peralta Laura, Molina Francisca Sonia, Juan Melchor, Luisa Fernanda Gómez, Paloma Massó, Jesús Florido, and Guillermo Rus. Transient elastography to assess the cervical ripening during pregnancy: A

preliminary study. *Ultraschall in der Medizin-European Journal of Ultrasound*, 38(04):395–402, 2017.

[212] Jeremy Bercoff, Mickaex0308l Tanter, and M K Fink. Supersonic shear imaging: a new technique for soft tissue elasticity mapping. *IEEE Transactions on Ultrasonics, Ferroelectrics and Frequency Control*, 51:396–409, 2004.

[213] Deng Yufeng, Rouze Ned C, Palmeri Mark L, and Nightingale Kathryn R. Ultrasonic shear wave elasticity imaging sequencing and data processing using a verasonics research scanner. *IEEE transactions on ultrasonics, ferroelectrics, and frequency control*, 64(1):164–176, 2016.

[214] José M. Carcione, editor. *Wave Fields in Real Media (Third Edition)*. Elsevier, third edition edition, 2015.

[215] Laura Peralta. *Feasibility of using ultrasonic shear waves to assess cervical remodelling during the gestation period*. PhD thesis, Departamento de Mecánica Estructural e Ingeniería Hidráulica, University of Granada, May 2015.

[216] Stefan Catheline, Jean luc Gennisson, Giles Delon, Mathias Fink, Ralph Sinkus, Saïd Abouelkaram, and Joseph Culioli. Measuring of viscoelastic properties of homogeneous soft solid using transient elastography: an inverse problem approach. *The Journal of the Acoustical Society of America*, 116 6:3734–41, 2004.

[217] Thanasis Loupas, J. Powers, and R. W. Gill. An axial velocity estimator for ultrasound blood flow imaging, based on a full evaluation of the doppler equation by means of a two-dimensional autocorrelation approach. *IEEE Transactions on Ultrasonics, Ferroelectrics and Frequency Control*, 42:672–688, 1995.

[218] Alfonso Rodriguez-Molares, Ole Marius Hoel Rindal, Olivier Bernard, Hervé Liebgott, Andreas Austeng, and Lasse Lovstakken. The ultrasound toolbox. *2017 IEEE International Ultrasonics Symposium (IUS)*, pages 1–1, 2017.

[219] Mansouri MR and Darijani H. Constitutive modeling of isotropic hyperelastic materials in an exponential framework using a self-contained approach. *International Journal of Solids and Structures*, 51(25-26):4316–4326, 2014.

[220] Richard M Aspden. Collagen organisation in the cervix and its relation to mechanical function. *Collagen and related research*, 8(2):103–112, 1988.

[221] Patalano Antoine, García Carlos Marcelo, and Rodríguez Andrés. Rectification of image velocity results (river): a simple and user-friendly toolbox for large scale water surface particle image velocimetry (piv) and particle tracking velocimetry (ptv). *Computers & Geosciences*, 109:323–330, 2017.

[222] Patalano A, Garcia CM, Brevis W, Bleninger T, Guillen N, Moreno L, and Rodriguez A. Recent advances in eulerian and lagragian large-scale particle image velocimetry. In *E-proceedings of the 36th IAHR World Congress, The Hauge, Netherlands*, 2015.

[223] Park Jeong-Man, Choi Seung-Min, Kwon Sung-Jae, and Jeong Mok-Kun. Measurement of the shear modulus of an ultrasound tissue phantom. *The Journal of the Acoustical Society of Korea*, 31(6):399–409, 2012.

[224] Barbrina L. Dunmire, John C. Kucewicz, Stuart B. Mitchell, Lawrence A. Crum, and Kevin Michael Sekins. Characterizing an agar/gelatin phantom for image guided dosing and feedback control of high-intensity focused ultrasound. *Ultrasound in medicine & biology*, 39 2:300–11, 2013.

[225] Mark L. Palmeri, Stephen A. McAleavey, Gregg E. Trahey, and Kathryn Nightingale. Ultrasonic tracking of acoustic radiation force-induced displacements in homogeneous media. *IEEE Transactions on Ultrasonics, Ferroelectrics and Frequency Control*, 53:1300–1313, 2006.

[226] Thomas Deffieux, Jean luc Gennisson, Benoît Larrat, Maximilian Fink, and Mickaël Tanter. The variance of quantitative estimates in shear wave imaging: Theory and experiments. *IEEE Transactions on Ultrasonics, Ferroelectrics and Frequency Control*, 59, 2012.

[227] Marko B. Orescanin, Muqeem A. Qayyum, Kathleen S. Toohey, and Michael F. Insana. Complex shear modulus of thermally-damaged liver. *2009 IEEE International Ultrasonics Symposium*, pages 127–130, 2009.

[228] Christopher Taylor Barry, Bradley Jay Mills, Zaegyoo Hah, Robert A Mooney, Charlotte Kathryn Ryan, Deborah J. Rubens, and Kevin J. Parker. Shear wave dispersion measures liver steatosis. *Ultrasound in medicine & biology*, 38 2:175–82, 2012.

[229] Seong-Ook Kim, Sang-Yun Lee, So-Ick Jang, Soo jin Park, Hye-Won Kwon, Seong-Ho Kim, Chin Siong Lee, Eun-Seok Choi, Seong-Kyu

Cho, Sun Hwa Hong, and Yang-Min Kim. Hepatic stiffness using shear wave elastography and the related factors for a fontan circulation. *Pediatric Cardiology*, 39:57–65, 2017.

[230] Xuan Zhou Ding, Debaditya Dutta, Ahmed Mustafa Mahmoud, Bryan W. Tillman, Steven A. Leers, and Kang Kim. An adaptive displacement estimation algorithm for improved reconstruction of thermal strain. *IEEE Transactions on Ultrasonics, Ferroelectrics, and Frequency Control*, 62:138–151, 2015.

[231] Gianmarco Pinton, Jeremy J. Dahl, and Gregg E. Trahey. Rapid tracking of small displacements with ultrasound. *IEEE Transactions on Ultrasonics, Ferroelectrics and Frequency Control*, 53:1103–1117, 2006.

[232] M. Fink, L. Sandrin, M. Tanter, S. Catheline, S. Chaffai, J. Bercoff, and J. Gennisson. Ultra high speed imaging of elasticity. In *2002 IEEE Ultrasonics Symposium, 2002. Proceedings.*, volume 2, pages 1811–1820 vol.2, Oct 2002.

[233] Rosa M.S. Sigrist, Joy Liau, Ahmed El Kaffas, Maria Cristina Chammas, and Juergen K. Willmann. Ultrasound elastography: Review of techniques and clinical applications. In *Theranostics*, 2017.

[234] Eun Kyoung Hong, Young Hun Choi, Jung Eun Cheon, Woo Sun Kim, In-One Kim, and Sun Young Kang. Accurate measurements of liver stiffness using shear wave elastography in children and young adults and the role of the stability index. In *Ultrasonography*, 2017.

[235] Anthony E. Samir and Manish Dhyani et al. Shear-wave elastography for the estimation of liver fibrosis in chronic liver disease: determining accuracy and ideal site for measurement. *Radiology*, 274 3:888–96, 2015.

[236] Anesa Mulabecirovic, Anders Batman Mjelle, Odd Helge Gilja, Mette Vesterhus, and Roald Flesland Havre. Repeatability of shear wave elastography in liver fibrosis phantoms—evaluation of five different systems. In *PloS one*, 2018.

[237] C F Dietrich and Jeffrey Bamber et al. Efsumb guidelines and recommendations on the clinical use of liver ultrasound elastography, update 2017 (long version). *Ultraschall in der Medizin*, 38 4:e48, 2017.

[238] Mireen Friedrich-Rust, Thierry Poynard, and Laurent Castera. Critical comparison of elastography methods to assess chronic liver disease. *Nature Reviews Gastroenterology & Hepatology*, 13:402–411, 2016.

[239] Thomas Deffieux and Jean luc Gennisson et al. Investigating liver stiffness and viscosity for fibrosis, steatosis and activity staging using shear wave elastography. *Journal of hepatology*, 62 2:317–24, 2015.

[240] Najat Salameh and Benoît Larrat et al. Early detection of steatohepatitis in fatty rat liver by using mr elastography. *Radiology*, 253 1:90–7, 2009.

[241] Marie Muller, Jean-Luc Gennisson, Thomas Deffieux, Mickaël Tanter, and Mathias Fink. Quantitative viscoelasticity mapping of human liver using supersonic shear imaging: preliminary in vivo feasibility study. *Ultrasound in medicine & biology*, 35 2:219–29, 2009.

[242] Changtian Li, Changsheng Zhang, Jun lai Li, Huiping Huo, and Danfei Song. Diagnostic accuracy of real-time shear wave elastography for staging of liver fibrosis: A meta-analysis. *Medical science monitor : international medical journal of experimental and clinical research*, 22:1349–59, 2016.

[243] Bruno Lapuyade et al Christophe Cassinotto. Non-invasive assessment of liver fibrosis with impulse elastography: comparison of supersonic shear imaging with arfi and fibroscan®. *Journal of hepatology*, 61 3:550–7, 2014.

[244] Chen Shigao, Sanchez William, Callstrom Matthew R, Gorman Brian, Lewis Jason T, Sanderson Schuyler O, Greenleaf James F, Xie Hua, Shi Yan, Pashley Michael, et al. Assessment of liver viscoelasticity by using shear waves induced by ultrasound radiation force. *Radiology*, 266(3):964–970, 2013.

[245] Deffieux Thomas, Montaldo Gabriel, Tanter Mickaël, and Fink Mathias. Shear wave spectroscopy for in vivo quantification of human soft tissues visco-elasticity. *IEEE transactions on medical imaging*, 28(3):313–322, 2008.

[246] Barry Christopher T, Hah Zaegyoo, Partin Alexander, Mooney Robert A, Chuang Kuang-Hsiang, Augustine Alicia, Almudevar Anthony, Cao Wenqing, Rubens Deborah J, and Parker Kevin J. Mouse liver dispersion for the diagnosis of early-stage fatty liver disease: A 70-sample study. *Ultrasound in medicine & biology*, 40(4):704–713, 2014.

[247] Barbara L. McFarlin, Viksit Kumar, Timothy A. Bigelow, Douglas G. Simpson, Rosemary C. White-Traut, Jacques S. Abramowicz, and William D. O'Brien. Beyond cervical length: A pilot study of ultrasonic

attenuation for early detection of preterm birth risk. *Ultrasound in Medicine Biology*, 41(11):3023 – 3029, 2015.

[248] Laura Peralta, G Rus, Nicolas Bochud, and Francisca Sonia Molina. Assessing viscoelasticity of shear wave propagation in cervical tissue by multiscale computational simulation. *Journal of biomechanics*, 48 9:1549–56, 2015.

[249] Xuyuan Jiang, Patrick Asbach, K Streitberger, A Zdeblick Thomas, Bernd Hamm, Jürgen Braun, Ingolf Sack, and Jing Guo. In vivo high-resolution magnetic resonance elastography of the uterine corpus and cervix. *European Radiology*, 24:3025–3033, 2014.

[250] Shi Lei, Wang Yao, Yu Gan, Lily Zhao, McKee William Eugene, Joy Vink, Ronanld Wapner, Christine Hendon, and Kristin Myers. Anisotropic material characterization of human cervix tissue based on indentation. *Journal of biomechanical engineering*, 2019.

[251] Antonio Callejas, Antonio Gomez, Juan Melchor, Miguel Riveiro, Paloma Massó, Jorge Torres, Modesto López-López, and Guillermo Rus. Performance Study of a Torsional Wave Sensor and Cervical Tissue Characterization. *Sensors*, 17(9):2078, sep 2017.

[252] Paloma Massó, Antonio Callejas, Juan Melchor, Francisca S. Molina, and Guillermo Rus. In Vivo Measurement of Cervical Elasticity on Pregnant Women by Torsional Wave Technique: A Preliminary Study. *Sensors*, 19(15):3249, jul 2019.

[253] A. Ashofteh Yazdi, J. Melchor, J. Torres, I. Faris, A. Callejas, M. Gonzalez-Andrades, and G. Rus. Characterization of non-linear mechanical behavior of the cornea. *Sci. Rep.*, 10(1):11549, dec 2020.

[254] Mukhtar Bizrah, Ammar Yusuf, and Sajjad Ahmad. An update on chemical eye burns, sep 2019.

[255] Marion J. Fedoruk, Rod Bronstein, and Brent D. Kerger. Ammonia exposure and hazard assessment for selected household cleaning product uses. *J. Expo. Anal. Environ. Epidemiol.*, 15(6):534–544, nov 2005.

[256] Thomas R. Nelson, J. Brian Fowlkes, Jacques S. Abramowicz, and Charles C. Church. Ultrasound biosafety considerations for the practicing sonographer and sonologist, feb 2009.

[257] JunJie Wang, XiaoYu Liu, FangJun Bao, Bernardo T. Lopes, LiZhen Wang, Ashkan Eliasy, Ahmed Abass, and Ahmed Elsheikh. Review of

ex-vivo characterisation of corneal biomechanics. *Med. Nov. Technol. Devices*, 11:100074, sep 2021.

[258] Inas H. Faris, Juan Melchor, Antonio Callejas, Jorge Torres, and Guillermo Rus. Viscoelastic Biomarkers of Ex Vivo Liver Samples via Torsional Wave Elastography. *Diagnostics*, 10(2):111, feb 2020.

[259] Chien Chang Weng, Pei Yu Chen, Dean Chou, Cho Chiang Shih, and Chih Chung Huang. High Frequency Ultrasound Elastography for Estimating the Viscoelastic Properties of the Cornea Using Lamb Wave Model. *IEEE Trans. Biomed. Eng.*, 2020.

[260] Juan M. Bueno, Francisco J. Ávila, Elvira Lorenzo-Martín, Patricia Gallego-Muñoz, and M. Carmen Martínez-García. Assessment of the corneal collagen organization after chemical burn using second harmonic generation microscopy. *Biomed. Opt. Express*, 12(2):756, feb 2021.

[261] Thu Mai Nguyen, Jean François Aubry, David Touboul, Mathias Fink, Jean Luc Gennisson, Jeremy Bercoff, and Mickael Tanter. Monitoring of cornea elastic properties changes during UV-A/riboflavin-induced corneal collagen cross-linking using supersonic shear wave imaging: A pilot study. *Investig. Ophthalmol. Vis. Sci.*, 53(9):5948–5954, aug 2012.

[262] Wonsuk Kim, Alan Argento, Frank W. Rozsa, and Kaitlyn Mallett. Constitutive behavior of ocular tissues over a range of strain rates. *J. Biomech. Eng.*, 134(6), jun 2012.

[263] Daniel V. Litwiller, Sung J. Lee, Arunark Kolipaka, Yogesh K. Mariappan, Kevin J. Glaser, Jose S. Pulido, and Richard L. Ehman. MR elastography of the ex vivo bovine globe. *J. Magn. Reson. Imaging*, 32(1):44–51, jun 2010.

[264] Thu Mai Nguyen, Jean Francois Aubry, Mathias Fink, Jeremy Bercoff, and Mickael Tanter. In vivo evidence of porcine cornea anisotropy using supersonic shear wave imaging. *Investig. Ophthalmol. Vis. Sci.*, 55(11):7545–7552, nov 2014.

[265] Antoine Ramier, Amira M. Eltony, Yi Tong Chen, Fatima Clouser, Judith S. Birkenfeld, Amy Watts, and Seok Hyun Yun. In vivo measurement of shear modulus of the human cornea using optical coherence elastography. *Sci. Rep.*, 10(1):1–10, dec 2020.

[266] M. Tanter, D. Touboul, Jean Luc Gennisson, Jeremy Bercoff, and Mathias Fink. High-resolution quantitative imaging of cornea elasticity using supersonic shear imaging. *IEEE Trans. Med. Imaging*, 28(12):1881–1893, dec 2009.

[267] Xuejun Qian, Teng Ma, Cho Chiang Shih, Martin Heur, Jun Zhang, Koping Kirk Shung, Rohit Varma, Mark S. Humayun, and Qifa Zhou. Ultrasonic Microelastography to Assess Biomechanical Properties of the Cornea. *IEEE Trans. Biomed. Eng.*, 66(3):647–655, mar 2019.

[268] Boran Zhou, Arthur J. Sit, and Xiaoming Zhang. Noninvasive measurement of wave speed of porcine cornea in ex vivo porcine eyes for various intraocular pressures. *Ultrasonics*, 81:86–92, nov 2017.

[269] Hamed Hatami-Marbini and Ebitimi Etebu. Hydration dependent biomechanical properties of the corneal stroma. *Exp. Eye Res.*, 116:47–54, nov 2013.

[270] Manmohan Singh, Zhaolong Han, Jiasong Li, Srilatha Vantipalli, Salavat R. Aglyamov, Michael D. Twa, and Kirill V. Larin. Quantifying the effects of hydration on corneal stiffness with noncontact optical coherence elastography. *J. Cataract Refract. Surg.*, 44(8):1023–1031, aug 2018.

[271] Nery Garcia-Porta, Paulo Fernandes, Antonio Queiros, Jose Salgado-Borges, Manuel Parafita-Mato, and Jose Manuel González-Méijome. Corneal Biomechanical Properties in Different Ocular Conditions and New Measurement Techniques. *ISRN Ophthalmol.*, 2014:1–19, mar 2014.

[272] Zhaolong Han, Jiasong Li, Manmohan Singh, Chen Wu, Chih hao Liu, Raksha Raghunathan, Salavat R. Aglyamov, Srilatha Vantipalli, Michael D. Twa, and Kirill V. Larin. Optical coherence elastography assessment of corneal viscoelasticity with a modified Rayleigh-Lamb wave model. *J. Mech. Behav. Biomed. Mater.*, 66:87–94, feb 2017.

[273] Zi Jin, Yuheng Zhou, Meixiao Shen, Yuanyuan Wang, Fan Lu, and Dexi Zhu. Assessment of corneal viscoelasticity using elastic wave optical coherence elastography. *J. Biophotonics*, 13(1):e201960074, jan 2020.

[274] Antoine Ramier, Behrouz Tavakol, and Seok-Hyun Yun. Measuring mechanical wave speed, dispersion, and viscoelastic modulus of the cornea using optical coherence elastography. *Opt. Express*, 27(12):16635, jun 2019.

[275] Guillermo Rus, Inas H. Faris, Jorge Torres, Antonio Callejas, and Juan Melchor. Why Are Viscosity and Nonlinearity Bound to Make an Impact in Clinical Elastographic Diagnosis? *Sensors*, 20(8):2379, apr 2020.

[276] Riegler Johannes, Labyed Yassin, Rosenzweig Stephen, Javinal Vincent, Castiglioni Alessandra, Dominguez Claudia X, Long Jason E, Li Qingling, Sandoval Wendy, Junttila Melissa R, et al. Tumor elastography and its association with collagen and the tumor microenvironment. *Clinical Cancer Research*, 24(18):4455–4467, 2018.

[277] Guillermo Rus, Inas H Faris, Jorge Torres, Antonio Callejas, and Juan Melchor. Why are viscosity and nonlinearity bound to make an impact in clinical elastographic diagnosis? *Sensors*, 20(8):2379, 2020.

[278] Rosa MS Sigrist, Joy Liau, Ahmed El Kaffas, Maria Cristina Chammas, and Juergen K Willmann. Ultrasound elastography: review of techniques and clinical applications. *Theranostics*, 7(5):1303, 2017.

[279] Tsuyoshi Shiina. Wfumb guidelines and recommendations for clinical use of ultrasound elastography: Part 1: basic principles and terminology. *Ultrasound in Medicine and Biology*, 43:S191–S192, 2017.

[280] R Sinkus, M Tanter, Catheline S, J Lorenzen, C Kuhl, E Sondermann, and M Fink. Imaging anisotropic and viscous properties of breast tissue by magnetic resonance-elastography. *Magnetic Resonance in Medicine: An Official Journal of the International Society for Magnetic Resonance in Medicine*, 53(2):372–387, 2005.

[281] Armen P Sarvazyan, Matthew W Urban, and Greenleaf James F. Acoustic waves in medical imaging and diagnostics. *Ultrasound in medicine & biology*, 39(7):1133–1146, 2013.

[282] Daniel Royer, Jean-Luc Gennisson, Thomas Deffieux, and Mickaël Tanter. On the elasticity of transverse isotropic soft tissues (l). *The Journal of the Acoustical Society of America*, 129(5):2757–2760, 2011.

[283] John T Conrad, Richard D Tokarz, and John F Williford. Anatomic site and stretch modulus in the human cervix. *Dilatation of the uterine cervix (connective tissue biology and clinical management)*, 255:64, 1980.

[284] Jean-Luc Gennisson, Stefan Catheline, Sana Chaffaı, and Mathias Fink. Transient elastography in anisotropic medium: application to

the measurement of slow and fast shear wave speeds in muscles. *The Journal of the Acoustical Society of America*, 114(1):536–541, 2003.

[285] Kathryn R Nightingale, Mark L Palmeri, Roger W Nightingale, and Gregg E Trahey. On the feasibility of remote palpation using acoustic radiation force. *The Journal of the Acoustical Society of America*, 110(1):625–634, 2001.

[286] Michael Wang, Brett Byram, Mark Palmeri, Ned Rouze, and Kathryn Nightingale. Imaging transverse isotropic properties of muscle by monitoring acoustic radiation force induced shear waves using a 2-d matrix ultrasound array. *IEEE transactions on medical imaging*, 32(9):1671–1684, 2013.

[287] Jean-Luc Gennisson, Thomas Deffieux, Emilie Macé, Gabriel Montaldo, Mathias Fink, and Mickaël Tanter. Viscoelastic and anisotropic mechanical properties of in vivo muscle tissue assessed by supersonic shear imaging. *Ultrasound in medicine & biology*, 36(5):789–801, 2010.

[288] Sara Aristizabal, Carolina Amador, Bo Qiang, Randall R Kinnick, Ivan Z Nenadic, James F Greenleaf, and Matthew W Urban. Shear wave vibrometry evaluation in transverse isotropic tissue mimicking phantoms and skeletal muscle. *Physics in Medicine & Biology*, 59(24):7735, 2014.

[289] Simon Chatelin, Miguel Bernal, Thomas Deffieux, Clément Papadacci, Patrice Flaud, Amir Nahas, Claude Boccara, Jean-Luc Gennisson, Mickael Tanter, and Mathieu Pernot. Anisotropic polyvinyl alcohol hydrogel phantom for shear wave elastography in fibrous biological soft tissue: a multimodality characterization. *Physics in Medicine & Biology*, 59(22):6923, 2014.

[290] Wang Yao, Yu Gan, Kristin M Myers, Joy Y Vink, Ronald J Wapner, and Christine P Hendon. Collagen fiber orientation and dispersion in the upper cervix of non-pregnant and pregnant women. *PloS one*, 11(11):e0166709, 2016.

[291] Joseph Chue-Sang, Yuqiang Bai, Susan Stoff, Mariacarla Gonzalez, Nola A Holness, Jefferson Gomes, Ranu Jung, Amir H Gandjbakhche, Viktor V Chernomordik, and Jessica C Ramella-Roman. Use of mueller matrix polarimetry and optical coherence tomography in the characterization of cervical collagen anisotropy. *Journal of biomedical optics*, 22(8):086010, 2017.

[292] Feltovich H and TJ Hall. Quantitative imaging of the cervix: setting the bar. *Ultrasound in Obstetrics & Gynecology*, 41(2):121–128, 2013.

[293] Yu Gan, Wang Yao, Kristin M Myers, Joy Y Vink, Ronald J Wapner, and Christine P Hendon. Analyzing three-dimensional ultrastructure of human cervical tissue using optical coherence tomography. *Biomedical optics express*, 6(4):1090–1108, 2015.

[294] Joy Vink and Mirella Mourad. The pathophysiology of human premature cervical remodeling resulting in spontaneous preterm birth: Where are we now? In *Seminars in perinatology*, volume 41, pages 427–437. Elsevier, 2017.

[295] Mathieu Couade, Mathieu Pernot, Emmanuel Messas, Alain Bel, Maguette Ba, Albert Hagège, Mathias Fink, and Mickael Tanter. In vivo quantitative mapping of myocardial stiffening and transmural anisotropy during the cardiac cycle. *IEEE transactions on medical imaging*, 30(2):295–305, 2010.

[296] Wei-Ning Lee, Benoît Larrat, Mathieu Pernot, and Mickaël Tanter. Ultrasound elastic tensor imaging: comparison with mr diffusion tensor imaging in the myocardium. *Physics in Medicine & Biology*, 57(16):5075, 2012.

[297] Edoardo Mazza, Alessandro Nava, Margit Bauer, Raimund Winter, Michael Bajka, and Gerhard A Holzapfel. Mechanical properties of the human uterine cervix: an in vivo study. *Medical image analysis*, 10(2):125–136, 2006.

[298] Atala Anthony, Kasper F Kurtis, and Mikos Antonios G. Engineering complex tissues. *Science translational medicine*, 4(160):160rv12–160rv12, 2012.

[299] James Casey and Marcel J Crochet. *Theoretical, Experimental, and Numerical Contributions to the Mechanics of Fluids and Solids: A collection of papers in honor of Paul M. Naghdi*. Birkhäuser, 2012.

[300] Robert S Langer and Vacanti Joseph P. Tissue engineering: the challenges ahead. *Scientific American*, 280(4):86–89, 1999.

[301] Simon Chatelin, Caroline Deck, and Rémy Willinger. An anisotropic viscous hyperelastic constitutive law for brain material finite-element modeling. *Journal of biorheology*, 27(1-2):26–37, 2013.

[302] Rachel B Groves, Sion A Coulman, James C Birchall, and Sam L Evans. An anisotropic, hyperelastic model for skin: experimental measurements, finite element modelling and identification of parameters for human and murine skin. *Journal of the mechanical behavior of biomedical materials*, 18:167–180, 2013.

[303] Grand Roman Joldes, Adam Wittek, and Karol Miller. Suite of finite element algorithms for accurate computation of soft tissue deformation for surgical simulation. *Medical image analysis*, 13(6):912–919, 2009.

[304] Taotao Wu, Alshareef Ahmed, Giudice J Sebastian, and Matthew B Panzer. Explicit modeling of white matter axonal fiber tracts in a finite element brain model. *Annals of biomedical engineering*, pages 1–15, 2019.

[305] Bajka M and Haller U. Virtual reality based surgery simulation for endoscopic gynaecology. *Medicine Meets Virtual Reality: The Convergence of Physical & Informational Technologies: Options for a New Era in Healthcare*, 62:351, 1999.

[306] Yoshida Emilia A, Castro Márcia LA, and Martins Valéria F. Virtual reality and fetal medicine—a systematic review. In *2017 XLIII Latin American Computer Conference (CLEI)*, pages 1–10. IEEE, 2017.

[307] Misra Sarthak, Ramesh KT, and Okamura Allison M. Modeling of tool-tissue interactions for computer-based surgical simulation: a literature review. *Presence: Teleoperators and Virtual Environments*, 17(5):463–491, 2008.

[308] Lukasz Fracczak, Szaniewski Mateusz, and Podsedkowski Leszek. Share control of surgery robot master manipulator guiding tool along the standard path. *The International Journal of Medical Robotics and Computer Assisted Surgery*, 15(3):e1984, 2019.

[309] NA STEPHANE COTIN HERVE DELINGETTE. Efficient linear elastic models of soft tissues for real-time surgery simulation. Technical report, Tech. rep., Institut National de Recherche en Informoatique et en Automatique, 1998.

[310] Zhang Chenxi, Wang Manning, and Song Zhijian. A brain-deformation framework based on a linear elastic model and evaluation using clinical data. *IEEE Transactions on Biomedical Engineering*, 58(1):191–199, 2010.

[311] LD Landau. Lifshitz (1970) theory of elasticity.

[312] Rashid Badar, Destrade Michel, and Michael D Gilchrist. Mechanical characterization of brain tissue in tension at dynamic strain rates. *Journal of the mechanical behavior of biomedical materials*, 33:43–54, 2014.

[313] Zemánek Miroslav, Burša Jiří, and Děták Michal. Biaxial tension tests with soft tissues of arterial wall. *Engineering Mechanics*, 16(1):3–11, 2009.

[314] J-L Gennisson, Mathieu Rénier, Catheline Stefan, Barrière Christophe, Bercoff Jeremy, Mickael Tanter, and Mathias Fink. Acoustoelasticity in soft solids: Assessment of the nonlinear shear modulus with the acoustic radiation force. *The Journal of the Acoustical Society of America*, 122(6):3211–3219, 2007.

[315] Miguel Bernal, Foucauld Chamming?s, Couade Mathieu, Bercoff Jeremy, Mickaël Tanter, and Jean-Luc Gennisson. In vivoquantification of the nonlinear shear modulus in breast lesions: Feasibility study. *IEEE transactions on ultrasonics, ferroelectrics, and frequency control*, 63(1):101–109, 2015.

UNIVERSIDAD
DE GRANADA